Title
Bed topography of Greenland glaciers from high-resolution gravity data

Author
AN, LU

Publication Date
2017

Peer reviewed|Thesis/dissertation

UNIVERSITY OF CALIFORNIA,
IRVINE

Bed Topography of Greenland Glaciers from High-resolution Gravity Data

DISSERTATION

submitted in partial satisfaction of the requirements
for the degree of

DOCTOR OF PHILOSOPHY

in Earth System Science

by

Lu An

Dissertation Committee:
Professor Eric Rignot, Advisor, Chair
Professor François Primeau
Professor Isabella Velicogna

2017

DEDICATION

To my beloved family and friends

A man who keeps company with glaciers comes to feel tolerably insignificant by and by. The Alps and the glaciers together are able to take every bit of conceit out of a man and reduce his self-importance to zero if he will only remain within the influence of their sublime presence long enough to give it a fair and reasonable chance to do its work.

— Mark Twain, A Tramp Abroad

TABLE OF CONTENTS

LIST OF FIGURES

LIST OF TABLES

ACKNOWLEDGMENTS

I would like to thank my PhD advisor Prof. Eric Rignot for taking me as a PhD student and bringing me to the ice world six years ago. His enthusiasm for science and great ideas on glaciers inspired me through my whole PhD life, which I will definitely carry with me during my future career.

This dissertation would not have been possible without all the help I received during these years. I thank Prof. Isabella Velicogna for her help on all the knowledge on gravity and the encouragement on my research. I also appreciate Professor François Primeau for his suggestion on the model parts related to ice interaction with ocean. Professor Todd K. Dupont is so kind and provided useful suggestion on ice modeling for me. I am so lucky to join the cryosphere group in UCI. All my colleagues are always friendly and willing to provide help. Professor Mathieu Morlighem is expressed me by his excellent mass conservation method in the development of the Ice Sheet System Model (ISSM). I really want to thank him for his help providing all the data and also patience on teaching me technical details. Jeremie Mouginot and Bernd Scheuchl, both are experts on Remote Sensing, gave me a lot of support when I stuck in my research. All the other members in the cryosphere group, senior colleagues Yu Xun and Xin Li, current members Cilan Cai, Hongju Yu, Romain Millan, Mike Wood and Emily Kane, they always gave me some ideas both on research and daily life. Except group members, people from the whole department are all friendly, especially peers same year as me, Aimee Gibbons, Elliot Shermane, Chia-wei Hsu, Jordan Schnell, Hrishi Chandanpurkar, Jamiat Nanteza and Kurt Solaner. I still remembered the day and night we fighting on projects and exams during our first year. And continuous support and encouragement I received from them during my PhD career.

Lots of help from outside the department kept the research going well. Kirsty Tinto from Lamont-Doherty Earth Observatory of Columbia University, who is an expert on gravity and magnetic inversion on glaciers, solved a lots of questions at the early stage of my research. I always learned a lot after talked with her during conferences or through emails. Dr. Atsuhiro Muto, now is an assistant professor in Department of Earth and Environmental Science of Temple University, gave me lots of support on the gravity model he developed, which I discussed in detail in Chapter 4. David Holland and Denise Holland acknowledge support from the NSF office of Polar Program ARC-1304137, and the NYU Abu Dhabi Center for Global Sea Level Change grant G1204. Denis Voytenko is thanked for assisting with the preparation for the XCTD bathymetric data file.

I am really want to thank my family, especially my mom and dad, without their support behind my back, I don't think I could arrive at this stage. People come, people gone. My parents are always there. I am grateful to my friends both in US and China, who love me regardless of success or failure, always with trust and encouragement. Thanks to all the people accompany with me , help me on my bumpy way to the degree.

This work was performed at the Department of Earth System Science, University of California, Irvine under grant 3280 from the Gordon and Betty Moore Foundation since 2012, funds from UC Irvine, and NASA grant NNX12AB86G; at Caltech's Jet Propulsion Laboratory, Pasadena under a contract with NASA. We thank the NASA Operation Ice Bridge project for their provision of data to the community.

Parts of Chapter 2 and Chapter 4 are reprinted with permission from the American Geophysical Union. The original texts appear in Journal of Geophysical Research Letters. I thank all the coauthors for their work and suggestion that made the publication of these two articles possible.

CURRICULUM VITAE

Lu An

EDUCATION

Doctor of Philosophy in Earth System Science **2017**
University California *Irvine, California*

Master of Science in Earth System Science **2013**
University of California, Irvine *Irvine, California*

Bachelor of Science in Atmospheric Sciences **2011**
Nanjing University *Nanjing, China*

RESEARCH EXPERIENCE

Graduate Research Assistant **2011–2017**
University of California, Irvine *Irvine, California*

International Summer School in Glaciology **June 2016**
University of Alaska, Fairbanks *McCarthy, Alaska*

Courses focus on modeling, quantitative glaciology and remote sensing.
Student project: Using Remote Sensing Techniques to map glacier changes. (Prof. Leigh Stearns)

TEACHING EXPERIENCE

INTRO TO ESS Teaching Assistant **Fall 2012 & 2016**
Lead instructor: Dr. Julie Ferguson UC, Irvine

ON THIN ICE Teaching Assistant **Winter 2013, Spring 2016 & Spring 2017**
Lead instructor: Dr. Julie Ferguson UC, Irvine

MODELING THE EARTH Teaching Assistant **Spring 2013 & 2014**
Lead instructor: Prof. Todd Dupont UC, Irvine

CATASTROPHES Teaching Assistant **Fall 2014**
Lead instructor: Prof. Claudia Czimczik UC, Irvine

Developed science communication and teaching skills by hosting the discussion sessions, office hours and a few lectures.
Collaborated with professors and other teaching assistants in curriculum design and homework/quiz/exam assignments and grading.

JOURNAL PUBLICATIONS

An, L., E. Rignot, J. Mouginot, R. Milan (2017), A century of stability of Avannarleq and Kujalleq glaciers, West Greenland, explained using high-resolution airborne gravity and other data *Geophys. Res. Lett.*, (submitted).

M. Morlighem, C.N. Williams, E. Rignot, **L. An**, J.E. Arndt, J.L. Bamber, G. Catania, N. Chauché, J.A. Dowdeswell, B. Dorschel, I. Fenty, K. Hogan, I. Howat, A. Hubbard, M. Jakobsson, T.M. Jordan, K.K. Kjeldsen, R. Millan, L. Mayer, J. Mouginot, B.P.Y. Noël, C. Ó Cofaigh, S. Palmer, S. Rysgaard, H. Seroussi, M.J. Siegert, P. Slabon, F. Straneo, M.R. van den Broeke, W. Weinrebe, M. Wood and K.B. Zinglersen (2017), BedMachine v3: Complete bed topography and ocean bathymetry mapping of Greenland from multi-beam echo sounding combined with mass conservation, *Geophys. Res. Lett.*, doi:10.1002/2017GL074954.

An, L., E. Rignot, S. Elieff, M. Morlighem, R. Milan, J. Mouginot, D.M. Holland, D. Holland and J. Paden (2017), Bed elevation of Jakobshavn Isbr, West Greenland, from high-resolution airborne gravity and other data, *Geophys. Res. Lett.*, **44**, doi:10.1002/2017GL073245.

Rignot, E., Y. Xu, D. Menemenlis, J. Mouginot, B. Scheuchl, X. Li, M. Morlighem, H. Seroussi, M.van den Broeke, I.Fenty, C. Cai, **L. An** and B. de Fleurian (2016), Modeling of ocean-induced ice melt rates of five west Greenland glaciers over the past two decades, *Geophys. Res. Lett.*, **43**, 6374-6382, doi:10.1002/2016GL068784.

Zhou, D., A. Ding, H. Mao, C. Fu, T. Wang, L. Chan, K. Ding, Y. Zhang, J. Liu, **L. An** and N. Hao (2013), Impacts of the East Asian monsoon on lower tropospheric ozone over costal South China, *Environ. Res. Lett.*, **8**, doi:10.1088/1748-9326/8/4/044011.

CONFERENCE PUBLICATIONS

An, L., E. Rignot, S. Elieff, M. Morlighem, J. Mouginot, D. M. Holland, D. Holland and J. Paden. Bed elevation of West Greenland, from high-resolution airborne gravity and other observations. Abstract C12B-02. **Oral** presentation at AGU Fall Meeting 2016, San Francisco, 12-16 December, 2016.

An, L., E. Rignot, M. Morlighem, J. Paden and D. M. Holland. Bed topography of Jakobsahvn Isbræ, Greenland from high-resolution gravity data. Abstract 74a2089. Poster presentation at International Symposium on Interactions of Ice Sheets and Glaciers with the Ocean, Scripps Institution of Oceanography, La Jolla, CA, 10-15 July 2016.

An, L., E. Rignot, M. Morlighem, J. Paden and D. M. Holland. Bed topography of Jakobsahvn Isbr, Greenland from high-resolution gravity data. Abstract C53C-0792. Poster presentation at AGU Fall Meeting 2015, San Francisco, 14-18 December 2015.

An, L., E. Rignot, A. Muto and M. Morlighem. Bed topography of Store Glacier and Fjord, Greenland from high-resolution gravity data and multi-beam echo sounding. Abstract C21B-

0317. Poster presentation at AGU Fall Meeting 2014, San Francisco, 15-19 December 2014.

An, L., E. Rignot, and M. Morlighem. 2D Bed topography from high-resolution airborne gravity data of Store Glacier and Jakobshavn Isbræ. Abstract C51A-0499. Poster presentation at AGU Fall Meeting 2013, San Francisco, 9-13 December 2013.

An, L., E Rignot, A. Rivera, R. Zamora, M. Buneta, S. Elieff and M. Morlighem. Using high-resolution airborne gravity data combined with other data to map glacier bed topography in Patagonia and Greenland. Abstract 1479499. Poster presentation at AGU Fall Meeting 2012, San Francisco. 3-7 December 2012.

VOLUNTEER EXPERIENCE

Graduate InterConnect Peer Mentor 2016–17

To support and guide new international students through a successful transition to their academic programs and to the campus community.

ABSTRACT OF THE DISSERTATION

Bed Topography of Greenland Glaciers from High-resolution Gravity Data

By

Lu An

Doctor of Philosophy in Earth System Science

University of California, Irvine, 2017

Professor Eric Rignot, Advisor, Chair

The mass balance of glaciers is influenced by their bed elevation below sea level, surface melt, and ocean-induced ice melt at calving fronts. It is essential to know the glacier thickness, bed elevation and fjord bathymetry to interpret the glacier evolution in the ongoing warm climate. Traditional methods for mapping ice thickness from radar sounding fail in the terminal valleys occupied by glaciers and near glacier calving fronts because of challenging conditions: side returns, rough surface, warm ice, water inclusions. We had to explore new ways to infer ice thickness. The advent of modern airborne gravimeters capable of sub milligal precision made it possible to explore the usage of gravity. Such instrument had been used widely for oil and mineral surveys and we applied it to glacier ice.

In this dissertation, we use airborne gravity data collected in August 2012 with a 0.5 mGal precision at a spatial resolution 750 m, combined with measurements of the fjord bathymetry and mass conservation reconstruction solution to obtain novel mapping of bed topography for several glaciers in Greenland. We use both 2D and 3D modeling to interpret the gravity data in these areas. The models are heavily constrained by geological information as much as we got, such as ocean bathymetry data, rock density information from Geological Survey of Denmark and Greenland with the selection of more optimized initial solutions. We use the gravity misfit to quantify the uncertainty of the inversion. The inversion significantly reduces

the gravity misfit from the initial bed, as expected. The gravity misfit ranges from -3 to $+3$ mGal, the nominal precision of our bed mapping is about 60 m. Our study demonstrated the practical use of high-resolution airborne gravity to fill critical gaps in bed elevation in Greenland, especially in deep fjords that cannot be surveyed with deep radar sounders. The results provide more definite view of the bed topography of these major glaciers system than available previously, meanwhile, at a spatial resolution of 750 m along the trough and with an average precision of about 60 m.

This study provides simple guidelines for utilizing gravity data to obtain glaciers bed topography and then to understand glaciers' evolution in ongoing warm climate for both ocean and atmosphere.

Chapter 1

Introduction

Glacier ice covers about 10% of the Earth's land surface at present time, including glaciers, ice caps, and the ice sheets of Greenland and Antarctica. The Greenland and Antarctica ice sheets together hold 33 million km^3 of ice, representing enough water to raise global sea level by 70 m (*Rignot and Thomas*, 2002). A tiny change in volume of these ice sheets due to climate warming could have a big effect on global sea level. In 2006, the Greenland and Antarctic ice sheets experienced a combined mass loss of 475 $\pm$ 158 Gt/yr and lost mass at a combined rate equivalent to 1.3 $\pm$ 0.4 mm/yr of sea level rise (*Rignot et al.*, 2011a). This mass loss appear to from acceleration of the outlet glaciers and ice streams draining the basins, producing increased flux across the grounding line into the ocean.

For Greenland itself, the contribution to sea level rise (SLR) increased from 0.23 $\pm$ 0.08 mm/yr in 1996 to 0.57 $\pm$ 0.01 mm/yr in 2005 (*Rignot and Kanagaratnam*, 2006). Increased surface melting accounts for approximately one third of the mass loss from Greenland in the last Decade (*Rignot and Kanagaratnam*, 2006). The change of surface elevation in West Greenland can reach up to 1.5 m/yr (*Pritchard et al.*, 2009) (Figure 1.1). The rest was lost by increased calving related to glacier dynamics, therefore, ice dynamics dominates the contribution to SLR from Greenland ice sheet (GrIS). And also these processes will continue to play an important role in the future. Both basal melting by sub-glacial warm water or the dynamical instability near glacier grounding line could be the trigger for glacier calving. Because the grounding line has been retreating, thicker ice columns will be exposed to warm ocean waters, leading to further retreat of the grounding line. Current models used to project the contribution to sea level from the GrIS due to climate change do not consider the physical processes and hence do not account for the effect of glacier dynamics. So most of the models only provide lower limits to the potential contribution from Greenland to sea level rise. Greenland ice loss is accelerating by climate warming now, if more glaciers accelerate father north, especially along the west coast, the mass loss from Greenland will continue to increase above predictions. Thus understanding the glacial physics and putting them into models are really desirable.

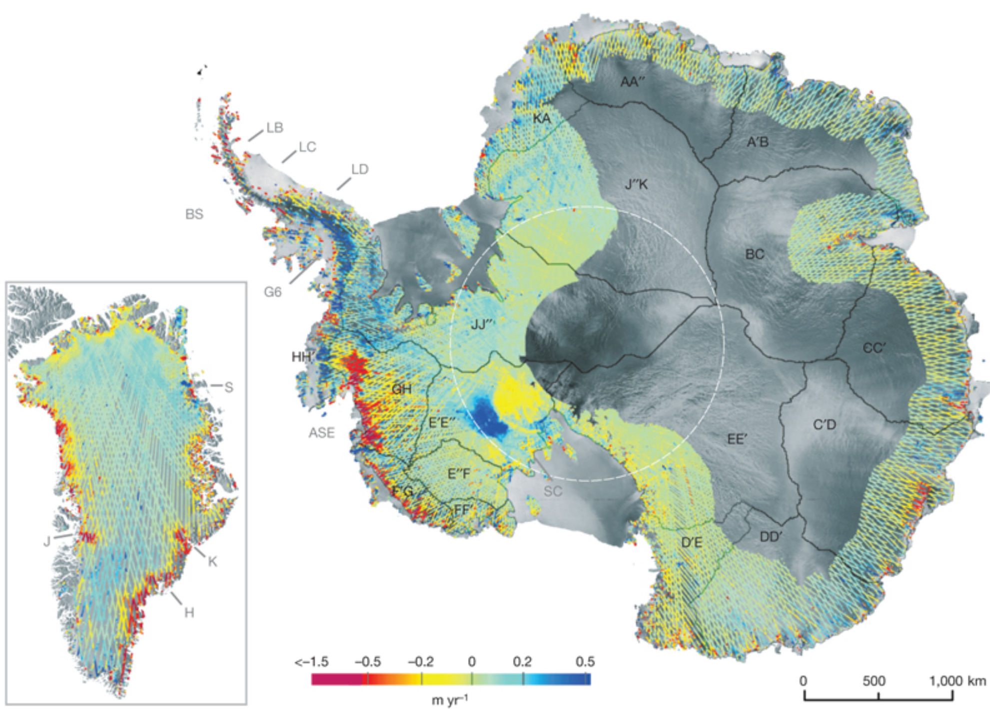

Figure 1.1: Rate of change of surface elevation for Antarctica and Greenland (*Pritchard et al.*, 2009).

Glaciers in other areas are also important elements of many landscapes: they release water, scour bedrock, cool the weather in summer, and advance down valleys or retreat into high basins. Patagonia glaciers are the largest ice fields in the Southern Hemisphere outside Antarctica. The Northern Patagonia Ice Field (NPI), located completely in Chile, and the Southern Patagonia Ice Field (SPI), shared between Chile and Argentina. Their areas are about 4200 and 13,000 km^2 respectively. The ice lost from the largest 63 glaciers of NPI and SPI during the period 1968/1975-2000, at a rate equivalent to a sea level rise of 0.042 $\pm$ 0.002 mm/yr. And in the year 1995-2000, the mean ice-thinning rate to an equivalent sea level rise is about 0.105 $\pm$ 0.011 mm/yr (*Rignot et al.*, 2003). However, more studies are needed because of few available mass balance data exist, giving a considerable uncertainty in the estimation of its contribution to sea level rise.

1.1 Mass balance of Greenland Ice Sheet

Ice balance between net accumulation and loss of these two ice sheets are quite different. The Antarctic ice sheet is about ten times as large as the Greenland ice sheet. Antarctica dominates its own climate and the surrounding Southern Ocean, which is cold even during summer. Hence, there is little surface melting, the ice attrition is mainly from basal melting and iceberg calving from ice shelves. However, Greenland's ice loss is primarily by surface runoff and iceberg calving because of the nearby land mass and the warm North Atlantic Ocean (*Rignot and Thomas*, 2002). There are three ways of measuring the mass balance of an ice sheet. First, calculate the mass budget of an ice sheet. Net accumulation is inferred from ice-core measurements, and net loss by melting, which the melt rates are estimated from positive degree-day models (*Braithwaite*, 1995). The second method is measuring the elevation change with radar altimeters and then translate to volume change over time. The last way is weighing the ice sheets by the NASA's Gravity Recovery and Climate Experiment (GRACE) satellite measuring gravity change of the Earth. It shows how mass is distributed around earth and how it varies over time (Figure 1.2).

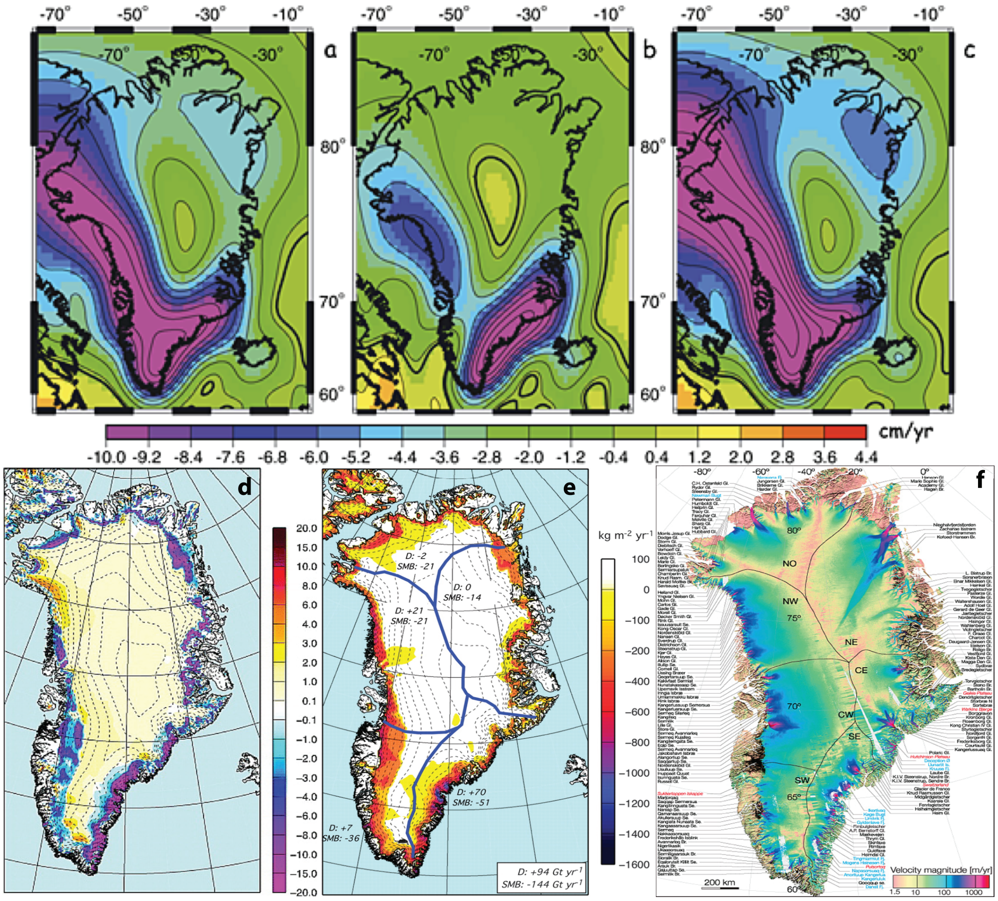

Figure 1.2: Rates of ice mass change in cm/yr of water from GRACE (a) January 2003 to November 2012, (b) January 2003 to December 2006, (c) December 2006 to November 2012 (*Velicogna and Wahr*, 2013), (d) RACMO2/GR modeled surface mass balance trend (1958-2007) in kg/m^2 (*Ettema et al.*, 2009), (e) Distribution of 2003-2008 mass changes due to SMB and D in Gt/yr (*van den Broeke et al.*, 2009), and (f) Ice velocity map of Greenland in m/yr (*Rignot and Mouginot*, 2012).

Based on the gravity mission from GRACE, in Greenland, the mass loss increased from 137 Gt/yr in 2002-2003 to 286 Gt/yr in 2007-2009 with an acceleration of 30 $\pm$ 11 Gt/yr^2 in 2002-2009 (*Velicogna*, 2009). In Figure 1.2 abc, mass loss appeared in southeast Greenland in 2003-2006, however, during the 2006-2012, the mass loss spread to northern side of Greenland, especially along the northwest coast and the northeast (*Velicogna and Wahr*, 2013; *Khan et al.*, 2010). Also, the mass budget method qualified from surface mass balance (SMB) subtracting ice discharge (D) (Figure 1.2 e) is validated by GRACE. The mass loss in 2000-2008 is $\sim$ 167 Gt/yr, which is equivalent to 0.46 mm/yr global sea level rise (*van den Broeke et al.*, 2009). *Ettema et al.* (2009) employed high-resolution ($\sim$ 11 km) regional climate modeling to calculate the annual average SMB of 469 $\pm$ 41 Gt/yr for 1958-2007 by subtracting total runoff (248 Gt/yr) and evaporation/sublimation (26 Gt/yr) from total snowfall (697 Gt/yr) and rainfall (46 Gt/yr). The GrIS SMB has increased rapidly since 1990 (*Rignot et al.*, 2008) (Figure 1.2 d). Interferometric synthetic aperture radar (InSAR) observations have revealed widespread glacier acceleration along the coast of GrIS (*Rignot and Kanagaratnam*, 2006) (Figure 1.2 f). Greenland mass loss is doubled with the contribution to SLR from 0.23 $\pm$ 0.08 mm/yr in 1996 to 0.57 $\pm$ 0.1 mm/yr in 2005 (*Rignot and Kanagaratnam*, 2006). Greenland is dominated by tidewater glaciers, which drain 88% of the ice area (*Rignot and Mouginot*, 2012). In 2006, the total mass loss from Greenland is 250 $\pm$ 40 Gt/yr, which equivalent to 0.6 $\pm$ 0.4 mm/yr SLR (*Rignot et al.*, 2011a). Between January and September in 2012, Greenland reveals a large mass loss (700 $\pm$ 100 Gt) by GRACE (*Velicogna and Wahr*, 2013). The GrIS not only experienced more total melt, but the melt was more persistent, and the summer temperature became the warmest in the Satellite-derived moderate-resolution imaging spectroradiometer (MODIS) record (-6.38 $\pm$ 3.98°C). (*Hall et al.*, 2013).

1.2 Oceanic forcing of Greenland's glaciers

Rignot and Kanagaratnam (2006) indicated that one third of the mass loss from Greenland in the last decade was due to increased surface melting. The rest was lost by increased calving related to glacier dynamics. What is the trigger for glacier calving? It is uncertain whether this is due to basal melting caused by sub-glacial warm water or the dynamical instability near glacier grounding line. Large areas of the ice sheets have a bed deepening in the inland direction because of thicker ice in the middle. In these areas, when the grounding line retreats, thicker ice columns will be exposed to warm ocean waters, leading to further retreat of the grounding line. Thus it is desirable to improve our understanding of the physics of glaciers so that we can improve the models used to predict sea level rise. Knowing the glacier basal topography and behaviors of ocean currents can determine (1) how the seawater flows in front of the ice (2) how much water can reach the glaciers grounding line, and (3) whether the heat coming from ocean will reach the ice.

The majority of Greenland's glaciers are marine-terminating glaciers, and the mass balance of these tidewater glaciers are controlled by calving, like Helheim and Kangerdlugssuaq (*Stearns and Hamilton*, 2007), Jakobshavn Isbræ (*Thomas et al.*, 2003; *Joughin et al.*, 2008) and Store Glacier (*Xu et al.*, 2013), with a relatively short ice tongues or grounded termini (Figure 1.3 a). They are typically grounded several hundreds of meters below sea level at the head of long (10-100 km), narrow (< 10 km) fjords (*Straneo and Heimbach*, 2013). Then the ice flow at the glacier front, accumulation of ice mélange and ocean water circulation really depend on how the fjords setting are (*MacAyeal et al.*, 2012, e.g.). By contrast the mass loss of the glaciers found in the north of Greenland, such as Petermann Glaciers (*Rignot and Steffen*, 2008) and 79 North Glacier (*Mouginot et al.*, 2015) with long floating ice tongues (Figure 1.3 b), is due mainly to surface and submarine melting.

The ocean currents near Greenland are influenced by the cyclonic sub-polar gyre circulation of the North Atlantic and the Arctic region (Figure 1.4). The warm and salty water from the subtropical Atlantic is carried by the Gulf Stream northward, and then moves toward the east with the North Atlantic Current (NAC) (*Holland et al.*, 2008; *Straneo et al.*, 2012). In West Greenland, the water masses are a mixture of cold low-salinity Polar Water (PW) and warmer and saltier Irminger Water (IW). The surface circulation is dominant by the northward West Greenland Current (WGC) (*Ribergaard*, 2013). As the water travels north with heat loses at high latitude, the water temperature is 10 °C in southeast Greenland, and becomes to $\sim 5°$ C, $\sim 3°$ C and $\sim 1.5°$ C when it travels to the northwest Greenland (Figure

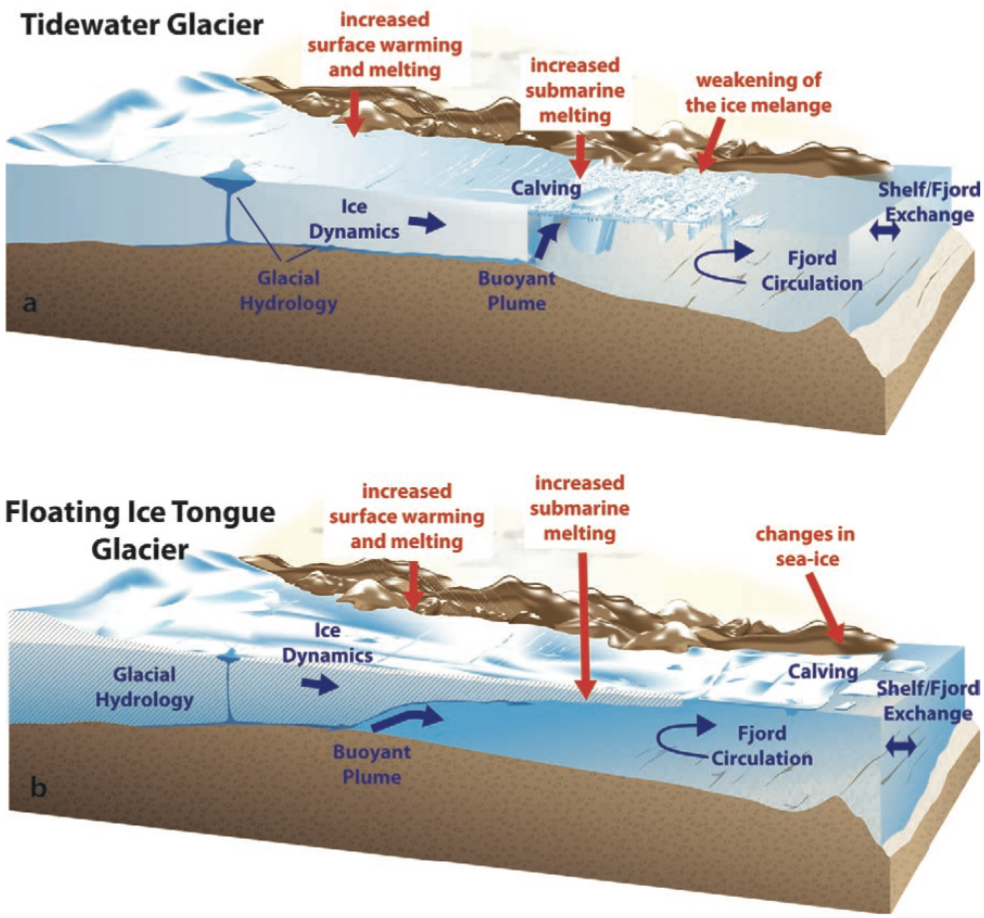

Figure 1.3: Glacier type (a) tidewater glacier and (b) floating ice tongue glacier (*Straneo et al.*, 2013).

1.4). The temperature is from the conductivity-temperature-depth (CTD) profiles collected in the vicinity of five major glaciers, which are: Nioghalvfjerdsbræ (or 79 North Glaicer), Kangerdlugssuaq Glacier, Helheim Glacier, Jakobshavn Isbræ and Petermann Glacier between 2003 to 2010 (*Straneo et al.*, 2012). The other branch of NAC travels anticlockwise to the east side of Greenland becoming Norwegian Atlantic Current, and then back along the east coast of Greenland with a temperature of $\sim 1.5°$ C at 79 North Glacier.

Widespread glacier acceleration occurred during the last decade (*Rignot and Kanagaratnam*, 2006) concurrently with a warming of nearby ocean waters leading to the suggestion that the ocean warming was the cause of the acceleration (*Holland et al.*, 2008; *Murray et al.*, 2010; *Motyka et al.*, 2011; *Rignot et al.*, 2012). If the glacier retreat was due to oceanic

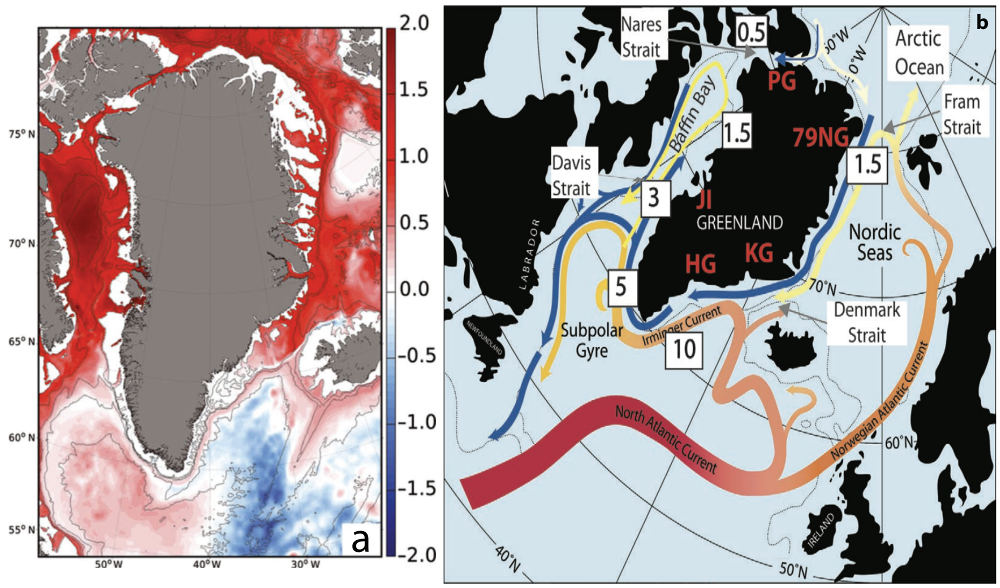

Figure 1.4: (a) Ocean temperature anomalies at 250 m from a 4 km horizontal resolution simulation by the MITgcm ocean circulation model with respect to the 1992-2009 simulation period (*Rignot et al.*, 2012), (b) Circulation of warm Atlantic (red to yellow) and cold Arctic (blue) water masses around Greenland. Numbers indicate the mean temperature (°C) of the Atlantic water on the continental shelf (*Straneo et al.*, 2012).

warming, then we may expect the changes of glacier will continue. *Yin et al.* (2011) with the climate models predicted that the maximum ocean warming around Greenland will be almost double the global mean with a magnitude of 1.7-2.0 °C. However, the mechanisms linking ocean warming and glacier retreat are still uncertain because of limited long-term observational records of glaciers and fjords and also because of a limited understanding of the relevant glacier dynamics. Water circulation and distribution in front of tidewater glaciers or underneath glacier ice shelves is determined by fjord geometry, which including its width, depth, presence or absence of shallow sills. Therefore, detailed knowledge of the continental shelf and fjord bathymetry is essential for ascertaining which glaciers are vulnerable to interannual Atlantic Water temperature variations (*Fenty et al.*, 2016).

1.3 Importance of glacier bed topography and sea floor bathymetry

Knowledge of sub-ice topography develops slowly. That is because it requires accurate measurements of the ice thickness and ocean bathymetry. Ice thickness or upper geologic features can be determined by radar, which does not work with thick ice (> 2 km), high surface clutter and temperate ice near the bottom. And it is difficult, expensive and time-consuming to collect accurate bathymetry information underneath the ice shelves or in fjords directly. Sometimes, the ocean survey is dangerous because of ice breaking-up.

Historical records suggest that humankind have explored the northern extremes since 325 BC by the ancient Greek sailor Pytheas. A driving force for the exploration of the Arctic was the desire of European monarchs to find an alternate trading route to China, either a Northwest Passage along the coast of North America, or a Northeast Passage along the coast of Siberia. With the development of navigation gears and more and more expeditions by pioneers, Arctic is not far away from us as before. In 1910-1915, the Russian Arctic Ocean Hydrographic Expedition represented an effort by the Imperial Russian Navy to explore, survey and chart the Northern Sea Route with a view to developing it as a commercial route (*Institution*, 2006). During the Cold War, people began to use nuclear submarines to collect echo sounding data in Arctic Ocean (AO). In 1993, the United States Navy and the marine research community embarked on an ambitious program called **SC**ience **IC**e **EX**ercise (SCICEX) to study the AO using nuclear-powered submarines (*Edwards and Coakley*, 2003). As the technology developed, powerful icebreakers, hovercraft (*Hall and Kristoffersen*, 2009) have been instrumental in mapping the AO sea floor. For some fjords full of sea ice or ice mélange, such as Jakobshavn Isbræ and Helheim Glacier, which cannot be accessed by commercial vessel, helicopters were used to drop depth sounders into the ocean fjord with positions taken by global positioning system (*Holland et al.*, 2008).

In 1997, a project called the International Bathymetric Chart of the Arctic Ocean (IBCAO) initiated and released its first gridded bathymetric map in 1999 of the region surrounding the Arctic Ocean (*IBCAO*, 2011). With updated new data sets collected from the circum-Arctic nations, and other data from fishing vessels, US Navy submarines and ships of various nations, the IBCAO Version 3.0 is on a 500 m grid, much greater details of the Arctic sea floor than IBCAO Version 1.0 (2.5 km) and Version 2.0 (2.0 km) (*Jakobsson et al.*, 2008). And there are much more multibeam surveys coverage in Version 3.0 ($\sim$ 11 %) than Version 2.0 ($\sim$ 6 %) (Figure 1.5) (*Jakobsson et al.*, 2012). *Rignot et al.* (2016) presents a nearly

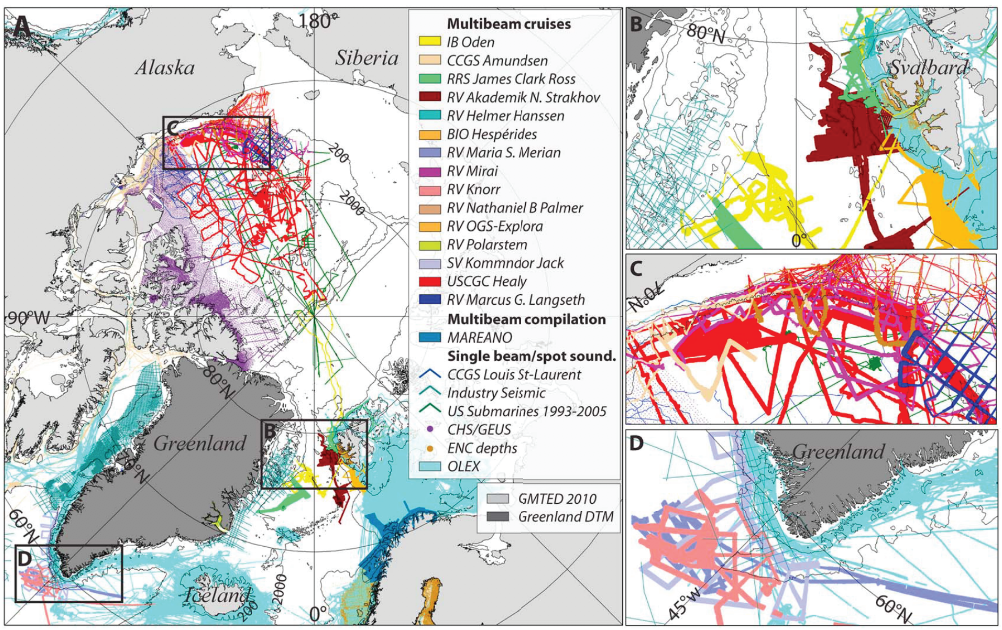

Figure 1.5: Circulation of warm Atlantic (red to yellow) and cold Arctic (blue) water masses around Greenland. Numbers indicate the mean temperature (°C) of the Atlantic water on the continental shelf (*Straneo et al.*, 2012).

complete bathymetric survey of Uummannaq and Vaigat Fjords in Central West Greenland, assembled from multibeam echo sounding data (MBES) over a 10-year period (Figure 1.6). This survey extends from the continental shelf to the glacier fronts, which is critical for understanding the glacier evolution. Inspired by the success of these mappings, NASA established a five-year Oceans Melting Greenland (OMG) mission, providing critical information about ocean-driven Greenland ice mass loss in a warming climate. In summer 2015, the first sea

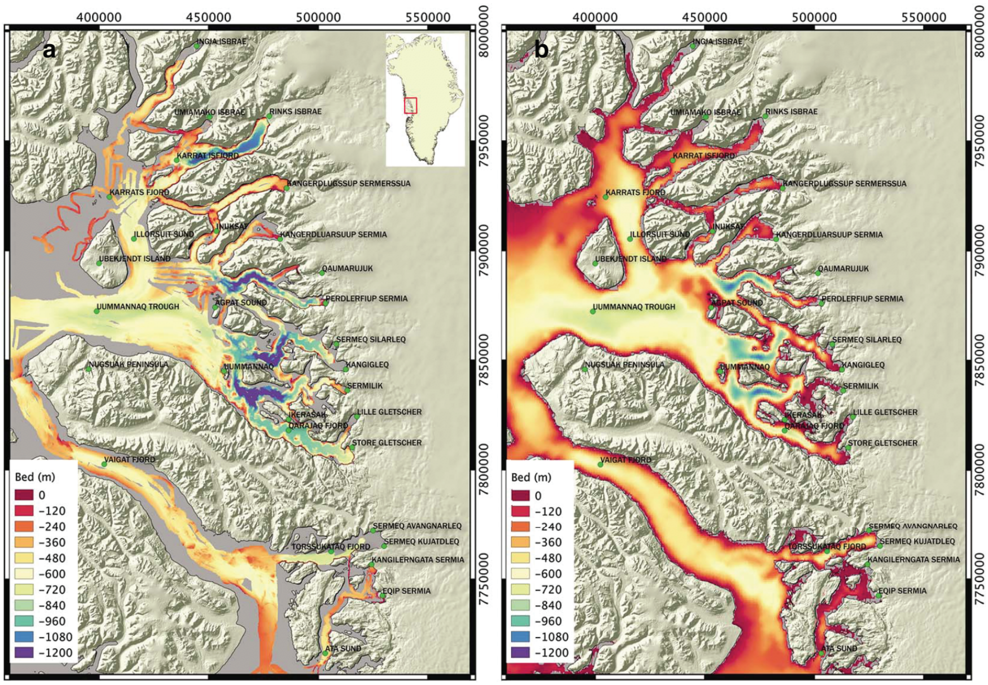

Figure 1.6: (a) Bathymetry of Uummannaq and Vaigat Fjords from MBES acquired in 2007-2014 (*Rignot et al.*, 2016). (b) IBCAO Version 3.0 (*Jakobsson et al.*, 2012).

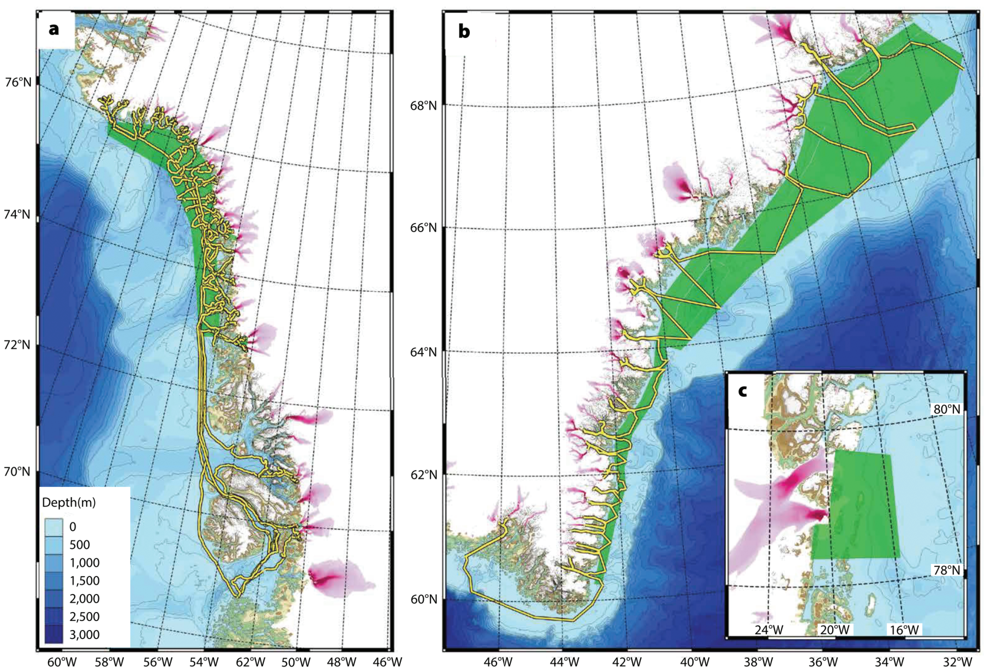

Figure 1.7: The OMG multibeam sonar ship survey in yellow lines, and airborne gravimetry (AIRGRAV) campaigns in green polygons. (a) 2015 August, (b) 2016 September, (c) northeast sector, no ship survey is possible (*Fenty et al.*, 2016).

floor measurement campaign with a ship-based multibeam sonar survey was launched to map the important shelf and glacier fjords in Northwest Greenland (*Fenty et al.*, 2016). The whole mission sea floor mapping will focus on the areas with marine-terminating glaciers in Greenland: the northwest, the southeast, and the northeast (Figure 1.7). As OMG will track the ocean conditions and ice loss for glaciers around Greenland through 2020, we will have more information then. *Morlighem et al.* (2016) using a mass conservation approach, combined OMG bathymetry with observations of ice velocity and thickness to obtain bed depth and ice thickness across the ice-ocean boundary with unprecedented accuracy and reliability. In regions where bathymetry measurements are sparse, a method conditioned by survey of terrestrial glacial valleys as well as existing sinuous feature interpolation schemes is used to generate synthetic fjord bathymetry for coastal Greenland, which is developed by *Williams et al.* (2017). With more and more accurate measurements of gravity, scientist started to use gravity data to invert glacier bed topography or fjord bathymetry. In recent studies, *Cochran and Bell* (2012) using the Parker-Oldenburg technique (*Oldenburg*, 1974) inverted the NASA Operation IceBridge (OIB) gravity data for continental shelf bathymetry beneath the Larsen Ice Shelf, Antarctica. *Greenbaum et al.* (2015) combined gravity, magnetic data and 2D, 3D models together identifying a cavity for the ocean access beneath the Totten Glacier in East Antarctica. *Gourlet et al.* (2016) used much higher resolution gravity data to investigate the ice thickness of the northern half of the Patagonia Ice fields. With OIB gravity, *Millan et al.* (2017) inferred the bathymetry of sub-ice shelf cavities in front of Pine Island, Thwaites, Smith, and Kohler glaciers in West Antarctica. In this dissertation, we mainly present 3D inversion of the gravity data along the ice fronts constrained by the MBES data at sea and the MC reconstruction inland. We evaluate the precision and uncertainty of the inferred bed elevation and compare the results with earlier mappings. We discuss the impact of the new mapping on our understanding of the recent and future evolution of these major outlet glaciers in Greenland. Details are represented in Chapter 3 and Chapter 4.

1.4 Outline of this dissertation

In Chapter 2, we present our high-resolution gravity data collected in several Greenland glaciers and glaciers of Patagonia in 2012, introduce the methods we used to interpret gravity data. In Chapter 3, 2D profile modeling on three glaciers, Petermann Glacier, Northwest Greenland and Store Glacier, Jakobshavn Isbræ in West Greenland. In Chapter 4, 3D modeling of Store Glacier, Jakobshavn Isbræ (*An et al.*, 2017), Sermeq Avangnardleq and Kujatdleq in Torssukatak Fjord in West Greenland, Helheim Glacier in Southeast Greenland. Chapter 5 summarizes the major findings of this dissertation and discusses implications for future studies.

Chapter 2

Gravity and magnetic data study and previous bathymetry study

The gravity method is a passive geophysical exploration based on the measurement of variations in the gravity field caused by the horizontal variations of density within the subsurface. And the magnetic method is the oldest and one of the most widely used geophysical techniques for exploring the Earth's subsurface since it was first used to locate the iron ore deposits in the seventeenth century. These two methods have developed rapidly over the past century because of significant technological advances and been mostly used to search out and investigate natural resources such as oil, gas and coal to fulfill human demands. There are several reasons for why the gravity and magnetic methods are so attractive to geologists and geophysicists. First, they could satisfy for application with a reasonable density and precision observation based on different measuring platforms. Second, although these methods may have a limitation in spatial resolution, which is not high enough for the entire earth, they are still useful in many regional investigations or could serve as background for the more localized studies, i.e., a glacier or an ice shelf. Last and the most important reason is gravity is especially sensitive to near vertical subsurface interfaces, which are difficult to map with other equipment like the higher-resolution ground-penetrating radar. And the measurements with seismic techniques are really time-consuming (*Cochran and Bell*, 2012).

Using satellite gravity measurements to determine the ocean floor bathymetry was presented by David T. Sandwell. The satellite cannot see the ocean floor from space directly, but the ocean surface has broad bumps and dips that mimic the topography underneath, and these sea floor features can be expressed by the extra gravitational attraction. This method is currently the only way to achieve globally uniform resolution within reasonable time and cost (*Smith and Sandwell*, 2004).

There are few studies on bathymetry based on airborne gravity data. *Studinger et al.* (2004) using aero-gravity data by US National Science Foundation's Support Office for Aero-geophysical Research (SOAR) produced the first bathymetry map covering the entire Lake Vostok in East Antarctica. NASA organized an Operation IceBridge (OIB) campaign since 2009 to monitor the cryosphere and to fill the gap between the two ICESat missions (The Ice, Cloud and land Elevation Satellite (ICESat) was launched by NASA in 2003 to monitor ice sheet mass balance using laser altimeter. Its science mission ended in February 2010. A follow-on satellite, ICESat-2, is scheduled to launch in 2018). The primary goal of gravity measurements within OIB is to 'infer bathymetry beneath ice shelves and sub-ice sheet bed topography beneath outlet glaciers that cannot be mapped by radar' (*Cochran et al.*, 2011). Utilizing the OIB airborne gravity data, bathymetry underneath the Larsen ice shelf and Thwaites glacier in Antarctica have already been determined. For Larsen C ice shelf, the geometry of the water-filled sub-ice cavity is determined by combining new bathymetry measurement with other data (*Cochran and Bell*, 2012). Determining the bed elevation for glaciers is quite different from bathymetry under floating ice shelves. Because of different scale of features being investigated and area of interests extending to grounded ice, the mass of ice itself must be included. With OIB airborne gravity data, *Tinto and Bell* (2011) had reorganized a bathymetric ridge 40 km in front of current grounding line, which is the key part of the recent ungrounding history for Thwaites glacier. *Muto et al.* (2013) used OIB gravity data combining with autonomous underwater vehicle (AUV) data to invert the height of the water column and sediment layer underneath the Pine Island Glacier (PIG) ice shelf and surrounding areas.

2.1 Data

The gravity and magnetic data I will use in my research is obtained through airborne surveys. For geologic purposes, the accuracy of gravity measurements is usually on the order of 10^-8 to 10^-9 for 0.01 to 0.001 mGal resolution of the Earth's gravitational field, for which highly sophisticated instruments and rigorous survey procedures are needed. Resolution in gravity data is commonly expressed in terms of the minimum half-wavelength that can be readily mapped in a survey provided the amplitude of the signal exceeds the accuracy limits of the observations and reductions. Resolution is a function of the measurement interval, either real or virtual *Hinze et al.* (2013, 89). In land-based measurements, the resolution is controlled by the actual data interval. However, for measurements on moving platforms, a virtual interval is the main character for resolution, which is established after required filtering to remove undesirable noise due to the platform itself. In this dissertation, we mainly focus on airborne gravity data, which the gravity data is measured by gravimeter mounted on an aircraft.

2.1.1 Data acquisition

Survey Equipments

We use airborne gravity data collected in August 2012 onboard a helicopter using the Sander Geophysics Ltd (SGL)'s airborne gravity system, Airborne Inertially Referenced Gravimeter

(AIRGrav) (*Argyle et al.*, 2000) (Figure 2.1). This helicopter is a modern twin-engine light helicopter powered by two Allison C20F turbine engine, which was outfitted with SGL's low level airborne geophysical survey instruments. A survey GPS antenna was mounted on the tail fin, clear of the rotor. The gravimeter and the survey computers were installed in the rear cabin of the aircraft. A monitor was installed above the flight instruments dashboard allowing the pilot in command to use the SGL guidance display and the navigator to operate the navigation system and ensure the acquisition system was operating under optimum parameters.

Figure 2.1: GBMF gravity survey Eurocopter AS-355 F2 helicopter and the Sander Geophysics Ltd (SGL) AIRGrav system.

The AIRGrav system achieves unprecedented spatial resolution (750 m) and precision (0.5 mGal) in gravity mapping. It is an inertially-referenced gravimeter that uses a Schuler tuned inertial platform (*Cochran and Bell*, 2012). The primary gravity sensor is the vertical accelerometer, which is held within 10 arc-seconds (0.0028 degree) to the local vertical. With suitable post-processing, the accelerometers and gyroscopes are sufficient to determine the vector gravity components to the sub mGal level (1 mGal=10^{-5} m^2/s). Another important character of AIRGrav is that it is capable of drape flying over terrain, i.e. provide reliable estimates of the free air gravity anomalies even when the system does not fly at a constant elevation (*Argyle et al.*, 2000; *Studinger et al.*, 2008). The final resolution and accuracy of the AIRGrav data depend on the survey design. Slower aircraft speed and tighter flight line spacing improve the resolution and accuracy, and more details are discussed later. Typical surveys deliver data with noise levels better than 0.5 mGal with a half sine wave ground resolution ranging from a few 100 m to a few km depending on the survey speed.

Novatel OEM4 and OEMV GPS receivers, and data loggers provide average position of the helicopter and raw range information at 10 Hz. The comparative navigation data supplied during production flights allows the for GPS corrections to be post-processed differently for every survey flight. The helicopter also carried a Riegl LD90-31K-HiP Infrared Laser Rangefinder with a range of 1,500 m, a resolution of 1 cm, an accuracy of 5 cm, and a data rate of 3.3 Hz. SGL proprietary geophysical software was used for AIRGrav data processing. As the Gordon and Betty Moore Foundation (GBMF) funded the survey, we refer to the free-air gravity anomaly data as the GBMF gravity data through all my thesis.

Survey Specifications

For Greenland, we surveyed a 250-m spacing grid for Store Glacier and 500-m spacing grids for several glaciers including Jakobshavn Isbræ (JI), at an average ground speed of 56 knots (29 m/s), with a target ground clearance of 80 m. NASA OIB surveyed Greenland with AIRGrav from year 2010 to year 2012 at a ground speed of 292 knots ($\sim$ 150 m/s) with a 500-m clearance. The slower flight speed and tighter spacing of the GBMF data yields a data grid with a spatial resolution of 750 m versus 5,200 m along-track for the OIB data filtered with a 35 s half-wavelength time filter. The spatial resolution of the GBMF data is therefore 6 times better than OIB. The parameters of two gravity surveys are listed in Table 2.1. We evaluate the measurement error of the 750-m gridded data at 0.5 mGal based on an analysis of cross-over errors.

Aircraft altitude The gravity signal decreases as 1/r, where r is the distance from aircraft to the mass responsible for the gravity. So the gravity anomaly amplitude will increase as the

Table 2.1: Survey parameters between OIB and GBMF

Variables	OIB	GBMF
Aircraft type	NASA DC-8, P-3	Eurocopter AS355-F2
Aircraft speed (knots)	140-150 (∼270-290 m/s)	56 (∼29 m/s)
Aircraft altitude (m)	500	80
Line spacing	10+ km	500 m (Store glacier is 250 m)
Grid cell size (m)	2000	200
Half-wavelength filter	35 s - 50 s - 70 s	20 s - 28 s - 36 s - 42 s
Resolution (horizontal)	5.25 km - 7.5 km - 10.5 km	514 m - 720 m - 925 m - 1079 m

increasing distance above their sources. At the same time, the short wavelength components are attenuated very fast. Thus there is a loss of resolution with increasing aircraft altitude (Figure 2.2).

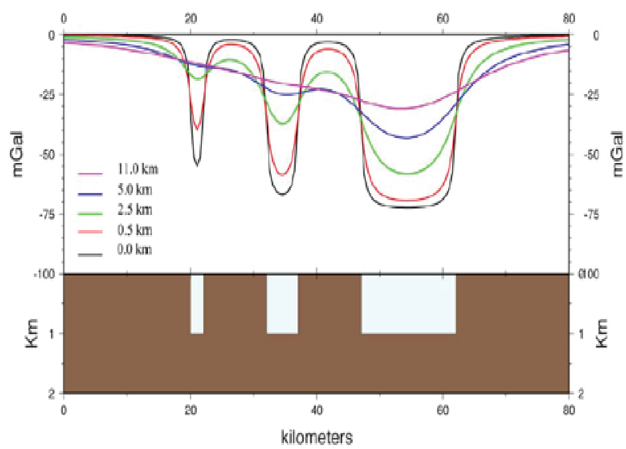

Figure 2.2: Gravity anomalies measured at different elevations above bodies with widths of 2, 5, and 15 km. Bodies are assumed to be two-dimensional and to extend from the Earth's surface to a depth of 1 km with a density contrast of 1.8 g/cm^3 (*Cochran et al.*, 2011).

Aircraft speed To get the accelerations from Earth gravity field, we need to subtract the aircraft's acceleration from the gravimeter measurements, which is computed using GPS signal. The GPS signal contains noise that is time dependent, increasing exponentially at shorter wavelength and is the dominant source of error at short wavelengths. Hence, all the gravity line data needs to be low-pass filtered in time to remove this noise (*Lowrie*, 1997). In large-scale crustal structure, the gravity anomalies due to local small bodies are of less interest that the regional anomalies, which can be enhanced by applying a low-pass filter. The spatial length of the filter is dependent on the aircraft speed. Thus, the quicker an aircraft flies, the lower resolution it obtains (Figure 2.3).

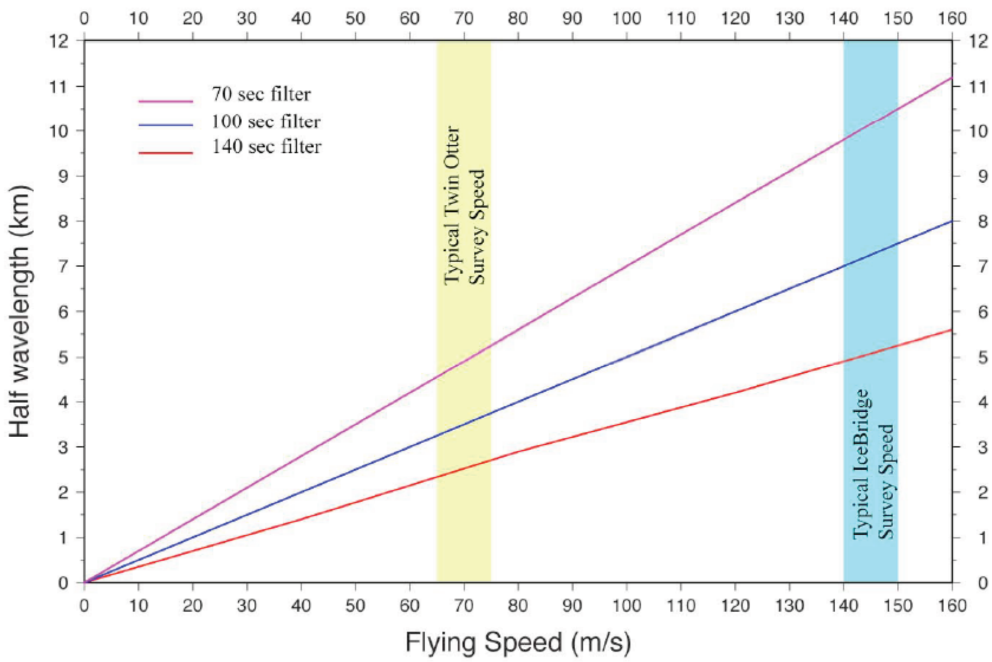

Figure 2.3: Variation of the spatial half-wavelength of th filter used in gravity data reduction as a function of aircraft speed. The blue band shows the typical range of survey speeds during OIB (*Cochran et al.*, 2011).

Flight line Gravity observations are designed to capture the gravity signature of the bedrock below the glaciers. The flight line direction varied depending on the orientation of the glacier and the surrounding terrain. Due to the irregular shape of the survey area and the roughness of the terrain, there are no definite line directions and the control lines are not always equally spaced. Line directions need to be chosen carefully to avoid steep terrain gradients, maximize glacier coverage, and to maintain uniform ground clearances. During our gravity survey, the line spacing of Store Glacier is 250 m, and for the other blocks (EqipTor, Jakobshavn Isbræ and Helheim Glacier) is 500 m. Generally, higher accuracy and shorter resolutions require closer line spacing.

Discussion

We use the GBMF data to simulate the impact of a change in aircraft speed and ground clearance on the spatial resolution, noise level, and magnitude of the gravity anomalies recorded over the JI trough as an example. Height changes are simulated by upward continuing the GBMF data to a new height of the aircraft (Figure 2.4).

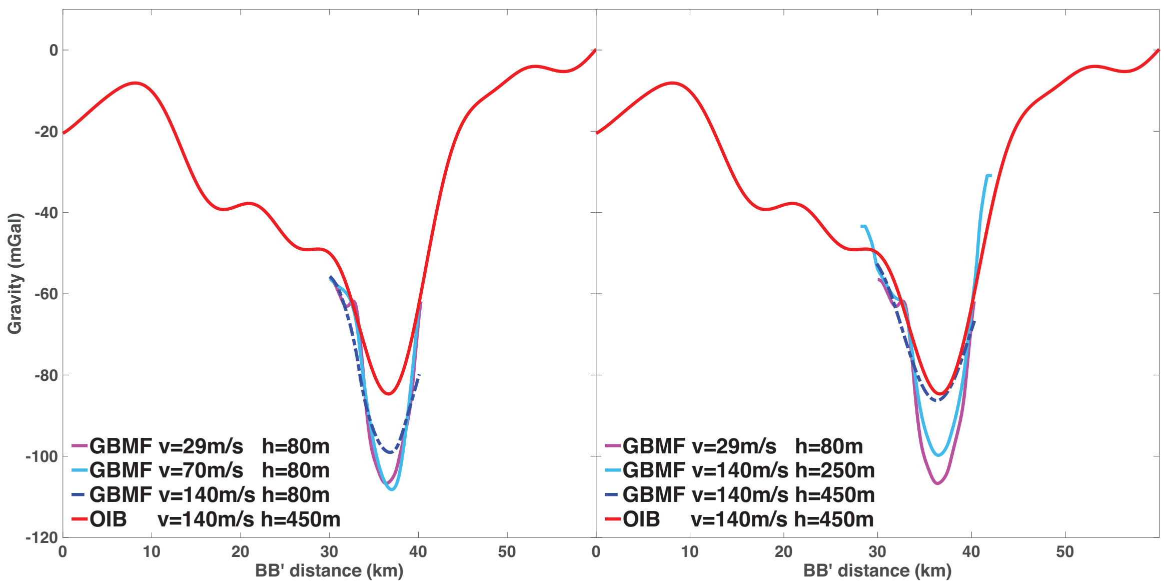

Figure 2.4: Comparison of NASA Operation IceBridge (OIB) and GBMF free-air gravity anomalies measured over Jakobshavn Isbræ (JI), West Greenland, along profile BB′ (Figure 4.17) using (a) increased platform speeds only and (b) both increased speeds and terrain clearance heights. Platform speeds are simulated using the ratio of original and target speeds to rescale a time based low pass filter. Higher terrain clearances are calculated using upward continuation of the GBMF gravity grid. The results show that the GBMF free-air gravity anomalies in the 750 m half-wavelength grid (approximately 26 s equivalent half-wavelength time filter at 29 m/s flight speed) capture the true gravity anomaly associated with the JI trough whereas the OIB 35 s half-wavelength time filter data underestimate its magnitude mainly due to a higher ground clearance and a higher survey speed.

Speed changes are simulated by increasing the duration of the time filter applied on the GBMF data. Faster speeds and higher ground clearances reduce the spatial resolution and the amplitude of the gravity anomalies recorded over the trough. We also evaluate the impact of applying different filter lengths on data resolution and data noise (Figure 2.5.

GBMF gravity data with 20, 28, 36, and 42 s half-wavelength filters provide similar gravity anomalies over the JI trough, except for a reduction in data noise for the longer filters (Figure 2.5).

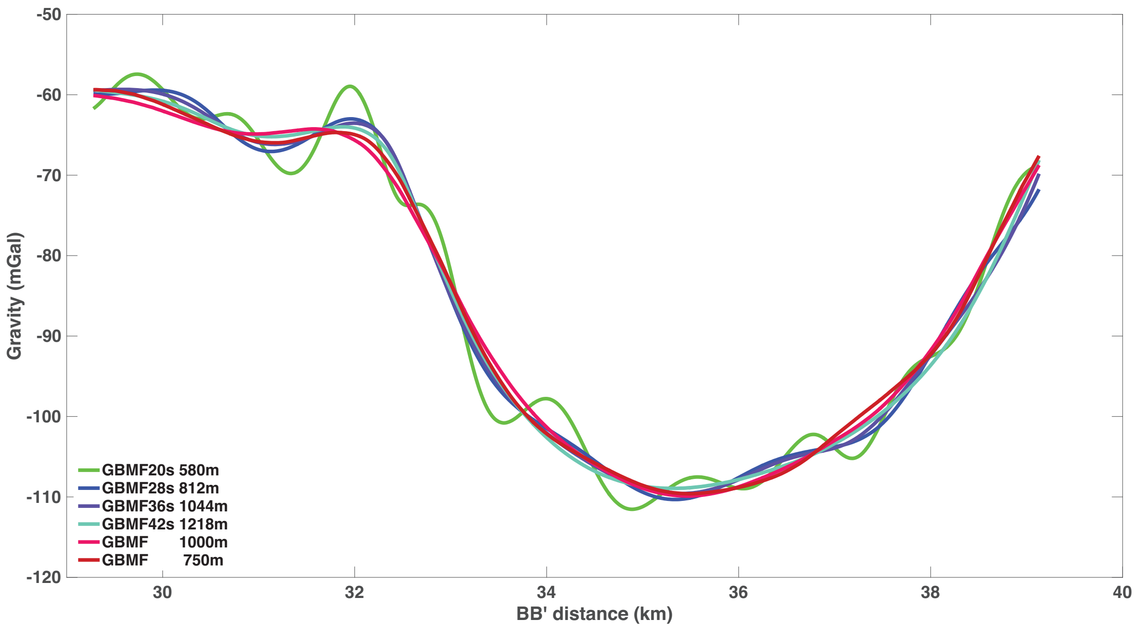

Figure 2.5: Free-air gravity anomalies recorded over Jakobshavn Isbræ, West Greenland, along a single line of data that followed profile BB′ (Figure 4.17) displayed with different half-wavelength time filters applied: 20 s (green), 28 s (dark blue), 36 s (purple), and 42 s (cyan). The length in meters indicates the corresponding half-wavelength spatial resolution for each time filter at the 29 m/s average flight speed. The gridded data, shown sampled along the same track with 1000-m (red) and 750-m (dark red) half-wavelength grid-based filter, are smoother than the equivalent time-based filter of the single line.

This similarity indicates that the GBMF data fully resolves the gravity anomaly associated with the JI trough. The gravity anomaly along profile BB′ decreases rapidly when the aircraft speed exceeds 70 m/s (Figure 2.4). At 140 m/s, the gravity anomaly is reduced by 10 mGal, which would translate into an error in bed elevation of 200 m. With the OIB data, which include both higher speed (140 m/s) and higher ground clearance (450 m), the gravity anomaly is 25 mGal too low above the JI trough, i.e. the data would yield a bed elevation 500 m too high. Changing the ground clearance has a stronger impact on data quality than changing the speed (Figure 2.4). Upward continuing the data to the OIB height reduces the gravity anomaly by 23 mGal, equivalent to 460 m of ice. Upward continuing the data to 250 m height reduces the gravity anomaly by only 8 mGal or 160 m of ice equivalent. We conclude that while there is flexibility in aircraft speed below 70 m/s, it is critical to maintain a ground clearance < 200 m to detect the gravity anomaly over JI trough within less than 5 mGal.

2.1.2 Data processing procedures

For an observation site, the observed and theoretical gravity are two fundamental components. The difference between these two is defined as gravity anomaly. There are three types of gravity anomalies: planetary, geological and filtered anomalies based on the different assumptions made in the calculation of theoretical gravity. Free-air gravity anomaly I used for my entire research is belong to planetary anomalies, which takes into account the latitudinal change in gravity on th Earth's best fitting ellipsoid represented by GRS-80 and vertical change in gravity between the reference datum and the observation height assuming that the gravity station is located in free air (*Hinze et al.*, 2013, 145).

The gravimeter mounted on the aircraft collects gravity accelerations including variations of earth gravity field and accelerations produced by aircraft motions. The gravity data are recorded at 128 Hz and are filtered and decimated to 10 Hz to match GPS measurements. Gravity is calculated by subtraction the GPS-derived aircraft accelerations from the inertial accelerations. And then the measured gravity is corrected by the theoretical gravity from the latitude at the observation point.

The free-air gravity anomaly is given as:

$$\Delta g = g_{raw} - g_{plane} - g_{normal} - g_{\text{Eötvös}} - g_{fa} - g_{sc} - g_{lc} \tag{2.1}$$

where g_{raw} is raw accelerations; g_{plane} is GPS-determined aircraft accelerations (in survey flying, accelerations in an aircraft can reach 0.1 G, equivalent to 100,000 mGal), so $g_{measured} = g_{raw} - g_{plane}$; g_{normal} is the theoretical gravity based on the latitude of the observation point; $g_{Eötvös}$ is the change in perceived gravitational force caused by the change in centrifugal acceleration resulting from eastbound or westbound speed; g_{fa} is free-air correction, which accounts for the height of the aircraft in meters above the GRS-80 ellipsoid; g_{sc} is static correction, based on static ground recordings and repeat lines; g_{lc} is the level correction, based on line intersections. Data processing must extract gravity data from this very noisy environment. The resulting anomalies are decimated to 2 Hz and low-pass filtered to avoid introducing bias in the data. All processing of the GBMF airborne gravity data was performed by SGL proprietary geophysical software.

2.1.3 Data coverage — Greenland and Patagonia

SGL conducted airborne helicopter high-resolution gravimetric survey in Greenland and Patagonia, Chile under contract with The Regents of the University of California, Irvine, for the Gordon and Betty Moore Foundation.

Greenland

The production flights commenced on August 16, 2012 and were completed on August 27, 2012. The survey blocks are located over the Eqip Sermia (EQIP), Kangilerngata Sermia (KANGIL), Sermeq Kujatdleq (KUJ), Sermeq Avangnardleq (AVA), Store, Jakobshavn Isbræ (JI) and Helheim outlet glaciers. An additional block, North Store, was included in the planning but not flown (Figure 2.6). My research mainly focuses on glaciers in Greenland.

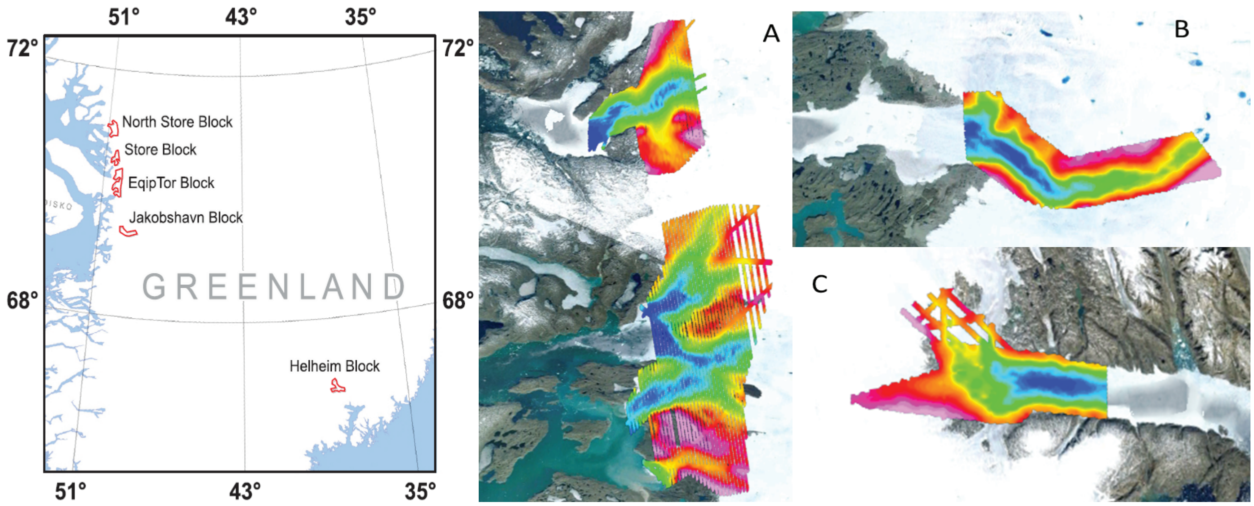

Figure 2.6: GBMF gravity survey in Greenland (left), Gravity anomalies on (A) a set of 5 glaciers north of Ilulissat, (B) Jakobshavn Isbræ in central West Greenland, (C) Helheim Glacier in East Greenland. Color coded from blue (smaller gravity anomaly) to magenta (larger gravity anomaly).

Patagonia, Chile

The survey in Patagonia was conducted in two phases, using two Eurocopter AS350 helicopters rented from Helicopters cl, registration CC-CDN (AS350 B3) and CC-ABT (AS350 B2). Production flights commenced on April 29, 2012 and were completed on November 19, 2012. A total of 9 flights were flown during the first phase (April to June, 2012) of the project and 12 flights in the second (October to November, 2012). The survey area covered most of the Northern Patagonian Ice Field (NPI) and the northern part of the Southern Patagonian Ice Field (SPI). NPI blocks include the plateau flown at lower resolution and the three blocks flown with denser line spacing named after their respective glaciers San Rafael-Qiontin, Steffen, and Colonia. SPI blocks include the plateau flown at lower resolution as well and three higher resolution blocks named Jorge Montt, O'Higgins and Occidental-Greve. All coordinates are in the WGS-84 datum, UTM zone 18S (Figure 2.7).

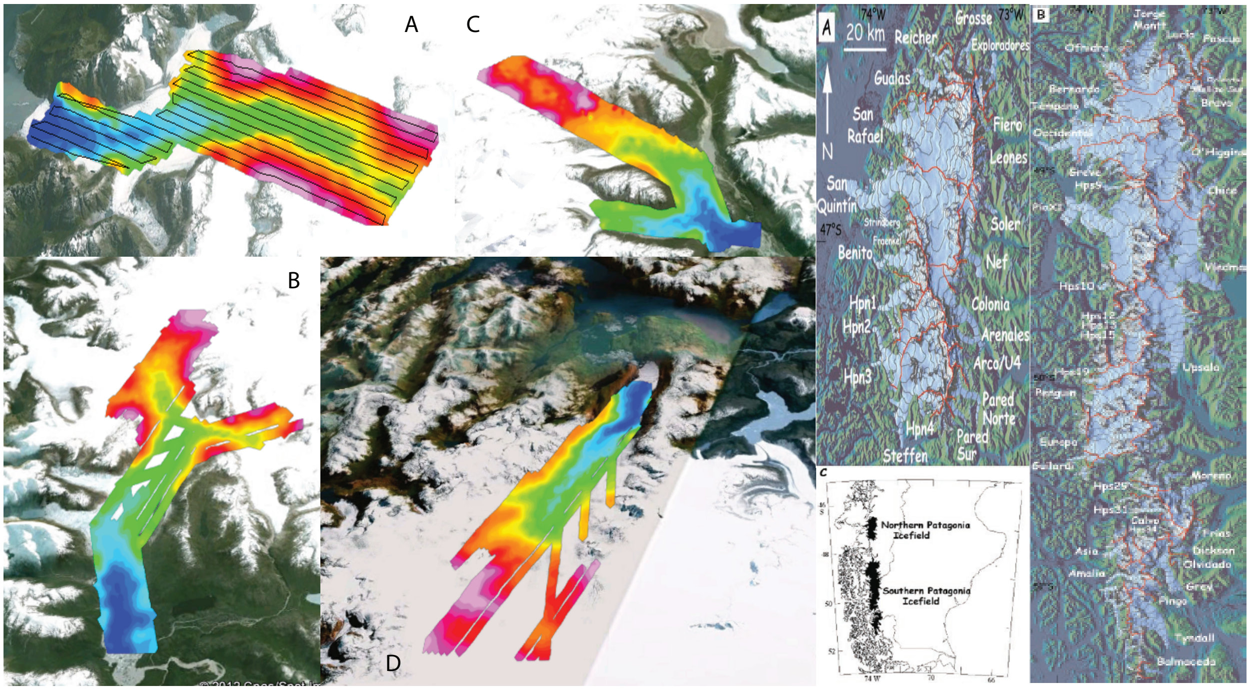

Figure 2.7: GBMF gravity survey in Patagonia (right) (*Rignot et al.*, 2003), Gravity anomalies on (A) Glacier San Rafael, to the right of Laguna San Rafael, at the northern end of NPI, (B) Glacier Steffen at the southern end of NPI, (C) Glacier Colonia on the eastern flank of NPI, and (D) Glacier Jorge Montt at the northern tip of SPI. Color coded from blue (smaller gravity anomaly) to magenta (larger gravity anomaly).

2.2 Methods

A simple gravity survey is used to isolate bedrock highs, can be interpreted in a qualitative way. However, for a complex survey when I need to determine the bedrock configuration, then a more quantitative interpretation uses inversion to quantify possible geometric and physical property parameters of the subsurface that can satisfy the observed data (*Hinze et al.*, 2013, 10). The important element of inversion is the forward model that produces a synthetic set of estimates or effects for comparison with the actual observations. Thus, an acceptable subsurface model is judged by how well the modeled effects match the observed data in amplitude and shape after an iterative process. This approach is suitable for processing a relatively small data set and a simple subsurface model, which only contains a few unknown parameters that need to be evaluated. If problems involve large numbers of observations and model unknown, then inverse modeling approaches are desirable.

2.2.1 2D and 3D models

For most interpretations, it is important to decide whether interpreting with profiles or maps. Profile interpretation is commonly performed on the main profile, which could go through the maximum or minimum amplitude of the gravity or magnetic anomaly and is perpendicular to the anomaly contours. A single profile is a relatively simple and efficient way to do interpretation; also, if there is a seismic or geologic cross-section in the same region, then profile interpretation could be the best choice. Usually, profile interpretation is described as a two-dimensional (2D) model. An assumption of an infinity extension of the geologic cross-section with no change is usually made during the profile interpretation procedure. It has proved much more fruitful to undertake forward modeling of individual profiles, using radar data over grounded areas and any available bathymetric information as tie points to constrain the models. Map interpretation assumes a finite extent of sources within the boundaries of the map. Gravity data is acquired along multiple parallel lines that are perpendicular to the anticipated strike direction of the source of interest. More commonly data can be acquired on a regular grid pattern with one grid direction perpendicular to the main geological strike of the region. However, the three dimensional (3D) interpretation methods with exhaustive details are more complex and time-consuming than 2D interpretation techniques. Thus, it is important to evaluate the contour map pattern for anomalies and determine the nature of the data before deciding which interpretation methodology will be selected.

2.2.2 Forward modeling

Talwani et al. (1959) had come up a new idea to do the gravity computations for irregular geological structures by approximating it to an n-sided polygon. Generally, any two-dimensional body can be approximated nearly to a polygon by making this polygon with enough numbers of sides. Then the vertical and horizontal gravity accelerations to this polygon could be calculated through analytical expressions at any given location. The accuracy of this computation relies on how well the polygon fits with the geological structures. Then this can be improved by increasing the number of polygon's sides, which is the method we used in 2D modeling in chapter 3.

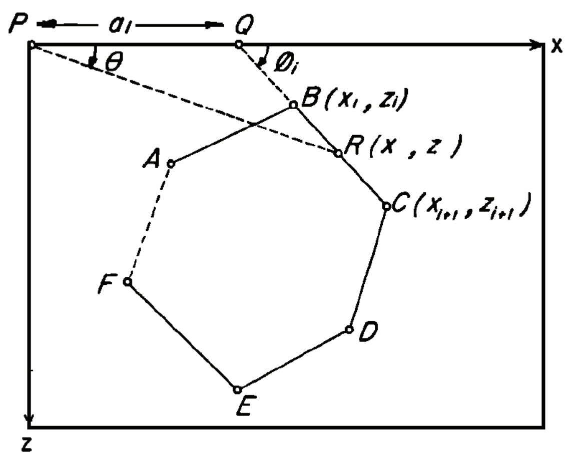

Figure 2.8: Geometrical elements involved in the gravitational attraction of an n-sided polygon (*Talwani et al.*, 1959).

In figure 2.8, ABCDEF is the given polygon with n sides and P is the point at which the gravity attraction wanted to be determined. The polygon and point P all lie in the xz planes (z is defined positive downwards). θ is measured from the positive x-axis to the positive z-axis. The vertical gravity attraction of this two-dimensional body is equal to $2G\rho \oint z d\theta$.

The integral is taken along the sides of this polygon, where G is the universal constant of gravitation and ρ is the volume density of the geological body. Similar equation to calculate the horizontal gravity attraction is given by $2G\rho \oint x d\theta$. Let $PQ = a_i$,

$$z = x \cdot \tan\theta \tag{2.2}$$

From any point R on BC,

$$z = (x - a_i) \cdot \tan\phi_i \tag{2.3}$$

From equation 2.2 and 2.3, $z = \frac{a_i \cdot \tan\theta \cdot \tan\phi_i}{\tan\phi_i - \tan\theta}$, or $\int_{BC} z \mathrm{d}\theta = \int_B^C \frac{a_i \cdot \tan\theta \cdot \tan\phi_i}{\tan\phi_i - \tan\theta} \mathrm{d}\theta \equiv Z_i$. Similarly it can be shown that $\int_{BC} x \mathrm{d}\theta = \int_B^C \frac{a_i \cdot \tan\phi_i}{\tan\phi_i - \tan\theta} \mathrm{d}\theta \equiv X_i$. Then the vertical gravity attraction V and horizontal gravity attraction H for whole polygon can be given respectively by $V = 2G\rho \sum_{i=1}^n Z_i$ and $H = 2G\rho \sum_{i=1}^n X_i$. Now if the integrals involved in Z_i and X_i are solved, then we will get the vertical and horizontal gravity attraction in the end. The most general cases can be shown as

$$Z_i = a_i \cdot \sin\phi_i \cdot \cos\phi_i \cdot [\theta_i - \theta_{i+1} + \tan\phi_i \cdot \ln \frac{\cos\theta_i(\tan\theta_i - \tan\phi_i)}{\cos\theta_{i+1}(\tan\theta_{i+1} - \tan\phi_i)}] \tag{2.4}$$

$$X_i = a_i \cdot \sin\phi_i \cdot \cos\phi_i \cdot [\tan\phi_i(\theta_{i+1} - \theta_i) + \ln \frac{\cos\theta_i(\tan\theta_i - \tan\phi_i)}{\cos\theta_{i+1}(\tan\theta_{i+1} - \tan\phi_1)}] \tag{2.5}$$

Where $\theta_i = \tan^{-1}\frac{z_i}{x_i}$, $\phi_i = \tan^{-1}\frac{z_{i+1} - z_i}{x_{i+1} - x_i}$, $\theta_{i+1} = \tan^{-1}\frac{z_{i+1}}{x_{i+1}}$, and $a_i = x_{i+1} - z_{i+1}\frac{x_{i+1} - x_i}{z_i - z_{i+1}}$. With the density of different geological bodies, the gravity attraction in both vertical and horizontal directions at a given point can be computed by the expressions above.

2.2.3 Inverse modeling

The inversion of gravity data for bathymetric relief will use Parker-Oldenburg technique (*Oldenburg*, 1974). *Parker* (1973) calculated the gravity anomaly caused by an uneven, uniform layer of material by means of a series of Fourier transforms. This expression is defines as:

$$F(\Delta g) = -2\pi G\rho \mathrm{e}^{-kz_0} \sum_{n=1}^{\infty} \frac{k^{n-1}}{n!} F[h^n(x)] \tag{2.6}$$

Where $F(\Delta g)$ is the Fourier transform of the gravity anomaly, G is the universal gravitational constant, ρ is the density contrast across the interface, k is the wave number, $h(x)$ is the depth to the interface (positive downward), z_0 is the mean depth of the horizontal interface.

Oldenburg (1974) rearranged Parker's equation that enables us to use this equation calculating the depth to the undulating interface from gravity anomaly through an iterative process, and this is the method we used in 3D modeling in Chapter 4:

$$F[h(x)] = -\frac{F[\Delta g(x)]\mathrm{e}^{-kz_0}}{2\pi G\rho} - \sum_{n=2}^{\infty} \frac{k^{n-1}}{n!} F[h^n(x)] \tag{2.7}$$

Gómez-Ortiz and Agarwal (2005) developed a MATLAB script using a grid of gravity anomalies as input employing the Parker-Oldenburg inversion. In this procedure, the values for the mean depth of the interface z_0 and the density contrast across the interface ρ need to be assumed. Hence, at the beginning, the gravity anomaly is dependent on the calculation of the Fourier transform. Then the first term of 2.7 is computed by assigning $h(x) = 0$ (*Oldenburg*, 1974) and the Fourier transform of the depth to the interface provides the first approximation of the topography interface h. The value of $h(x)$ is then used in 2.7 to evaluate a new estimate of $h(x)$ (*Gómez-Ortiz and Agarwal*, 2005). This iterative process is continued until a reasonable solution reached.

2.2.4 Discussion

In gravity applications, trial-and-error forward modeling is the most effective and widely used approach by adjusting the unknown parameters with iterative re-computation until a reasonable result is obtained between the observed and calculated anomalies. Normally, the number of unknown parameters of the forward model to be estimated is relatively small, whereas least-squares inversion is commonly applied to larger-scale inversions (*Hinze et al.*, 2013, 202). Both forward and inverse modeling are inversions that estimate unknown parameters of the assumed forward model from the known parameters and observations. Because of the ambiguity inherent in gravity interpretations, the solution is not unique. Thus, a series of sensitivity experiments is normally used in forward model by modifying important attributes to test their impact on gravity anomaly, which will be discussed in the case study later on in Chapter 3. In inversion model, there are errors in the known or assumed parameters and observations, which make the solution not unique either. Overall, constraints from geological, geophysical and other observations are needed to help us get a reasonable and effective solution from gravity anomaly.

2.2.5 Methods limitation

Gravity anomaly interpretation is relatively straightforward process compared with other gravity methods. However, each method has its own limitation. For anomaly interpretation, it will never unified because of different features of glaciers and the ubiquitous presence of data errors. Also there is an inherent source ambiguity of the gravity potential (*Hinze et al.*, 2013, 175). Although these sources of ambiguity can be controlled to a significant degree, they cannot be completely eliminated. Thus, auxiliary geological, geophysical and other constraints on the subsurface are really important to help limit the ambiguity. Shipboard bathymetry measurements are the mainly used constraints in my research. For example, Petermann glacier at 81° N in northwest Greenland, it has some shipboard bathymetry data in the vicinity of the floating ice tongue in 2003, 2007 and 2009 (*Johnson et al.*, 2011).

No matter the forward method or the inversion method is chosen during the gravity anomaly interpretation process, the free parameters are essentially to be considered. The two most concerned parameters in my model are the bed depth and rock (or sediment) density.

2.3 Geosoft — Oasis montaj

Oasis montaj is a product from Geosoft Inc., which we employ during our research to analyze the gravity data. It provides a powerful suite of modeling and analysis tools for advanced understanding of the Earth's subsurface and subsea environments (*Inc.*, 2017).

2.3.1 GM-SYS Profile Modeling

The GM-SYS Profile Modeling is a program for calculating the gravity and magnetic response from a geological cross-section model using *Talwani et al.* (1959) forward modeling method. Two-dimensional (2D) models assume the earth is two-dimensional, i.e. it changes with depth (Z direction) and in the direction of the profile (X direction; perpendicular to strike). 2D models do not change in the strike direction (Y direction). 2D blocks and surfaces are presumed to extend to infinity in the strike direction.

2.3.2 GM-SYS 3D Modeling

GM-SYS 3D Modeling is a 3D gravity and magnetic modeling software for surface-oriented models. A model is defined by one or more stacked horizontal grids with density, susceptibility, and remnant magnetization distributions specified for the layer below each surface. The calculations are based on Parker's algorithm (*Parker*, 1973).

Chapter 3

2D modeling

3.1 2D modeling on Petermann Glacier, Northwest Greenland

3.1.1 Introduction

Petermann Glacier, a large and influential glacier, drains 4% of the Greenland Ice Sheet in area in Northwest Greenland to the east of Nares Strait. If flows from southeast to northwest into steep walled Petermann Fjord at about 1 km/yr. It develops the longest floating ice tongue in the northern hemisphere whose thickness changes from 600 m at its grounding line to about 30-80 m at its front (*Rignot and Steffen*, 2008). We could roughly estimate the loss of its mass, but it is hard to identify the interaction or impression between its fjord and Petermann glacier due to one of outstanding unknowns: fjord bathymetry.

3.1.2 Data

The data applied to build the Petermann Glacier 2D bathymetry model contains three parts:

(1) Airborne gravity data from NASA OIB on 20110507.

(2) Ice thickness data from CReSIS on 20110507.

(3) Ship bathymetry data from Humfrey Melling in 2009 and 2012 and H. L. Johnson in 2003.

There are five tracks of NASA OIB airborne gravity data along the axis of Petermann glacier in 2011. The reasons why I chose these two tracks are they extended further into Arctic Ocean intersecting with marine data and also overlapped with the ice thickness data from CReSIS (Figure 3.1).

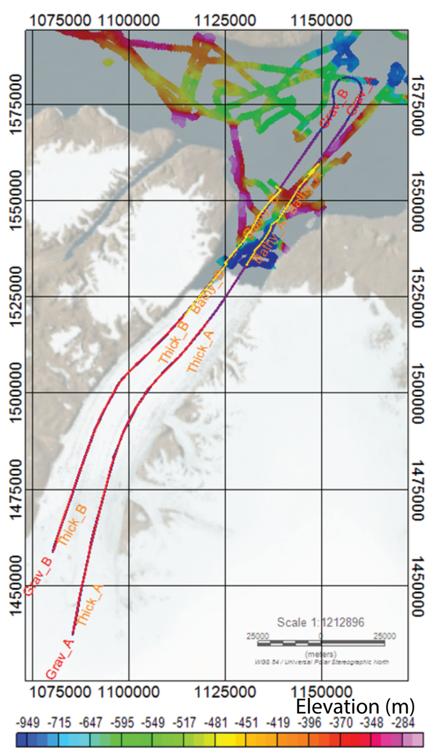

Figure 3.1: All the data sets along two CReSIS tracks on 20010507. Airborne gravity data from NASA OIB in red, ice thickness data from CReSIS in blue, and ship bathymetry data from Humfrey melling in 2009 and 2012 in yellow, and the color coded bathymetry measurements from H. L. Johnson in 2003 in meters.

3.1.3 2D profile model

A four-body forward model was used. It contained air (0 g/cm^3), ice (0.917 g/cm^3), ocean (1.03 g/cm^3) and rock (2.67 g/cm^3).

(1) First, the model was constrained by radar measurements (Figure 3.2).

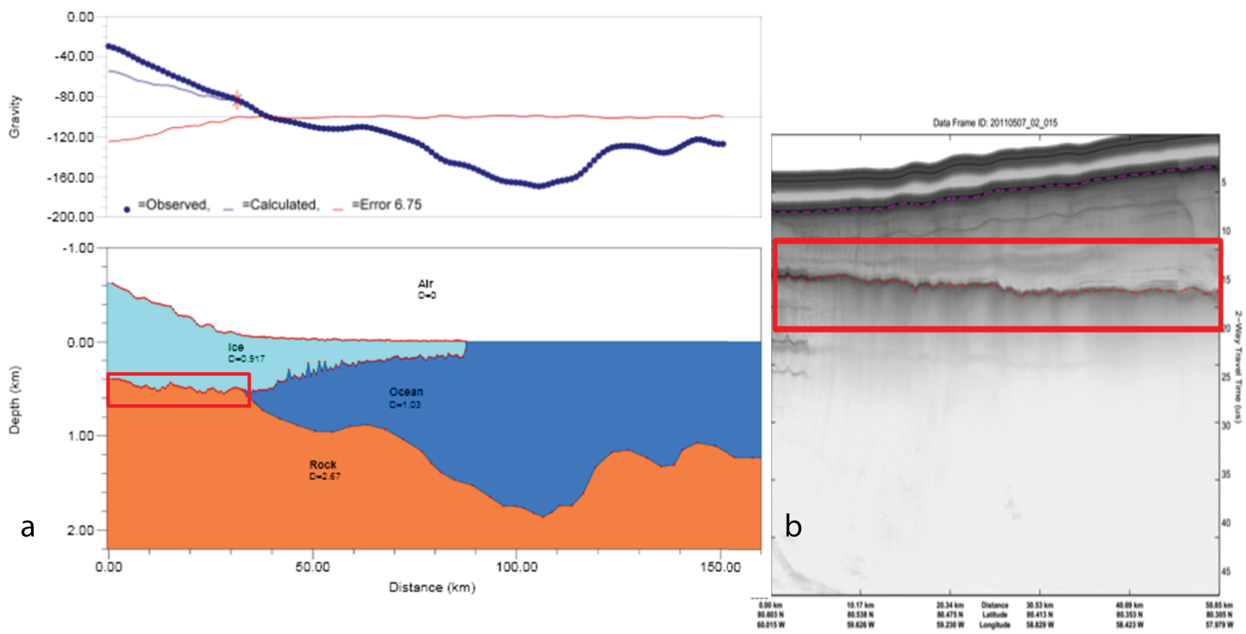

Figure 3.2: (a) The 2D profile model along survey line. Calculated gravity is shown for homogeneous bed rock of density 2.67 g/cm^3. In the top panel, blue dots represent observed gravity anomaly; blue solid line is calculated gravity anomaly; red line represents the residual between observed and calculated gravity anomaly. (b) Ice surface and bottom elevations Echo Strength Profile images from the MCoRDS radar along the survey line.

(2) Then the model was pinned to bathymetry known from marine surveys at the northwestern end of the survey line (Figure 3.3).

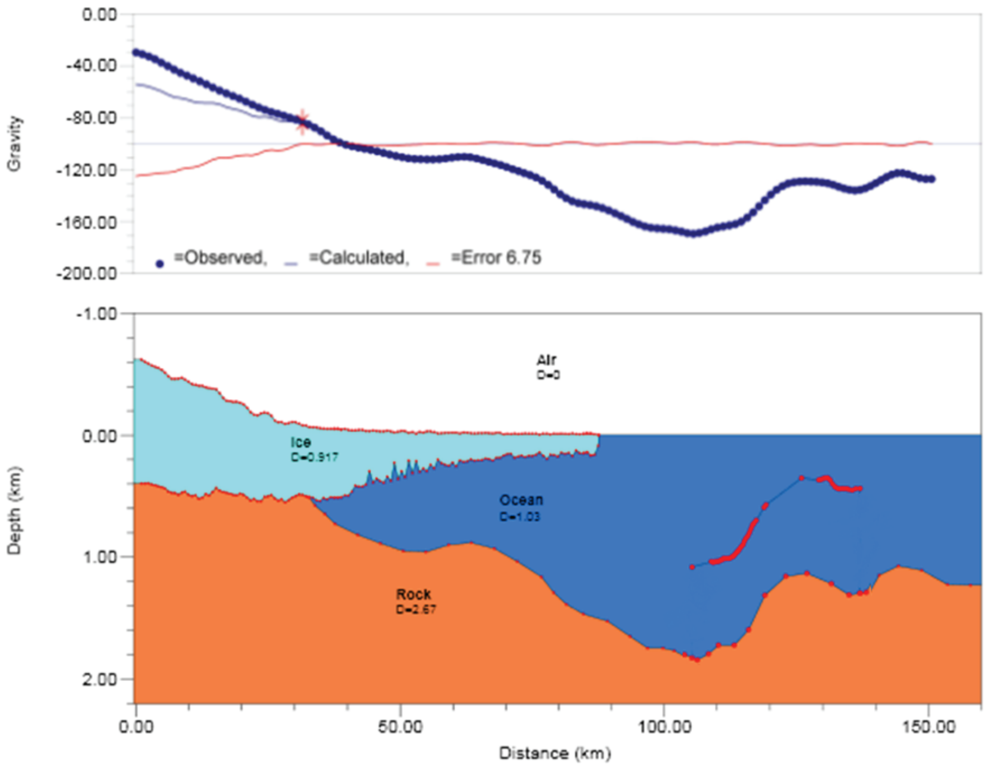

Figure 3.3: Shipboard bathymetry measurements in red dots are introduced into the 2D profile model along survey line in the bottom panel. In the top panel, blue dots represent observed gravity anomaly; blue solid line is calculated gravity anomaly; red line represents the residual between observed and calculated gravity anomaly.

The bathymetric surface must be constrained below the base of ice, and bed topography was considered homogeneous (rock density 2.67 g/cm^3) at first. The gravity-based bathymetric model has a similar shape to the observed gravity in Figure 3.2. Then after adding the shipboard bathymetry data into model, we modified the bed in order to fit these well-known constraints. However, large residuals appeared at the grounded ice (calculated gravity is much smaller than observed gravity) (Figure 3.4a). This indicated that denser rocks need to be included to account for the residual anomalies (Figure 3.4b).

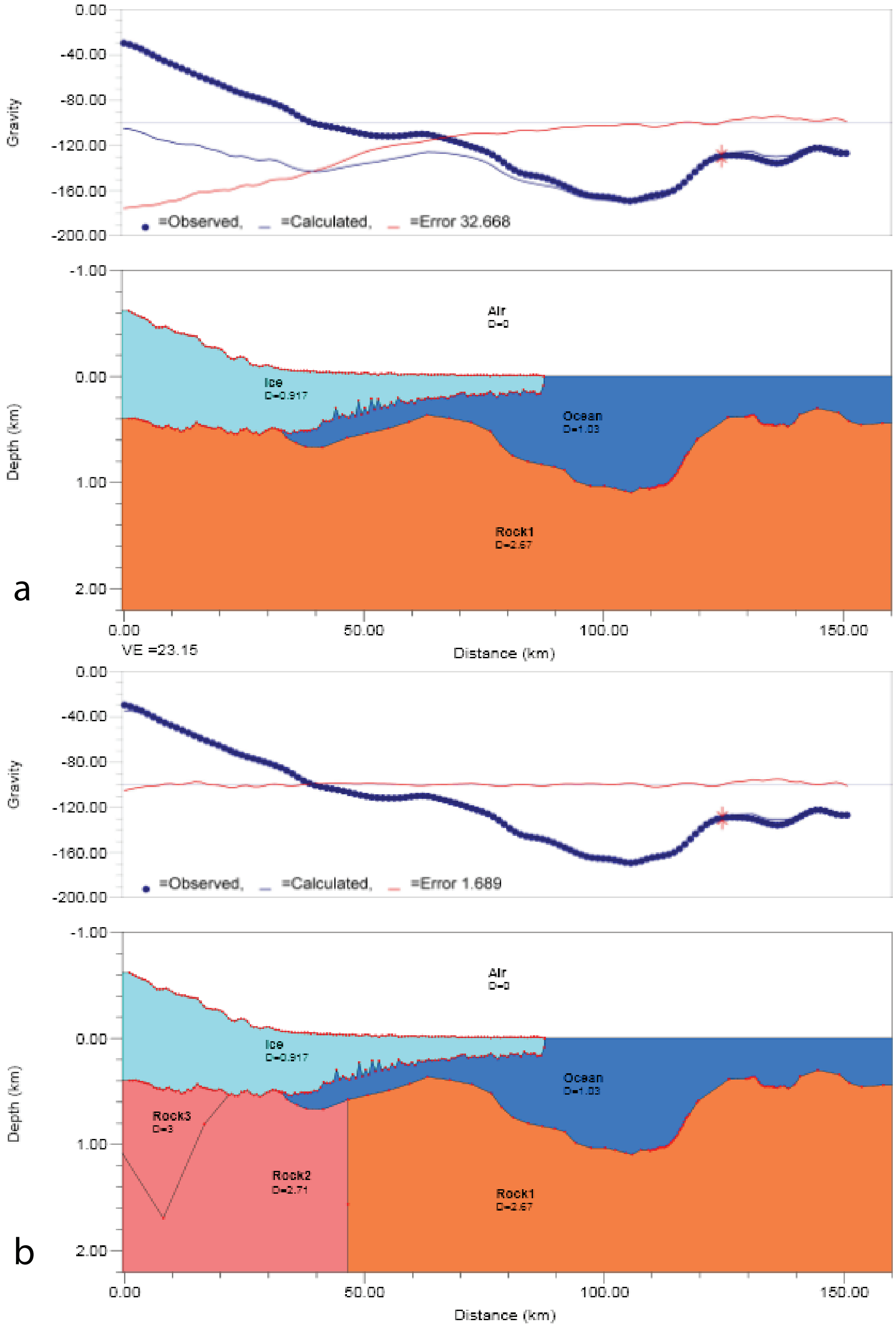

Figure 3.4: (a) The 2D profile model along survey line with big gravity residual anomaly after shipboard bathymetry measurement constraint of homogeneous rock density. (b) Denser rock introduced in the model offers varying solution. In the top panel for each figure, blue dots represent observed gravity anomaly; blue solid line is calculated gravity anomaly; red line represents the residual between observed and calculated gravity anomaly.

3.1.4 Sensitivity experiments

Rock density needs to be constrained by local geology (Figure 3.5) (*Pedersen et al.*, 2013).

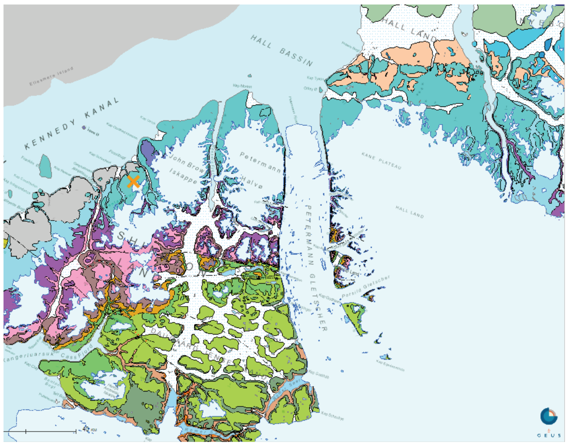

Figure 3.5: Geological data of Petermann Glacier from the Geological Survey of Denmark and Greenland (GEUS).

The dominant two types of rocks that lay onshore are Cape Calhoun limestone (purple in Figure 3.5) and Cape Clay limestone (green in Figure 3.5) formed the late and early Ordovician period, respectively. Rock density variations due to geological structures. It is possible to identify in an accurate way, but not only considering current constraints. Magnetic data could be introduced.

A residual gravity anomaly over grounded ice can be accounted for by the existence of denser rock on the ridge. The density of the second rock is changed by 0.1 g/cm^3 each time and testing at a fixed rock topography is done to determine how gravity changes. The best-fit density for the second rock is 2.71 g/cm^3 (Figure 3.6). The magnetic data is applied in a future study to determine the rock boundary quantitatively by *Tinto et al.* (2015).

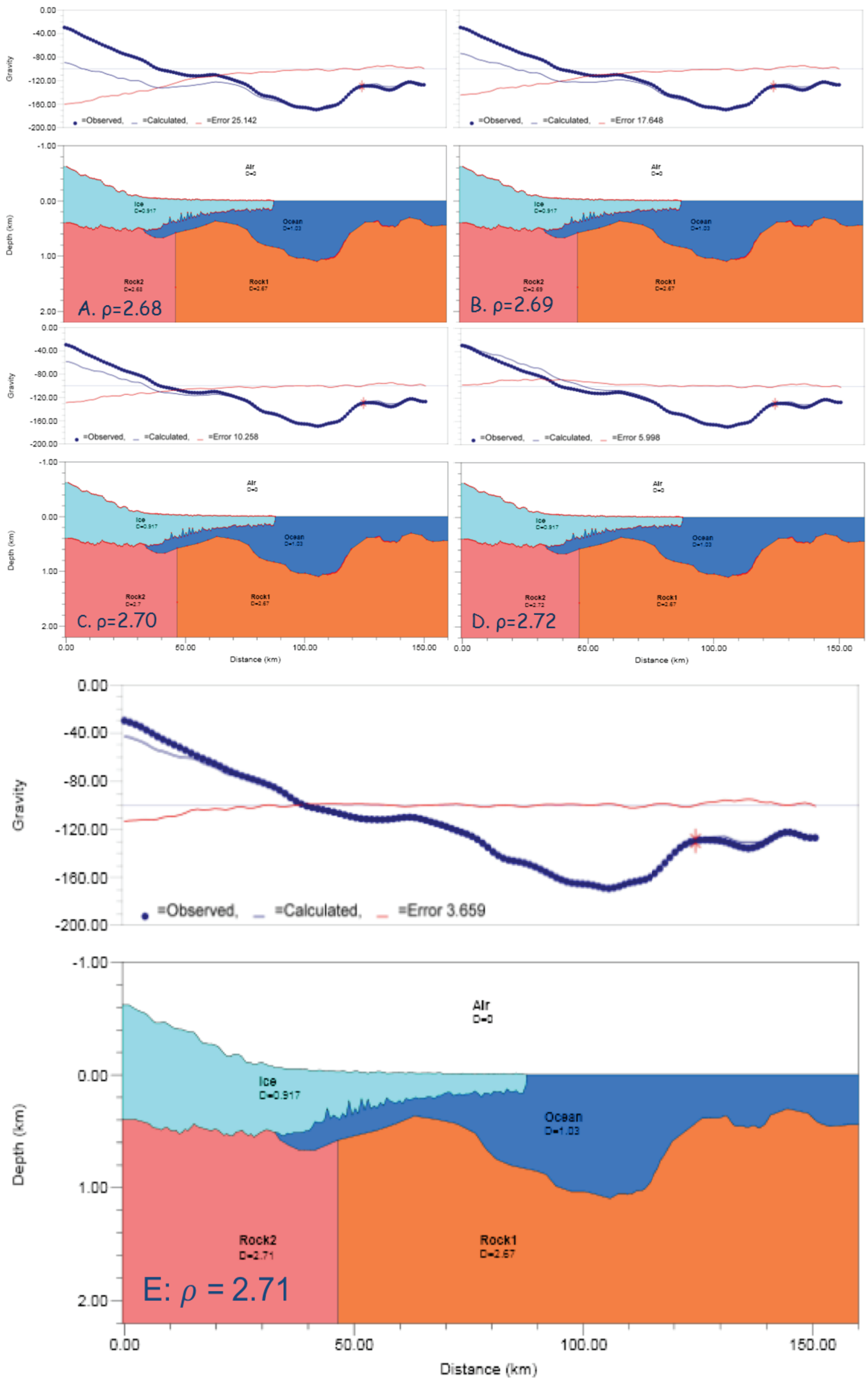

Figure 3.6: Density sensitivity experiments changed every 0.1 range from 2.67 to 2.72 g/cm^3. (a) 2.68 g/cm^3, (b) 2.69 g/cm^3, (c) 2.70 g/cm^3, (d) 2.71 g/cm^3, (e) 2.72 g/cm^3.

3.1.5 Petermann Glacier bathymetry map

The apparent feature of the gravity-based bathymetric model for Petermann glacier is a continuous sill traverse the head of the fjord aligned with the onshore ridge. Based on the models results along these two survey lines, Petermann glacier fjord has asymmetry topography, which the eastern side of the fjord is deeper that the other side. Around 25 km from grounding line, a second sill appears on the western side, which is about 450 to 300 m high.

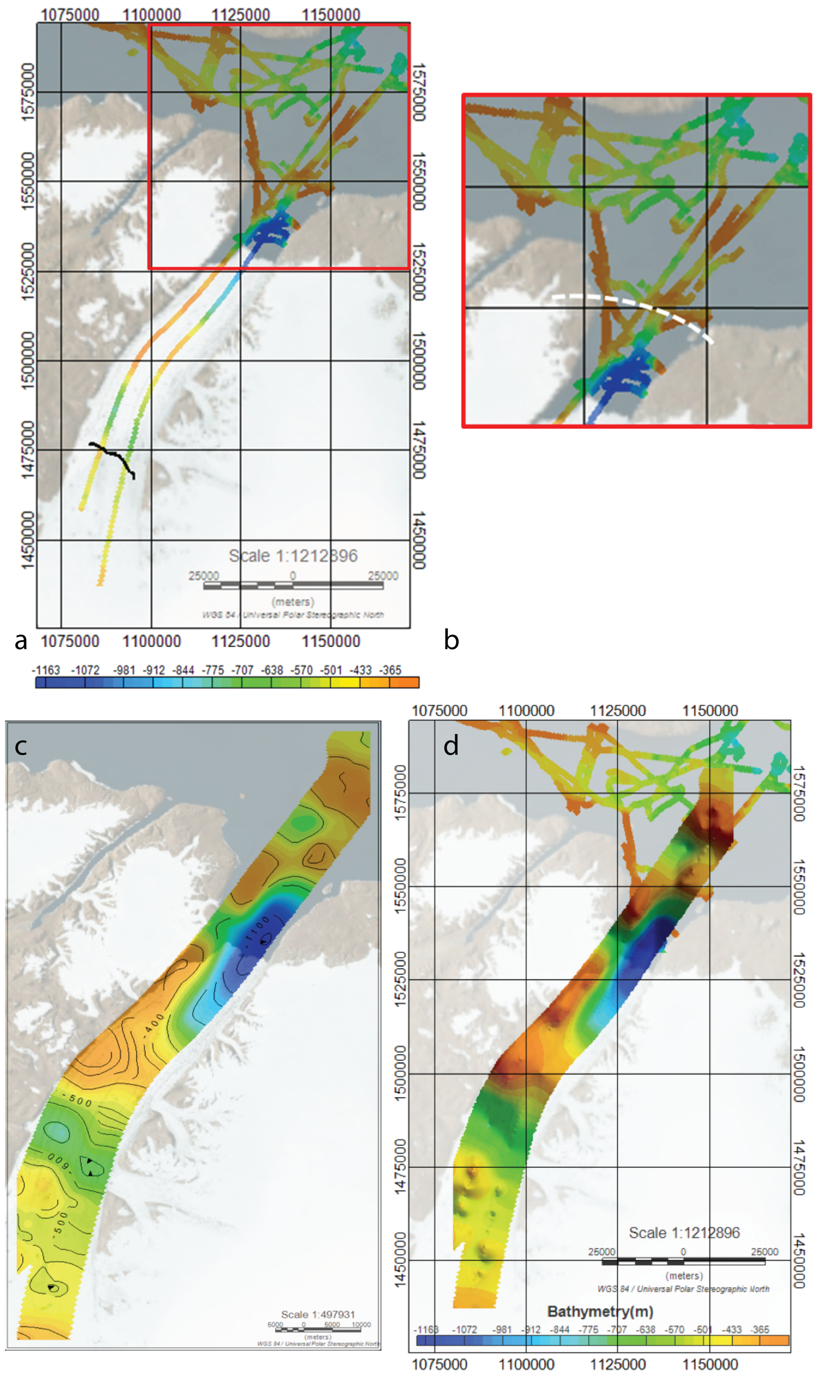

Figure 3.7: The new bathymetry map derived from OIB data in 2D model with marine constraint in meters. (a) Two OIB profile 2D model results, (b) Zoom in for the red box in (a) of the front of Petermann Glacier, (c) Interpolated map with two profiles with contour line in black every 100 m, (d) Shaded bed elevation map with measured bathymetry in the glacier front. Color coded from deep blue (1000 m below sea level), yellow (500 m below sea level) to orange (300 m below sea level). All maps overlaid on a Landsat image. Projection is WGS84/Universal Polar Stereographic North.

3.2 2D modeling on Jakobshavn Isbræ, West Greenland

Jakobshavn Isbræ in West Greenland, is the largest and most active outlet glacier. The velocity is 20 m/day (*Rignot and Mouginot*, 2012) and is a major contributor to sea level rise. To have a preliminary interpretation of gravity data, based on the calculation, here we use an approximation 1 mGal being equivalent to 25 m of ice to compare the GBMF and OIB gravity data (Figure 3.8) with three CReSIS lines on 20090401 (*Leuschen et al.*, 2010, updated 2017) (Figure 3.9). There are four overlapping lines between GBMF and OIB gravity data (Figure 3.10) flying across Jakobshavn Isbræ's trough. 2D gravity models also made with Geosoft GM-SYS Profile Modeling for three of them (Figure 3.11).

The results show major improvement in accuracy and resolution compared to the OIB data. OIB gravity data has limitations for resolving the depth of the toughs in the middle of Jakobshavn Isbræ due to the coarse resolution ($\sim$ 5.2 km). The comparison with thickness data from radar sounding is encouraging that these data will be useful to infer glacier ice thickness in the most challenging parts of Greenland where uncertainties remain high. In the main trough of Jakobshavn Isbræ, the new data confirm discrepancies in ice thickness mapping from radar near glacier front. *Bamber et al.* (2013) yields estimates of the bed depth that too shallow compared with the result of *Morlighem et al.* (2013) mass conservation (MC), which is also called BedMachine v1 and inversions from high resolution gravity data. The standard deviation between MC and GBMF inversion is about 400 m. The difference is larger that the uncertainties of the other methods and indicates a failure of the kriging method. Results of MC and GBMF do not agree perfectly, which is due to the uncertainties from density and depth of sediments layer and also mixture of sea water and ice. 3D gravity model is made for Jakobshavn Isbræ, more details discussed in Chapter 4.

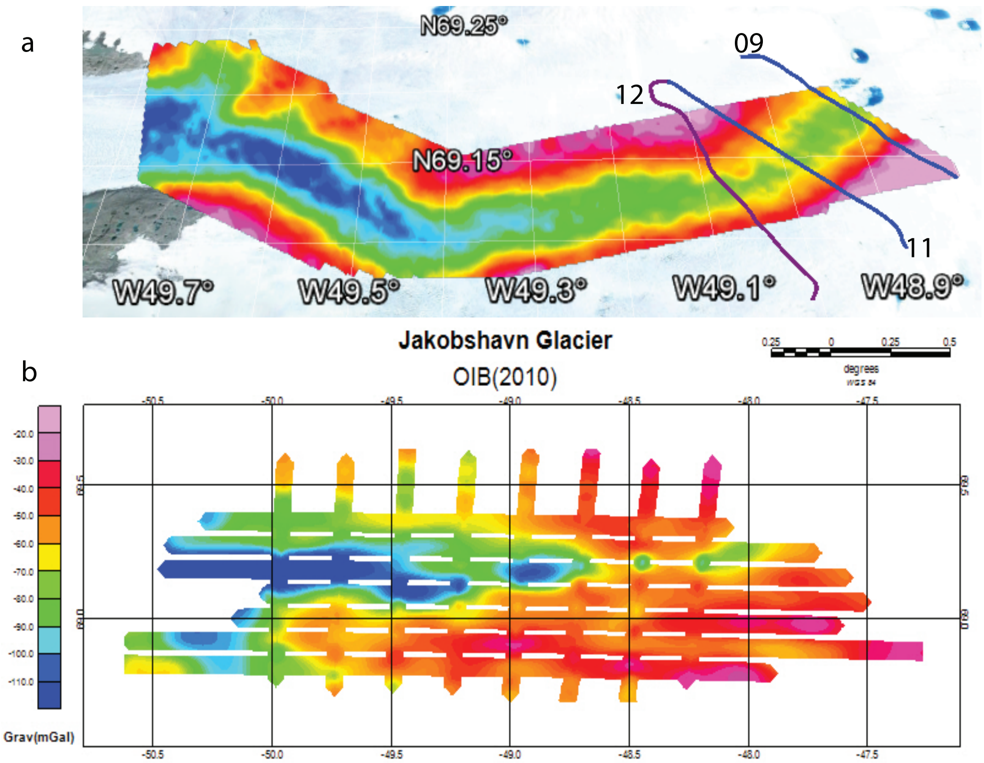

Figure 3.8: Comparison gravity maps (a) new data obtained in August 2012 (average cross over error = 0.00134), and the locations of there profiles from CReSIS on 20090401 (b) data collected by NASA Operation IceBridge (OIB) in 2010 (average cross over error = 0.9109) of Jakobshavn Isbræ, Central West Greenland.

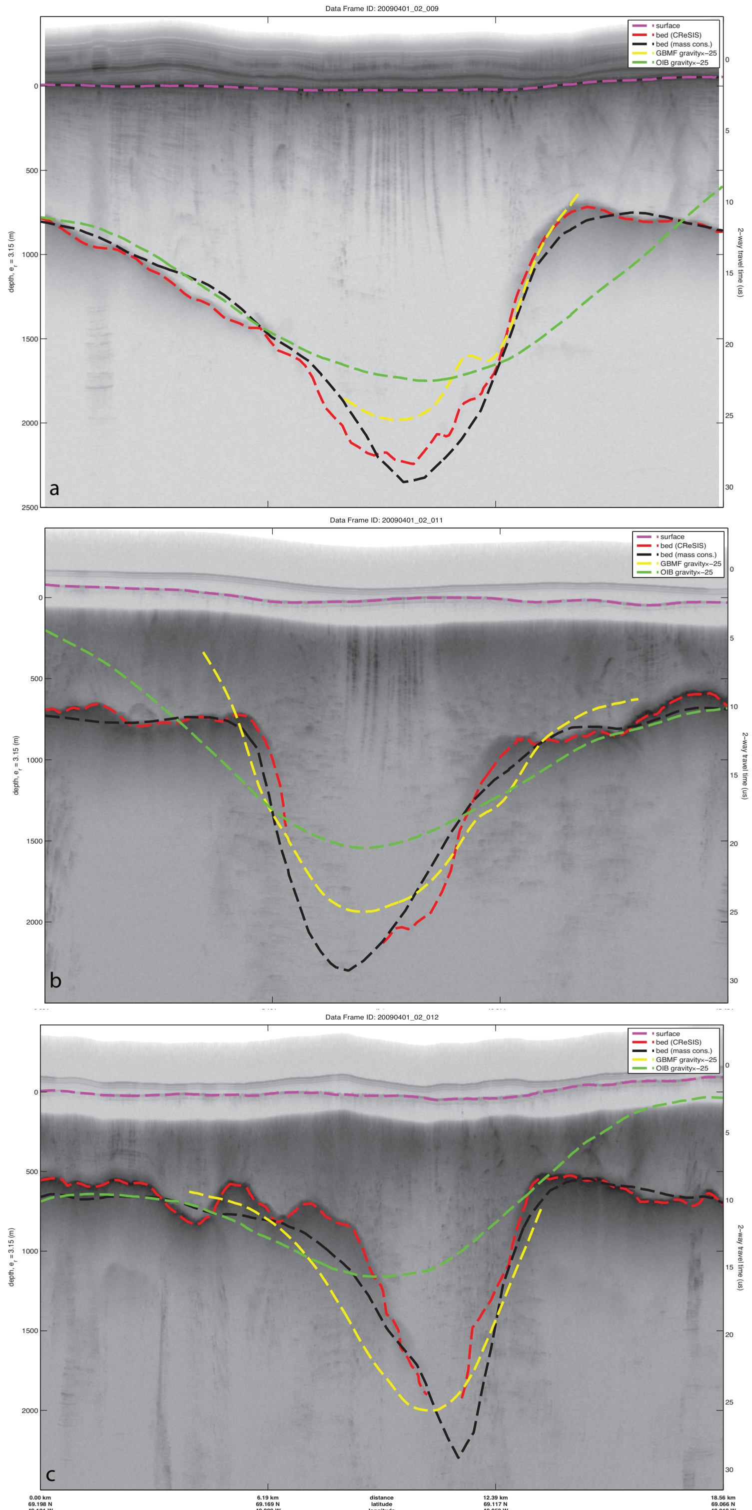

Figure 3.9: Three profiles comparison between gravity inversion's thickness (GBMF and OIB), CReSIS bottom elevation and bed elevation from mass conservation. (a) CReSIS 20090401_02_009 (b) CReSIS 20090401_02_011 (c) CReSIS 20090401_02_012, CReSIS surface (magenta), CReSIS bed (red), MC (black), GBMF (yellow), OIB (green).

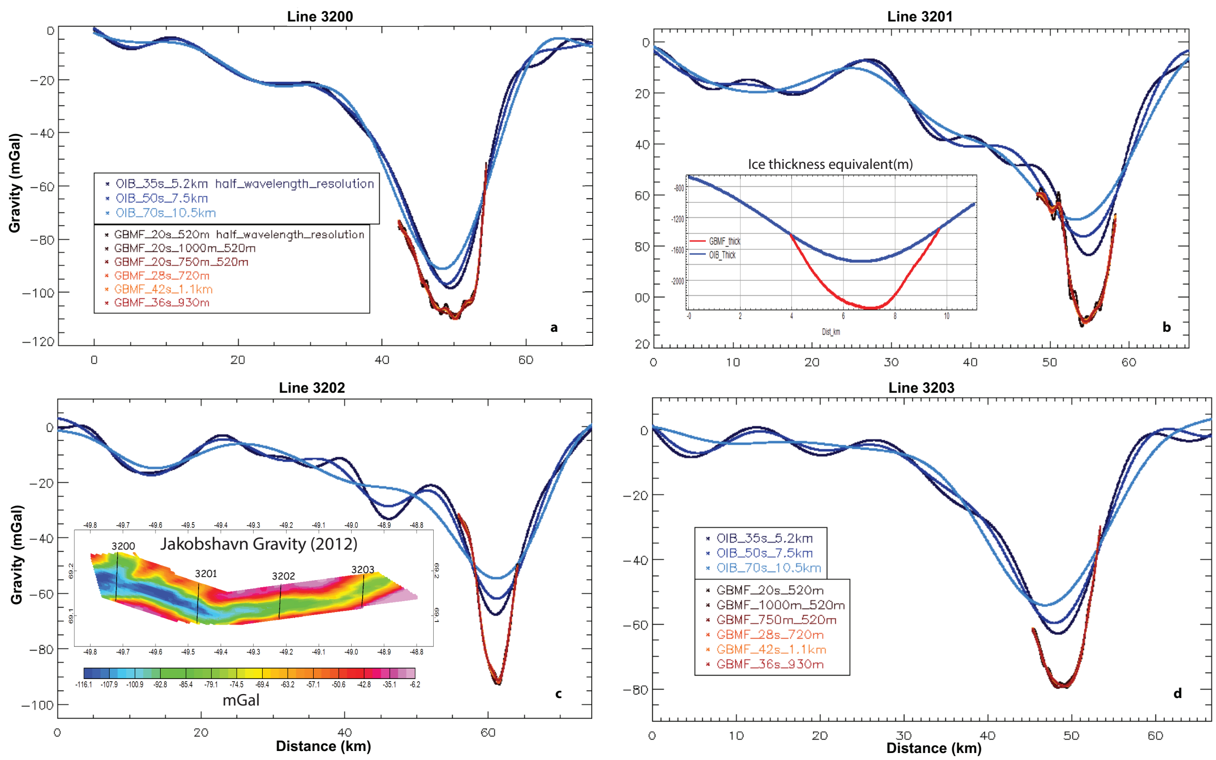

Figure 3.10: Four overlapping profiles from GBMF and OIB free-air gravity anomaly comparison. Locations of these profiles are showed in (c)'s intersected figure with Jakobshavn Isbræ's GBMF gravity anomalies. Another intersected figure of Ice thickness equivalent for GBMF and OIB in (b). (a) GBMF Line 3200 vs. OIB 20120421_08, (b) GBMF Line 3201 vs. OIB 20120421_11, (c) GBMF Line 3202 vs. OIB 20120421_14, (d) GBMF Line 3203 vs. OIB 20120421_17.

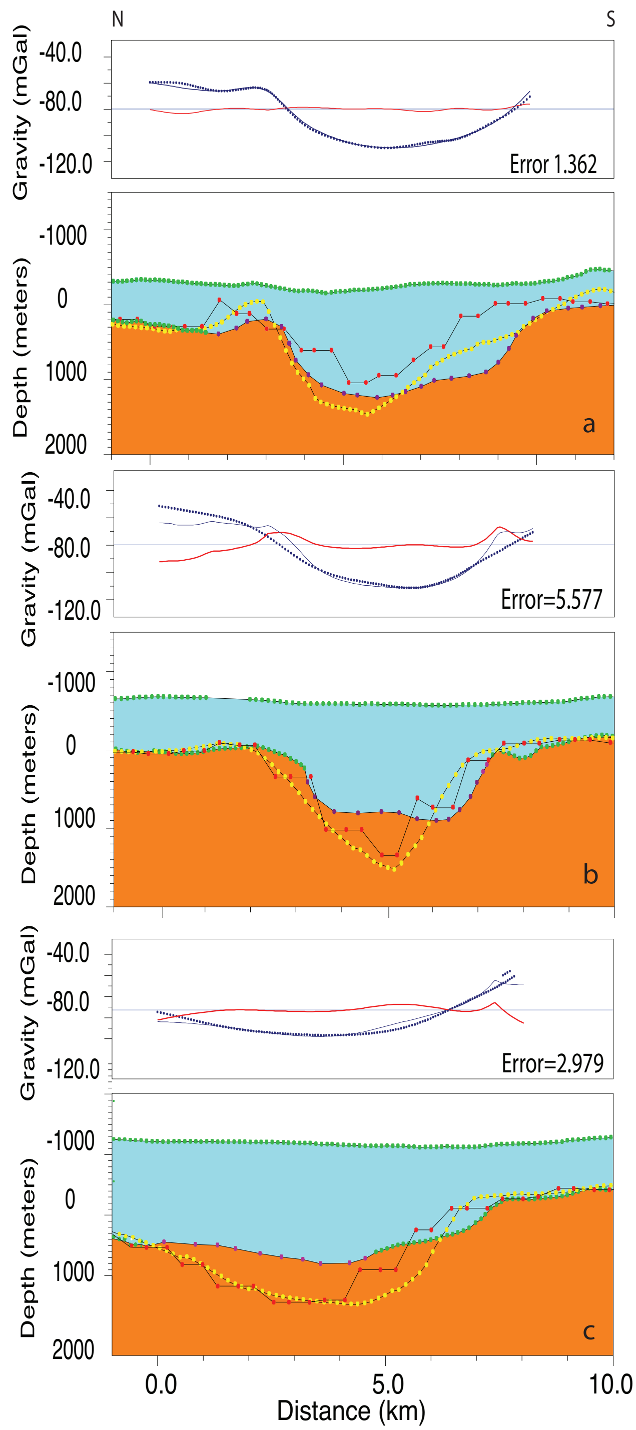

Figure 3.11: 2D gravity models with GM-SYS (a) line 3201, (b) line 3202, (c) line 3203. Observed gravity (blue dots), Calculated gravity (blue solid line), Error (red solid line), ATM_surface (black line with dark green dots), CReSIS_bed (black line with lighter green dots), BedMachine v1 (black line with yellow dots) (*Morlighem et al.*, 2013), *Bamber et al.* (2013) bed elevation (black line with red dots), GBMF inverted bed (black line with purple dots), ice density is 0.917 g/cm^3, rock density is 2.72 g/cm^3.

3.3 2D modeling on Store Glacier, West Greenland

Store glacier is a major tidewater glacier in west Greenland, which drains an area of 30,000 km^2 into Uummannaq Fjord at a speed of 4.8 km/yr (*Rignot and Mouginot*, 2012). This glacier is 5 km wide at the ice front, with a freeboard height of 70 m (*Howat et al.*, 2010) and a draft of 500 m below sea level. The ice front position has been relatively stable for the past century (*Weidick and Bennike*, 2007) with a seasonal fluctuation about 400 m (*Howat et al.*, 2010). Similar 2D models with Geosoft GM-SYS Profile Modeling were made for Store Glacier as did for Jakobshavn Isbræ (Figure 3.12).

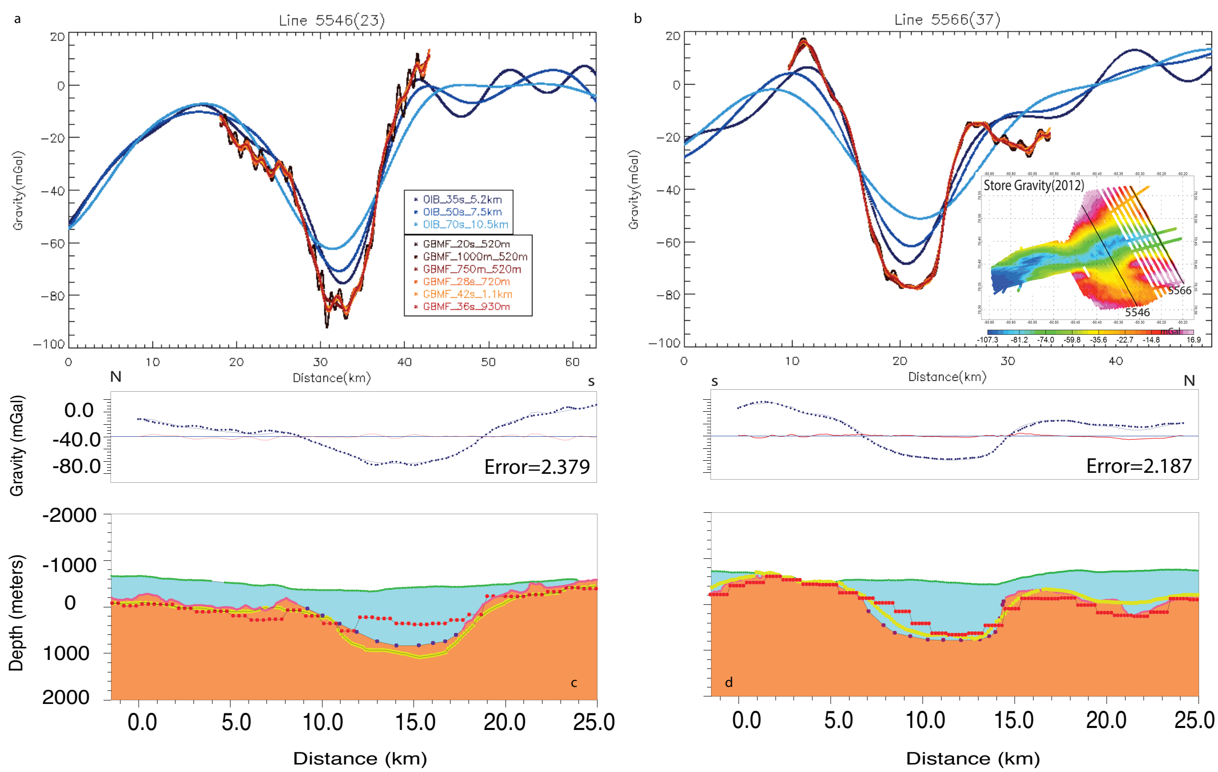

Figure 3.12: Two overlapping profiles from GBMF and OIB free-air gravity anomaly comparison (a) GBMF L5546 vs. OIB 20120430_23 and (b) GBMF L5566 vs. OIB 20120430_37. Locations of these profiles are showed in (b)'s intersected figure with Store Glacier's GBMF gravity anomalies. 2D gravity models with GM-SYS of same lines (c) and (d). Observed gravity (blue dots), Calculated gravity (blue solid line), Error (red solid line), ATM_surface (black line with dark green dots), CReSIS_bed (black line with lighter green dots), Mass conservation bed (black line with yellow dots) (*Morlighem et al.*, 2013), *Bamber et al.* (2013) bed elevation (black line with red dots), GBMF inverted bed (black line with purple dots), ice density is 0.917 g/cm^3, rock density is 2.67 g/cm^3.

3.4 Discussion

DC-shift To remove the edge effect during the calculation of gravity, a constant or DC-shift must be applied to the calculated gravity to match the observed data. The DC-shift is used to normalize a model response to take account of the differences between the observed mean value and the calculated mean value of the model response. In the gravity example, the DC-shift has an important role, since the modeling approach required a very large model space (60,000 km wide and 50 km deep) (*Tinto and Bell*, 2011). For gravity, this is necessary because the calculated value is an absolute gravity calculation for the model extending to 30,000 km in the ±X and ±Y directions, and to some arbitrary depth (50 km). Observed gravity data are generally corrected for the reference geoid, or referenced to some local datum.

Errors in gravity model The errors of these gravity-based bathymetry models include three parts:

- Instrument errors

  The instrument errors in the bathymetric model under floating ice tongue are from the gravity measurements. Under grounded ice part, errors arise from radar based ice thickness measurements.

- Modeling errors

  The modeling method required a large model space, which is 60,000 km wide and 50 km deep to remove the edge effects for calculating of gravity effect from the four bodies. There is also an offset between the model space and the observed values. The shift is determined by pinning the model to a point of known bathymetry. Hence, a suitable selection for this pinning point from the shipboard bathymetry controls the modeling errors.

- Geologic errors

  The geologic errors are crucial and difficult to avoid due to the unknown geology in different areas. And it is hard to decide a boundary between different kinds of rocks. The interpretations of gravity and magnetic data are not unique solutions (i.e. several Earth models can produce the same gravity and/or magnetic response). Furthermore, many solutions may not be geologically realistic. So these two methods need to employ in conjunction with other geophysical methods and available known data observations, which may include geology and other measurements.

Limitation of 2D modeling There are several advantages of 2D forward modeling. First, the forward modeling, it performs very quick to give insights on the range of data that satisfies the gravity model and also the parameters of sensitivity experiments. In addition, during the trial-and-error inversion processes, it will provide considerable practical insights into the subsurface informations to the investigators. However, difficulties also exist. There is no reliable error statistics for the final solution. Also the processes of trial-and-error are relatively intolerably laborious. Hence, for more complicated problems especially with a large numbers of unknowns, inverse modeling is commonly used.

Chapter 4

3D modeling

4.1 3D modeling of Store Glacier, West Greenland

4.1.1 Introduction

Many of Greenland's glacier frontal regions have been changing rapidly in recent decades and have resulted in a significant loss of mass from the Greenland ice Sheet which is increasing with time. Many posit that these changes in mass coincide with an increase in ocean heat along the coastal margin, yet we don't know the details of this interaction and in particular we do not know the geometry of the glaciers and of the sea floor at the transition boundary. Glacier thickness is not well known because existing radar sounders have difficulties probing the bed of rough, entrenched, warm ice; and bathymetry is not known in most glacial fjords.

Here we use a combination of measurements to reconstruct the bed elevation, ice thickness and water depth at the transition boundary between land and ocean of Store Glacier, Greenland. Store is a major glacier that flows at 4.8 km/yr into Uummannaq Fjord (*Rignot and Mouginot*, 2012). We measured the fjord bathymetry in August 2012 and 2013 using multibeam echo sounding (MBES) data. OIB collected ice thickness data between 2008 and 2012 on this glacier as well. Finally, we deployed the AIRGrav gravity instrument in August 2012 on a helicopter to obtain high resolution gravity. The gravity grid is 250 m spacing around the glacier snout and 500 m inland.

4.1.2 Gravity Inversion

Data All the data available to use for Store (Figure 4.1b):

(1) Airborne gravity data for Store glacier with GBMF in 2012 (magenta lines).

(2) Ice thickness data from CReSIS 20120421, 20120429 and 20120430 (red lines).

(3) Shipboard bathymetry data in 2013 (blue grid).

(4) Mass conservation solution *Morlighem et al.* (2013).

Using the Cape Race vessel, we conducted a bathymetric survey of the water in front of Store Glacier using a Reson 8160 Multi-Beam Echo Sounding (MBES) system operating at 50 KHz. The MBES is operated with a NAVCOM 3050 differential GPS unit with sub-meter position accuracy, and an Applanix POSMV inertial navigation system, which provides real time vessel attitude and position. The data acquired using the QINSy software and processed using the CARIS HIPS software. Calibration of sound speed is water is performed using Conductivity Temperature Density (CTD) data obtained at regular intervals during the cruise, and by surveying a set of topographic features on the sea-floor at different look angles. The output sea-floor bathymetry products were generated on a 25-m grid, with a vertical precision of 1-2 m. Fjord surveys were conducted at a speed of 5 knots, and less than 1 knot along the ice front (*Rignot et al.*, 2015).

Radio echo sounding of Store Glacier using the Multi-channel Coherent Radar of Ice Sheets (MCoRDS) from the University of Kansas provides constraints on ice thickness in the upper reaches of the glacier. In the terminal valley, no bed echoes have been retrieved from the data due to high surface clutter presumably combined with the high water content of the ice. The nominal precision of these data is about 10 m over the flat interior but no more than 30-50 m at low elevation over rough terrain (*Morlighem et al.*, 2013; *Wu*, 2014, e.g.). These radio echo sounding-derived thickness data were combined with ice motion vectors derived from satellite radar interferometry (*Rignot and Mouginot*, 2012) using a mass conservation approach to obtain a seamless, gridded representation of the bed topography at 150 m spacing over the image domain in Figure 4.9c.

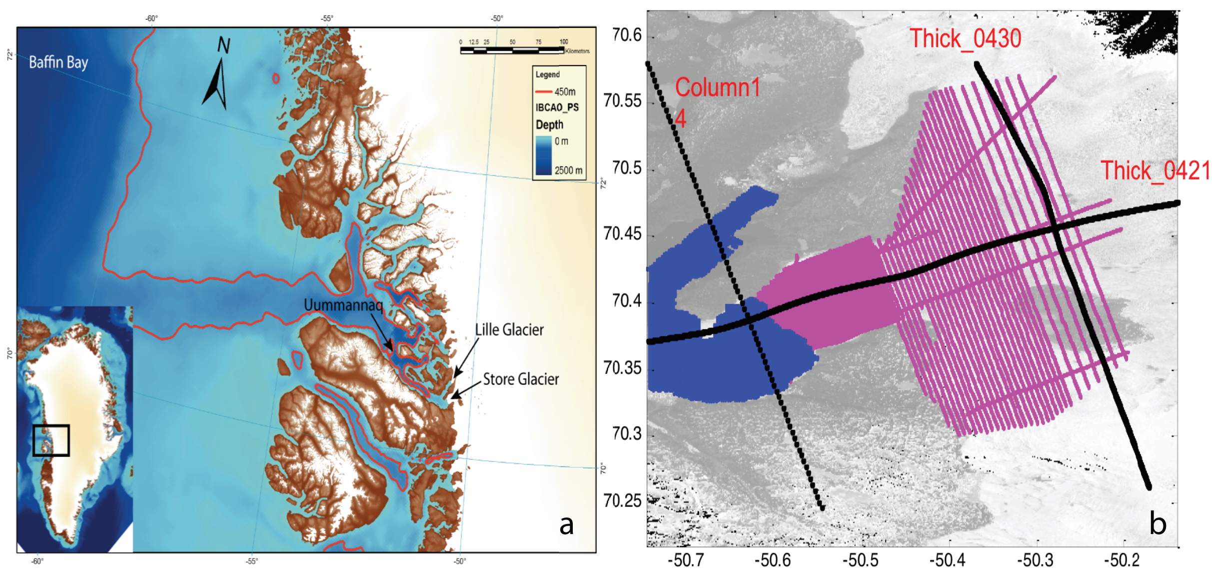

Figure 4.1: (a) Position of Store Glacier, West Greenland by Nolwenn Chauché, Centre of Glaciology, Aberystwyth University, UK `https://www.aber.ac.uk/greenland/iceberg.shtml`. (b) All datasets used in gravity inversion for Store Glacier, 2012 glacier ice front in cyan, overlaid on a Landsat image.

Geological information of Store Glacier To define an optimal average density for the glacier bed, we check the geological information from GEUS and with a series of sensitivity experiments to get the best solution in terms of the misfit between modeled and initial gravity fields for densities varying from 2.58 to 2.73 g/cm^3, with the presence of granodioritic and gabbro respectively in this area (*Pedersen et al.*, 2013) (Figure 4.2). We find a minimum at a density of 2.67 g/cm^3.

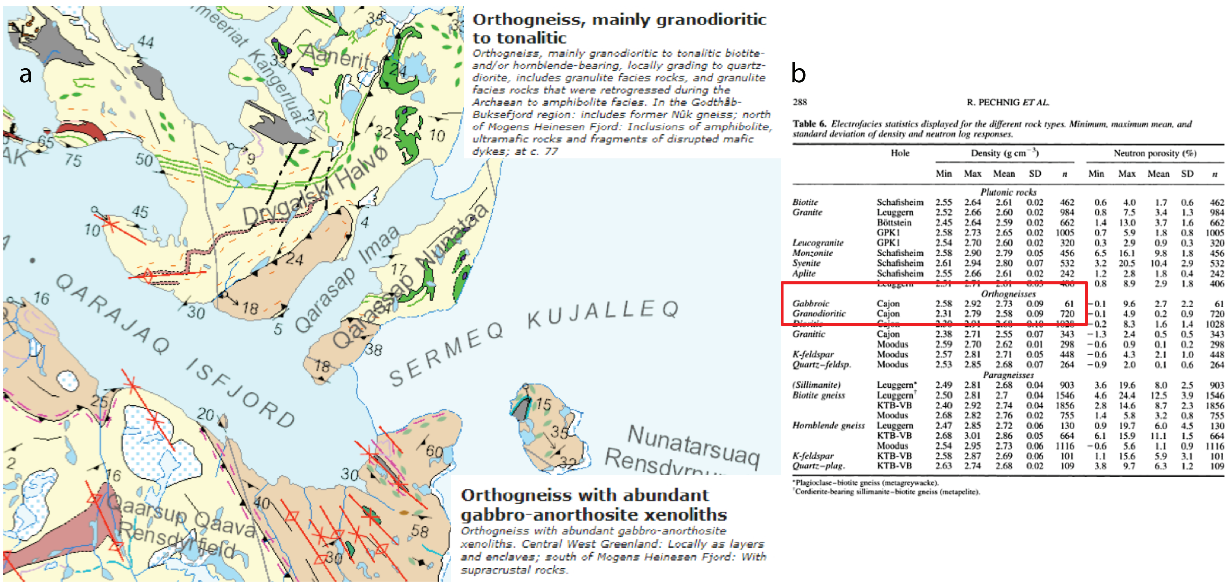

288 R. PECHNIG *ET AL.*

Table 6. *Electrofacies statistics displayed for the different rock types. Minimum, maximum mean, and standard deviation of density and neutron log responses.*

	Hole	Density (g cm^{-3})					Neutron porosity (%)				
		Min	Max	Mean	SD	*n*	Min	Max	Mean	SD	*n*
				Plutonic rocks							
Biotite	Schafisheim	2.55	2.64	2.61	0.02	462	0.6	4.0	1.7	0.6	462
Granite	Leuggern	2.52	2.66	2.60	0.02	984	0.8	7.5	3.4	1.3	984
	Böttstein	2.45	2.64	2.59	0.02	662	1.4	13.0	3.7	1.6	662
	GPK1	2.58	2.73	2.65	0.02	1005	0.7	5.9	1.8	0.8	1005
Leucogranite	GPK1	2.54	2.70	2.60	0.02	320	0.3	2.9	0.9	0.3	320
Monzonite	Schafisheim	2.58	2.90	2.79	0.05	456	6.5	16.1	9.8	1.8	456
Syenite	Schafisheim	2.61	2.94	2.80	0.07	532	3.2	20.5	10.4	2.9	532
Aplite	Schafisheim	2.55	2.66	2.61	0.02	242	1.2	2.8	1.8	0.4	242
	Leuggern	2.51	2.71	2.61	0.03	406	0.8	8.9	2.9	1.8	406
				Orthogneisses							
Gabbroic	Cajon	2.58	2.92	2.73	0.09	61	−0.1	9.6	2.7	2.2	61
Granodioritic	Cajon	2.31	2.79	2.58	0.09	720	−0.1	4.9	0.2	0.9	720
Dioritic	Cajon	2.30	2.91	2.68	0.10	1028	−0.2	8.3	1.6	1.4	1028
Granitic	Cajon	2.38	2.71	2.55	0.07	343	−1.3	2.4	0.5	0.5	343
	Moodus	2.59	2.70	2.62	0.01	298	−0.6	0.9	0.1	0.2	298
K-feldspar	Moodus	2.57	2.81	2.71	0.05	448	−0.6	4.3	2.1	1.0	448
Quartz–feldsp.	Moodus	2.53	2.85	2.68	0.07	264	−0.9	2.0	0.1	0.6	264
				Paragneisses							
(Sillimanite)	Leuggern*	2.49	2.81	2.68	0.04	903	3.6	19.6	8.0	2.5	903
Biotite gneiss	Leuggern†	2.50	2.81	2.7	0.04	1546	4.6	24.4	12.5	3.9	1546
	KTB-VB	2.40	2.92	2.74	0.04	1856	2.8	14.6	8.7	2.3	1856
	Moodus	2.68	2.82	2.76	0.02	755	1.4	5.8	3.2	0.8	755
Hornblende gneiss	Leuggern	2.47	2.85	2.72	0.06	130	0.9	19.7	6.0	4.5	130
	KTB-VB	2.68	3.01	2.86	0.05	664	6.1	15.9	11.1	1.5	664
	Moodus	2.54	2.95	2.73	0.06	1116	−0.6	5.6	1.1	0.9	1116
K-feldspar	KTB-VB	2.58	2.87	2.69	0.06	101	1.1	15.6	5.9	3.1	101
Quartz–plag.	KTB-VB	2.63	2.74	2.68	0.02	109	3.8	9.7	6.3	1.2	109

*Plagioclase–biotite gneiss (metagreywacke).
†Cordierite-bearing sillimanite–biotite gneiss (metapelite).

Figure 4.2: (a) Geological information of Store Glacier from Geological Survey of Denmark and Greenland (GEUS). (b) Rock density table of related rocks in this area from *Harvey* (2005, 288).

Gravity Inversion from Muto's model

Methods For the inversion of free-air gravity anomalies for bathymetry and sediment thickness layer, the forward model is followed *Plouff* (1976) and *Seber et al.* (2001) (Figure 4.3). Model domain is discretized into small 3D rectangular prisms of four layers with different densities: ice (917 kg/cm^3), ocean water (1030 kg/cm^3), rock (2670 kg/cm^3) and sediment (2014 kg/cm^3). Here, we have no further information or knowledge of the proper density for sediment, so we use 40% of porosity for the rock filled with sea water (*Muto et al.*, 2013).

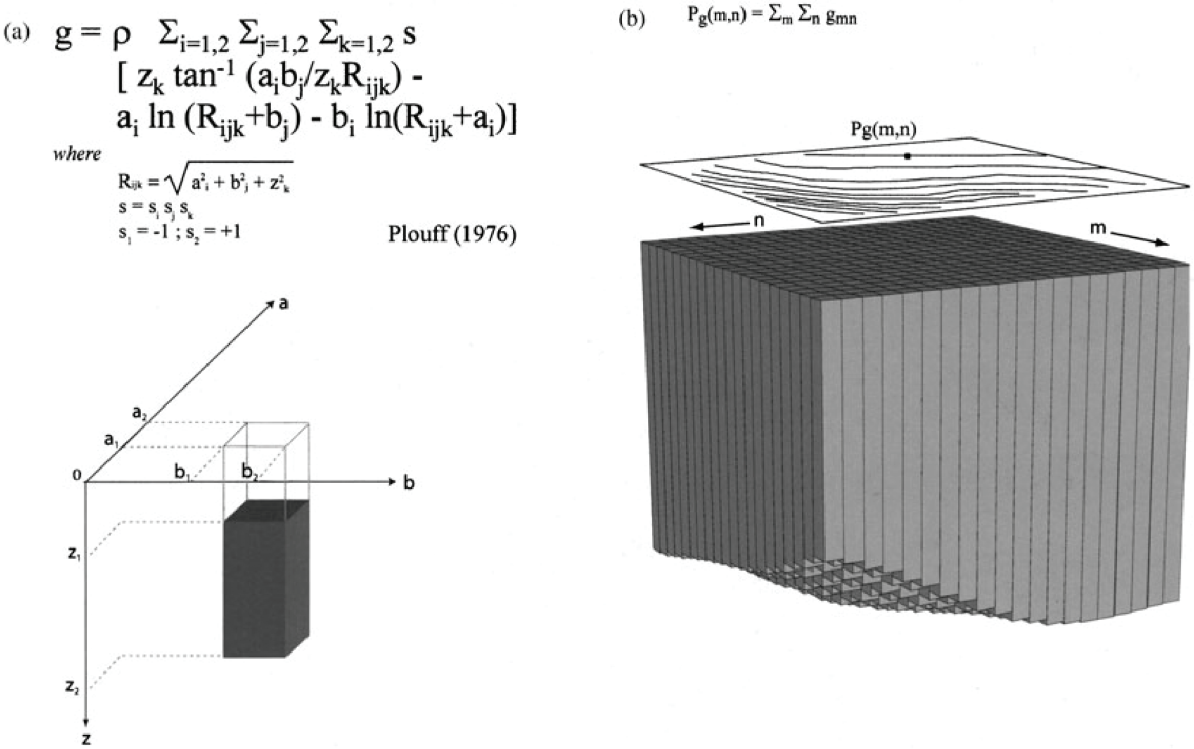

Figure 4.3: Schematic diagrams from *Seber et al.* (2001).

The inversion part in this method using very fast simulated annealing (VFSA), which *Roy et al.* (2005) and *Filina et al.* (2008) used to model the water depth and sediment distribution in Lake Vostok. We solve the inverse problem by minimizing the misfit function by *Roy et al.* (2005):

$$E = \frac{2\sum(|g_{obs} - g_{cal}|)}{\sum(|g_{obs} - g_{cal}| + \sum|g_{obs} + g_{cal}|)} \tag{4.1}$$

where g is the free-air anomaly with subscripts *obs* and *cal* represented observed and calculated gravity anomaly respectively.

The shape of the body is established by computing the thickness of rectangular prisms of equal width. Searching for a plane that minimize the root mean square difference between the observed and calculated gravity anomalies. DC-shift in the model is calculated where measured gravity data overlapped with exposed rock in this area (Figure 4.4c).

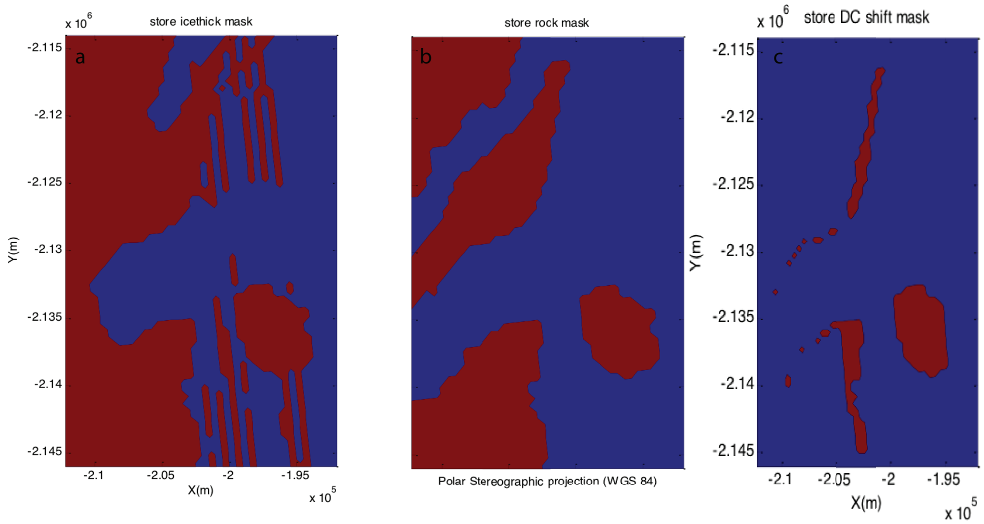

Figure 4.4: (a) Model ice thickness mask, (b) model rock mask, blue block values vary in inversion, red block values fixed in inversion. (c) area to calculate DC-shift (red)

Results The bed rises near the front of the glacier, which makes the glacier more robust to change. Accumulation of sediment has a significant influence in the fjord, but not so much underneath the glacier (Figure 4.7). At sea, in front of the area of river discharge, there is a large pile of sediment, which exhibit a gravity anomaly associated to a layer of sediment of higher density than water about 200-300 m thick.

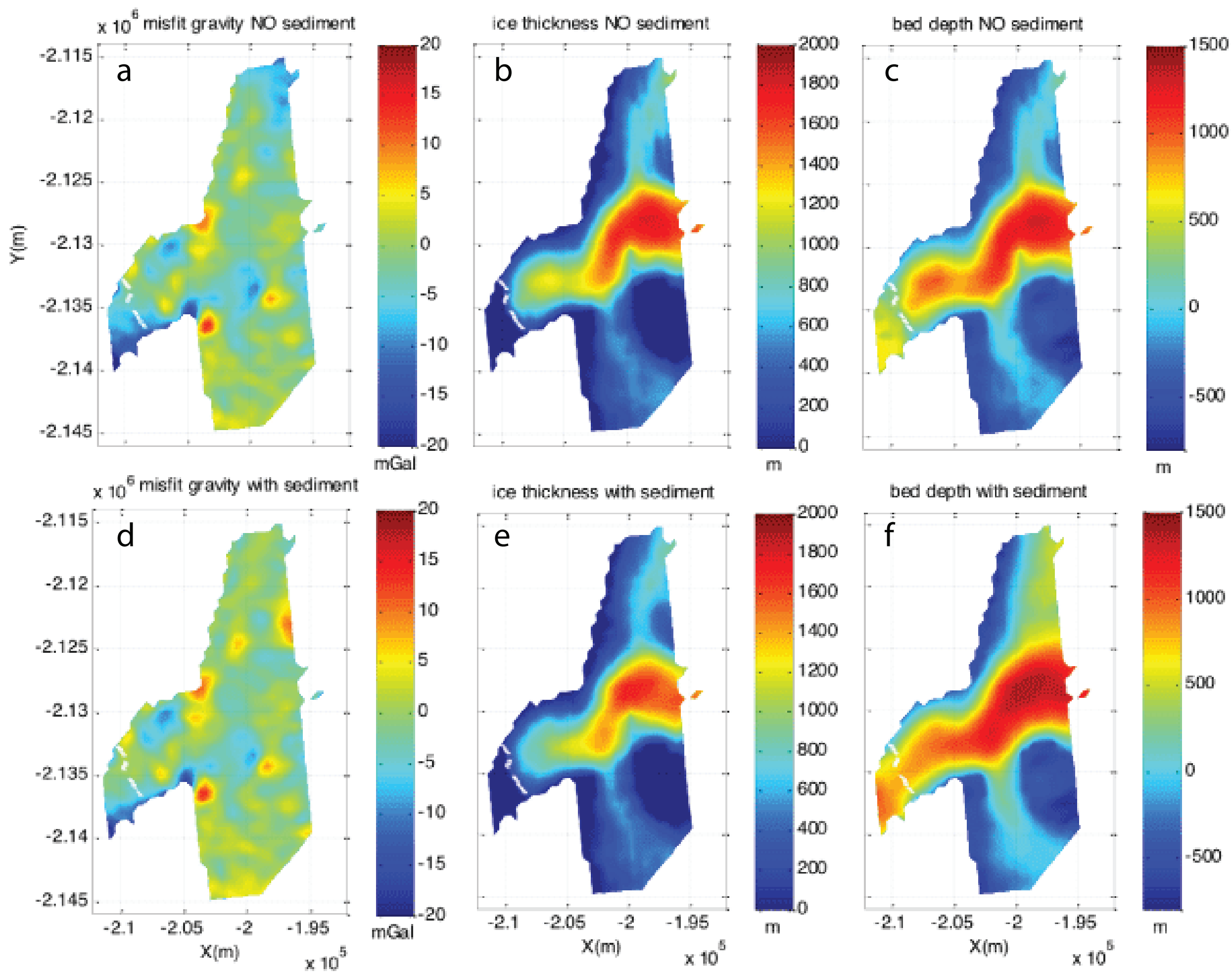

Figure 4.5: Inversion results comparison between model without (a-c) and with (d-f) sediment layer. (a) (d) misfit between calculated and observed gravity, (b) (e) ice thickness in meters after inversion without and with sediment layer separately, (c) (f) bed elevation results in meters without and with sediment layer separately. White line indicates ice front in 2012.

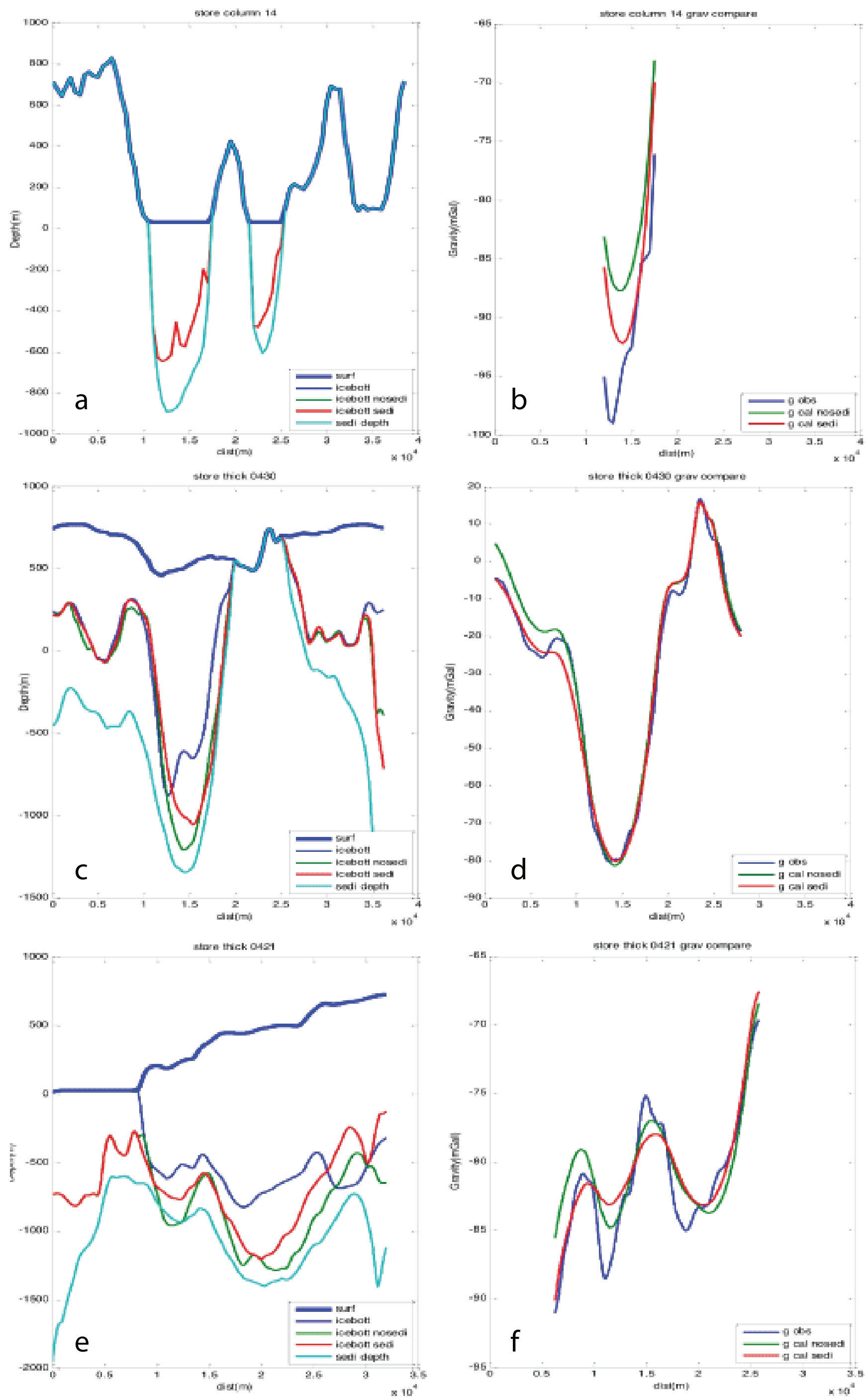

Figure 4.6: Inversion results along three profiles in Figure 4.1b. For each row, left panel is the comparison for bed elevation, and dark blue lines are surface and ice bottom elevation from model initial set-up; dark green line is ice bottom elevation from model without sediment layer; red line is ice bottom elevation from model with sediment layer; light green line represents bed elevation with sediment layer thickness. Right panel is comparison between observed and calculated gravity, and dark blue line is observed gravity; dark green line is calculated gravity from model without sediment layer; red line represents calculated gravity from model with sediment layer. (a) (b) column 14, (c) (d) Thick_0430, (e) (f) Thick_0421.

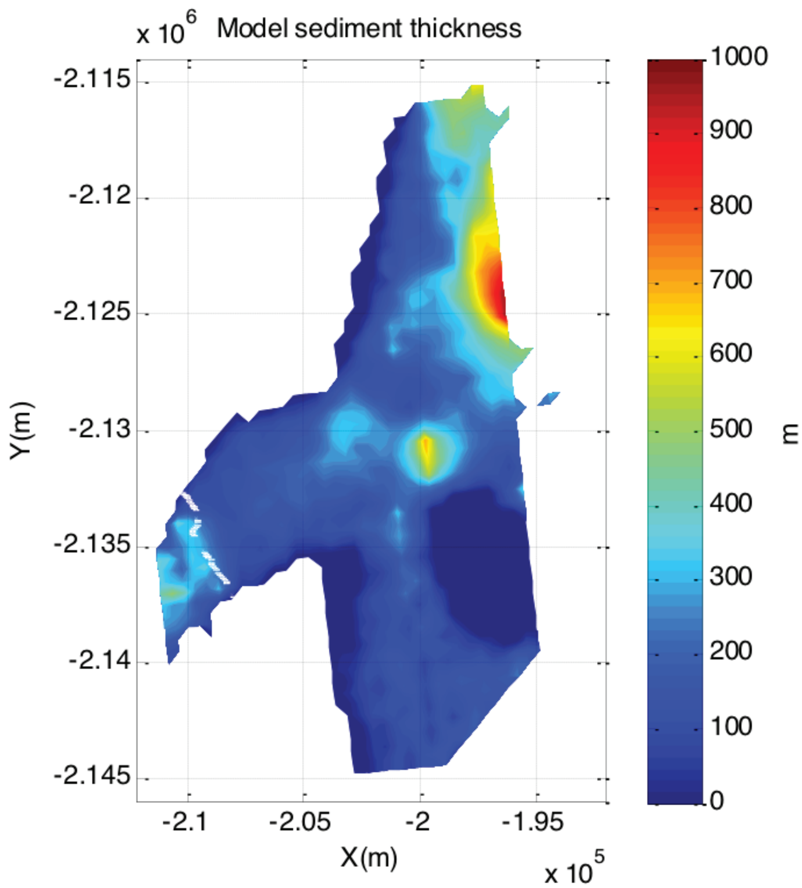

Figure 4.7: Inversion result of sediment layer thickness underneath Store Glacier in meters. Color coded from dark blue (0 m) to green (500 m) then to dark red (1000 m). White line indicates ice front in 2012.

Gravity Inversion from GM-SYS 3D Modeling

Methods To analyze the gravity data, we employ the Geosoft GM-SYS 3D software, which implements *Parker* (1973)'s method. The inversion domain is modeled as three layers: 1) a solid ice layer with a density of 0.917 g/cm^3; 2) a sea water layer with a density of 1.028 g/cm^3; and 3) a rock/sediment substrate layer with a uniform density of 2.67 g/cm^3. Selection of a density for rock is discussed above. Ice surface elevation is from the GBMF laser altimeter. The model domain extends to the limit of the GBMF survey. Beyond the survey domain, we use the initial bed model to calculate the gravity field using a forward model based on GM-

SYS 3D (Figure 4.8).

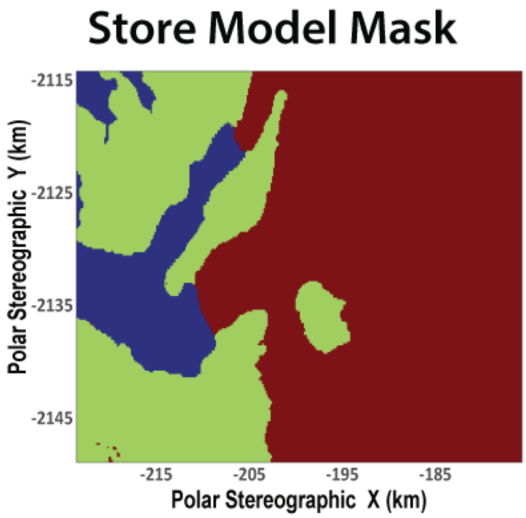

Figure 4.8: Mask domain for Store Glacier, blue block is ocean, light green is rock, red is grounded ice area.

Results 1. This analysis shows that major uncertainties exist in the mapping of the bed elevation of the glaciers in Greenland and in the sea floor bathymetry. On Store Glacier, we detect a sill at the current ice front that is probably responsible for its exceptional stability versus neighboring glaciers since 1958. The glacier is grounded hundreds of meters deeper than indicted in *Bamber et al.* (2013) and the fjord is also deep enough to enable widespread access of subsurface warm, salty waters from the North Atlantic than indicated in IBCAO (*Jakobsson et al.*, 2012).

2. These results call in question model simulation of weak influence of the ocean on glacier evolution as well as projections of glacier evolution in a warmer climate in general until a similar quality mapping is performed on other Greenland glaciers.

3. High resolution airborne gravity is instrumental in filling gaps between MBES data and MC calculations, and may in some places difficult to probe provide a very important alternative to the reconstruction of ice thickness. Such data should however be acquired on a slower moving platform than OIB. (GBMF = 50 knots; OIB = 400 knots).

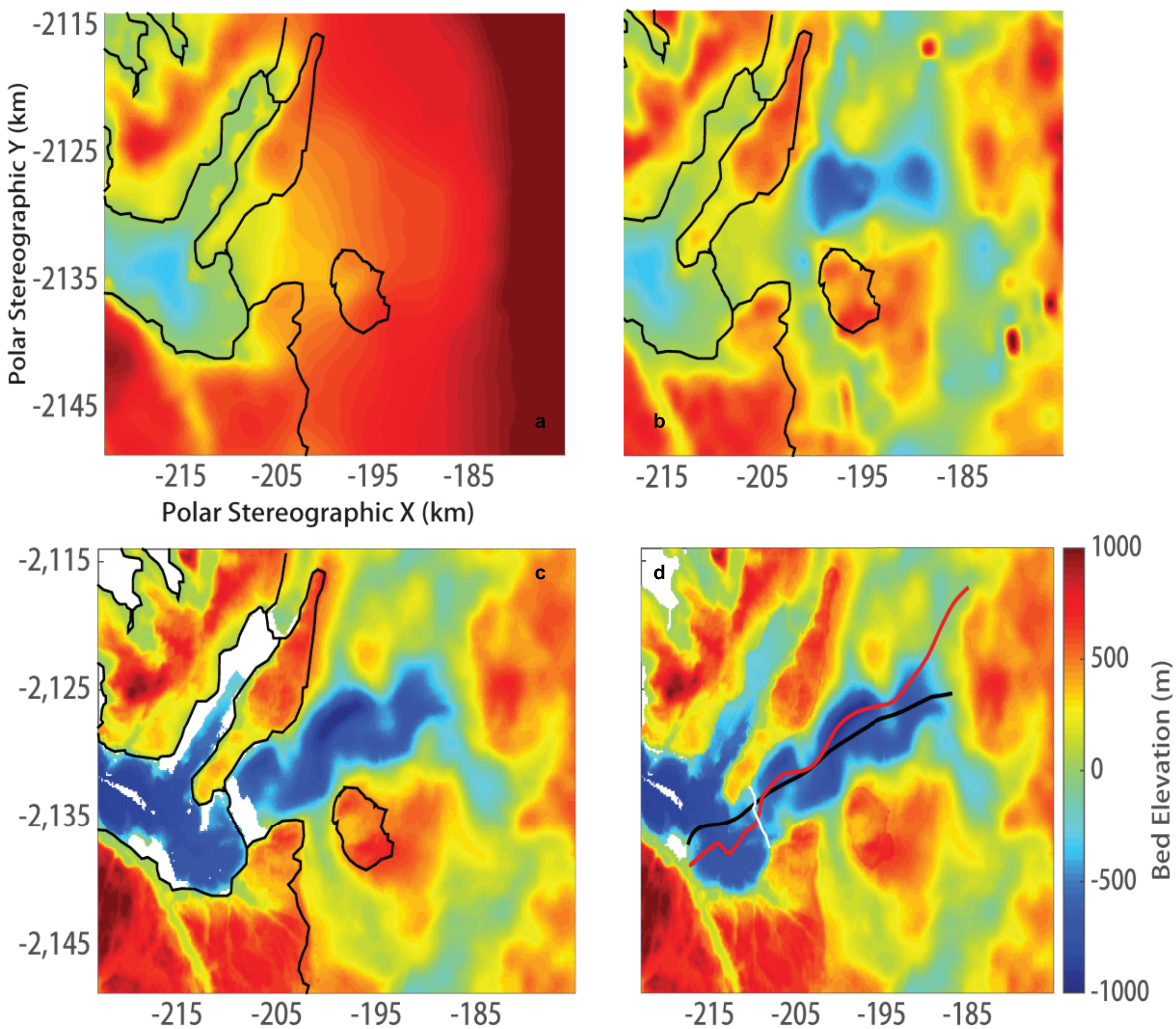

Figure 4.9: Store Glacier bed elevation results. (a) Bed elevation from IBCAO3 (*Jakobsson et al.*, 2012), (b) Bed elevation on and sea from *Bamber et al.* (2013), (c) MC bed elevation (*Morlighem et al.*, 2014) and MBES bed elevation, and (d) MC bed elevation, MBES and airborne gravity derived bed elevation, white line is the ice front in 2012; black line is CReSIS on 20080722; red line is flow line of Store Glacier. Black lines represent the boundaries of rocks and ocean.

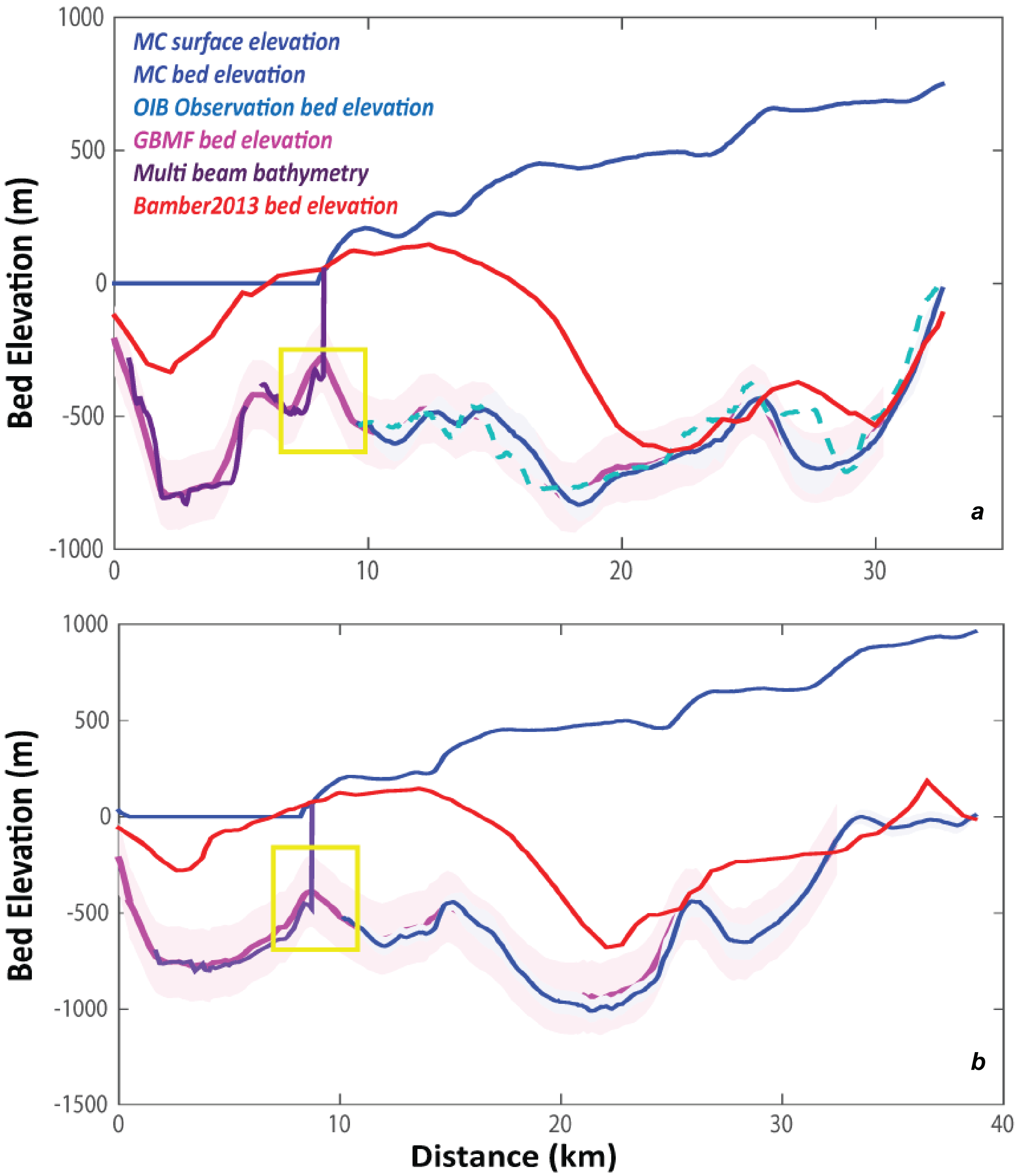

Figure 4.10: Bed elevation results comparison between different solutions along two lines in Figure 4.9d. (a) CReSIS line on 20080622, (b) Store Glacier flow line, MC (dark blue), OIB (light blue), GBMF (magenta), MBES (purple) and *Bamber et al.* (2013) (red).

4.1.3 Discussion

Here, we employ high-resolution (250 m spacing) , high-precision (0.5 mGal) gravity data combined with other data to reconstruct the bed topography of Store Glacier, West Greenland from its terminal valley, across the grounding line, into the glacier fjord with two types of 3D models. The gravity inversion is constrained by a reconstruction of ice thickness on land combining sparse radar profiles and ice motion vectors from satellite imaging radar, and at sea with multi-beam echo sounding right to the foot of this glacier. The inversion result indicates the presence of a 400 m sill at the current position of the glacier front. When sediment thickness is also included in the inversion, we identify regions of sediment accumulation downstream of channels of subglacial water discharge and less than 200 m elsewhere.

Overall the presence of a bed high at the current front location explains the exceptional stability of Store Glacier in the last 50 years despite warming air temperature and exposure to warm Atlantic water.

4.2 3D modeling of Jakobshavn Isbræ, West Greenland

4.2.1 Introduction

The contribution to sea level rise from the Greenland Ice Sheet has increased significantly in the past decades due to the accelerated flow of its glaciers and the enhanced melting of its snow and ice surface (*Rignot et al.*, 2011a, e.g.). Jakobshavn Isbræ (JI), in West Greenland, is the largest and most active outlet glacier. It drains 6.5% of the ice-sheet area (*Echelmeyer et al.*, 1991). Repeated laser-altimeter surveys by NASA's Airborne Topographic Mapper (ATM) showed that the glacier experienced a slight thickening between 1991 to 1997 of 10 cm/yr (*Thomas et al.*, 1998) while many other glaciers were thinning. After 1997, the glacier started to thin (*Thomas et al.*, 2003) and accelerate (*Joughin et al.*, 2004; *Luckman and Murray*, 2005). The glacier floating ice tongue collapsed in 2002-2003 (*Weidick et al.*, 2004) after experiencing thinning rates of up to 80 m/yr (*Thomas et al.*, 2003). The ice shelf removal reduced the back-stress on the glacier, causing its ice speed to triple (*Joughin et al.*, 2008). As the glacier retreated, the frontal regions thinned up to 15 m/yr (*Thomas et al.*, 2009).

This drastic evolution following decades of slow retreat since the little ice age has been attributed to the intrusion of warmer-than-usual, salty, subsurface (below 400 m depth) Atlantic waters (AW) into Ilulissat fjord in the mid 1990s (*Holland et al.*, 2008). The higher heat content of the fjord waters fueled higher rates of ice shelf melt causing it to collapse. *Motyka et al.* (2011) estimated from mass conservation that the ice shelf melted at 228$\pm$49 m/yr in the 1980s. The melt rate must have therefore increased by 35% in the late 1990s to explain the observed 80 m/yr thinning. As a result of the ice shelf collapse and glacier acceleration, JI contributed a 1-mm global sea level rise from 2000 to 2011 (*Howat et al.*, 2011).

To interpret the glacier evolution and reduce uncertainties in projections of its evolution, it is essential to know the glacier thickness, bed elevation below sea level (bsl), and fjord bathymetry. The slope in bed topography exerts a major control on the rate of grounding line retreat (*Schoof*, 2007). The retreat is expected to be rapid along retrograde portions of the bed, i.e. where the bed elevation slopes in the inland direction, because a higher ice thickness entrains higher spreading rates. Conversely, bumps in bed topography will slow down the retreat due to a reduction in spreading rate. This instability is referred to as the marine ice sheet instability or tide-water glacier cycle (*Post et al.*, 2011). In the fjord, bathymetry controls the advection of warm, salty AW toward the grounding line. Deep portions of the fjord facilitate the intrusion of subsurface AW whereas shallow parts (< 300 m) restrict its access to the glacier (*Holland et al.*, 2008).

To this day, the fjord bathymetry and glacier bed topography of the lower portion of JI have remained poorly known, at least not sufficiently well to provide reliable information for ice sheet numerical models. Standard vessels cannot penetrate the fjord to measure its depth due to the permanent presence of icebergs, brash ice, and ice mélange caused by a 350 m deep sill at the mouth of the fjord which blocks the exit of icebergs. On land, the sounding of bed topography in the lower reaches of the glacier using the Multichannel Coherent Radar Depth Sounder (MCoRDS) is rendered difficult by the thick ice (2 km), the presence of highly absorptive and temperate ice near the bottom, combined with high surface clutter caused by a broken up ice surface (*Leuschen et al.*, 2010, updated 2017). Seismic profiles were successfully collected upstream of the terminus by *Clarke and Echelmeyer* (1996). Together with quality radar data upstream, these observations revealed the presence of a deep trough beneath JI, more than 1 km bsl, extending far inland (*Plummer et al.*, 2008, e.g.). Near the ice front, few reliable bed echoes are available. Radar sounders do not provide a comprehensive description of the bed topography, hence leaving considerable uncertainty about the depth of JI close to the ocean margin.

4.2.2 Data and Methods

To analyze the gravity data, we employ the Geosoft GM-SYS 3D software, which implements *Parker* (1973)'s method. The inversion domain is modeled as three layers: 1) a solid ice layer with a density of 0.917 g/cm^3; 2) a sea water layer with a density of 1.028 g/cm^3; and 3) a rock/sediment substrate layer with a uniform density of 2.72 g/cm^3. Selection of a density for rock is discussed later on. Ice surface elevation is from the GBMF laser altimeter. The model domain extends to the limit of the GBMF survey. Beyond the survey domain, we use the initial bed model to calculate the gravity field using a forward model based on GM-SYS 3D (Figure 4.11).

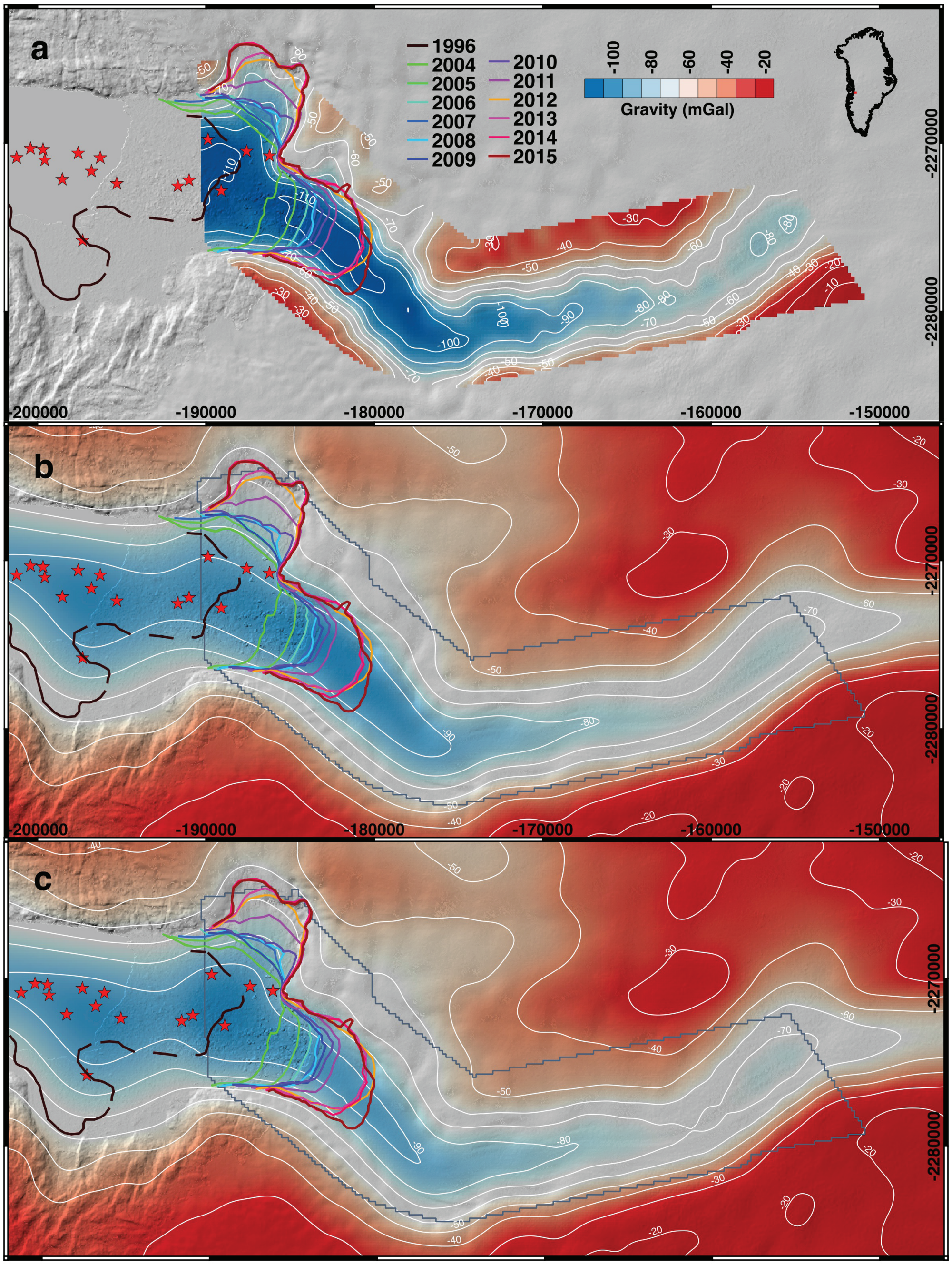

Figure 4.11: (a) Airborne, high-resolution, free-air gravity anomalies measured in 2012 for the GBMF survey over Jakobshavn Isbræ, West Greenland with a color scale in mGal(1 mGal=10^{-5} m^2/s), (b) forward model calculated gravity and (c) forward model calculated gravity over Jakobshavn Isbræ, West Greenland, knitted together with observed gravity after upward continuation to 1,220 m overlaid on a shaded relief digital elevation model of Greenland (*Howat et al.*, 2014). Contour level is every 10 mGal in white. Grounding line positions are color coded from brown (1996 from ERS-1/2) to green, blue, and red (2004 to 2015 from Landsat image). Red stars are positions of measured fjord bathymetry. The limit of the survey domain is a thin, dark blue outline in (b) and (c).

The initial bed model is the interpolated bathymetry for the fjord and the MC result on land. We match the observed gravity and forward modeled gravity at the boundary by estimating the DC shift to apply on the data in the upper part of the survey domain where the MC result is most reliable because quality ice thickness data exist. In the 3D model, we use constraints grids to constrain or restrict some of the inversion options. A constraints grid is a grid that matches the index grid for the model and constraints values between 0 and 1. Where the value of a grid node in the constraints grid is set to 0, the corresponding location in the grid being inverted will remain unchanged. Where the value of a grid node in the constraints grid is set to 1, the corresponding location in the grid being inverted is totally unconstrained. If the value in the constraints grid is greater than 0 and less than 1, it acts as a weighting factor to slow down the amount of movement during inversion. In our model, we allow a 1.5-km wide transition at the ocean boundary and at the boundary with the modeled gravity. Within the transition boundary, the inversion is modulated by a factor varying linearly between 0 (no gravity inversion) to 1 (full gravity inversion) as a function of distance to the gravity survey. No data inversion is performed outside the domain (inversion factor is 0). During the inversion, the unknown bed elevation is modified iteratively until we obtain the best match between modeled and observed gravity. The iteration stops when the calculated gravity does not vary by more than 0.1 mGal.

To define an optimal average density for the glacier bed. First, we check the geological information in this area (*Pedersen et al.*, 2013) and find that the rock type is orthogneiss, mainly granodioritic to tonalitic with density range from 2.6 to 3.0 g/cm^3. So we calculate the rate of convergence of the solution in terms of the misfit between modeled and initial gravity fields for densities varying from 2.6 to 3.0 g/cm^3 with steps of 0.02 g/cm^3. We find a minimum at a density of 2.72 g/cm^3 (Figure 4.12). A value of 2.72 g/cm^3 is consistent with the presence of orthogneiss, mainly granodioritic to tonalitic, in the area (*Pedersen et al.*, 2013).

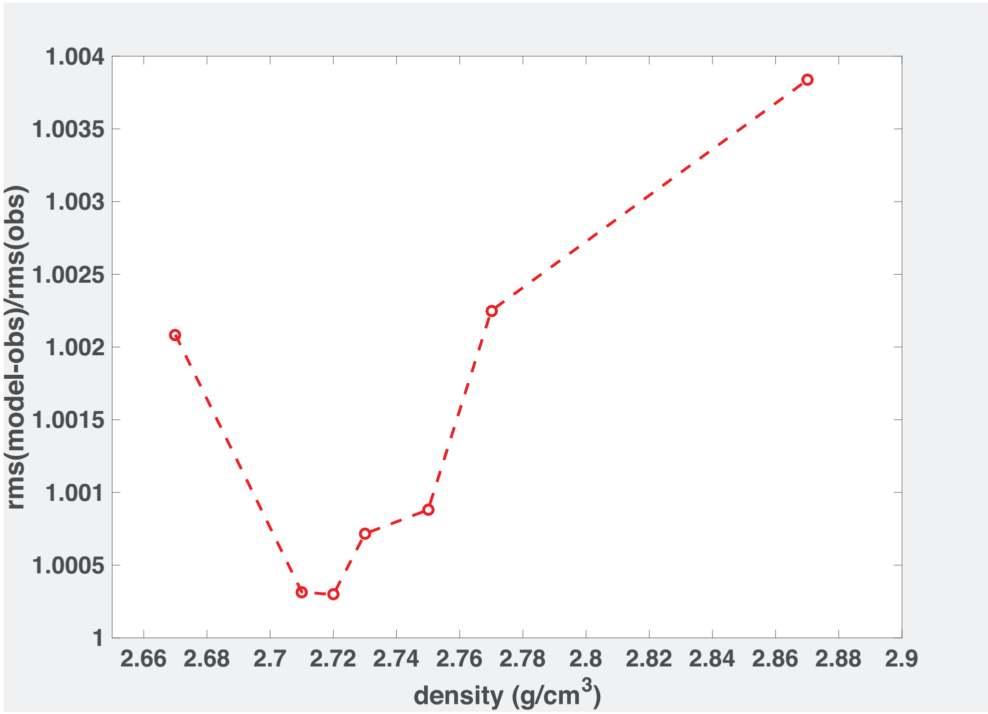

Figure 4.12: Optimization of the bedrock density beneath Jakobshavn Isbræ, West Greenland, obtained by comparing the r.m.s. of the modeled gravity solution versus the observed gravity divided by the r.m.s of the observed gravity for density values varying from 2.6 to 3.0 g/cm^3. The results reveal the existence of a minimum at a density of 2.72 g/cm^3. The density value of 2.72 g/cm^3 is in excellent agreement with the density of Orthogneiss (mainly granodioritic to tonalitic) present in this area according to the geologic maps of the Geological Survey of Denmark and Greenland (GEUS).

We use the gravity misfit, i.e. modeled gravity minus observed gravity, to quantify the uncertainty of the inversion (Figure 4.13).

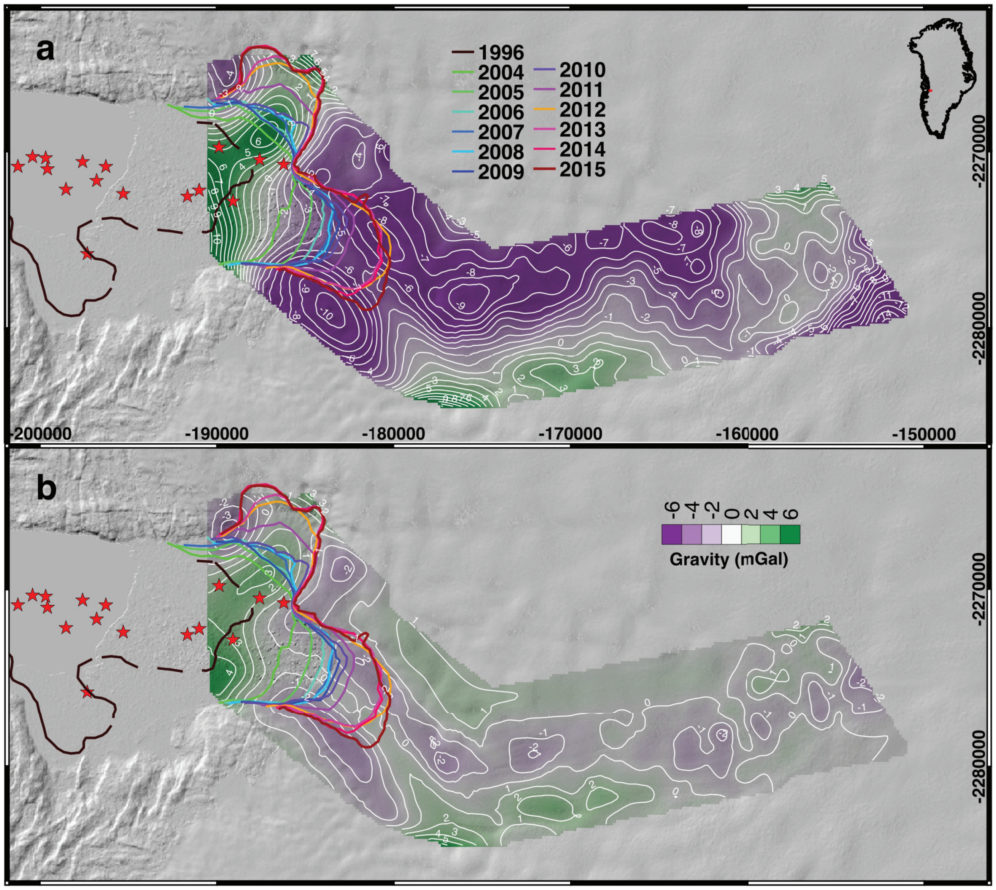

Figure 4.13: (a) Forward model gravity misfit (model minus observation) over Jakobshavn Isbræ, West Greenland, after upward continuation to 1,220 m and (b) inversion model gravity misfit in milligal (mGal) overlaid on a shaded relief digital elevation model of Greenland (*Howat et al.*, 2014). Contour level is every 1 mGal for the misfit. Inset on top right shows the location of the survey area in Greenland. Grounding line positions are color coded from brown (1996 from ERS-1/2) to green, blue, and red (2004 to 2015 from Landsat image). Red stars show the location of bathymetry measurements in Ilulissat fjord.

The inversion significantly reduces the gravity misfit from the initial bed, as expected. To translate the misfit (in mGal) into an error in bed elevation, we calculate the gravity anomaly using GM-SYS 3D obtained by shifting the bed result by +100 m and compare the results with the original gravity field. We find an average shift of 5 mGal in gravity per 100 m of ice in the trough. We use this product to generate a point-per-point conversion of the gravity misfit into an uncertainty in bed elevation (Figure 4.14). Given that the gravity misfit ranges from -3 to +3 mGal, the nominal precision of our bed mapping is about 60 m.

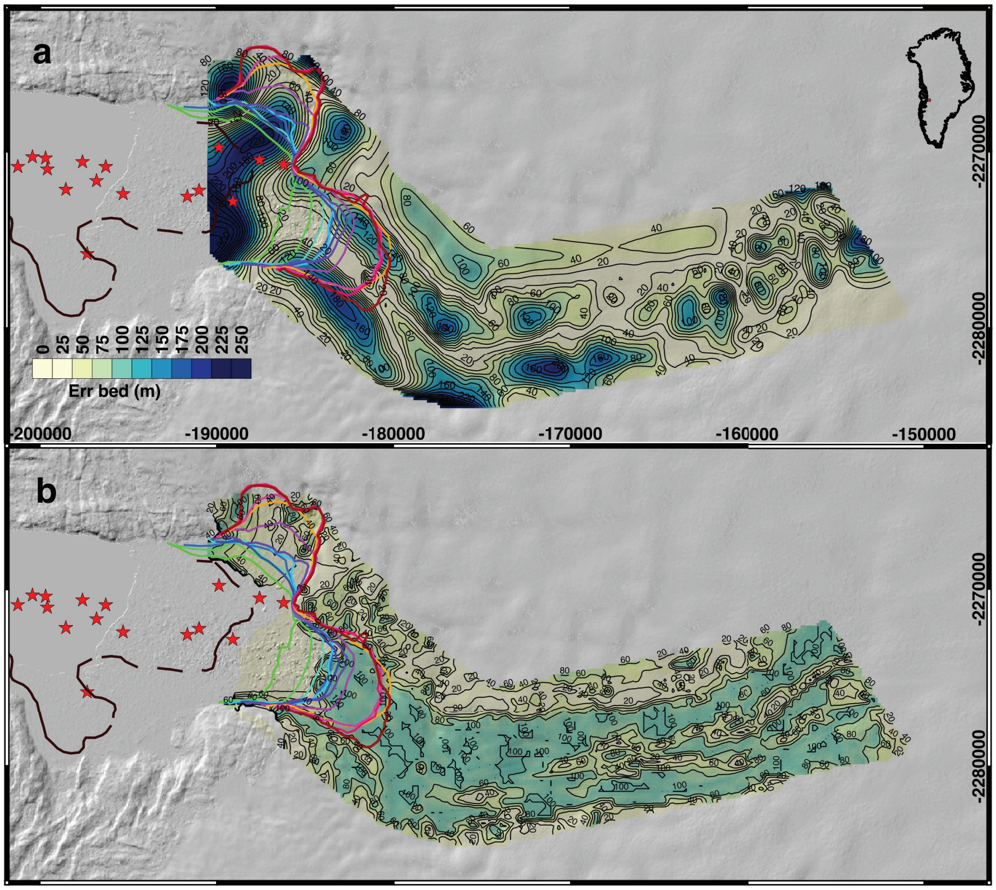

Figure 4.14: Bed error map (a) calculated from gravity inversion model gravity misfit with the bed result by +100 m shifting, and (b) bed error map from MC in meter (m) overlaid on a shaded relief digital elevation model of Greenland (*Howat et al.*, 2014). Contour level is every 20 m in black. Inset on top right shows the location of the survey area in Greenland. Grounding line positions are color coded from brown (1996 from ERS-1/2) to green, blue, and red (2004 to 2015 from Landsat image). Red stars show the location of bathymetry measurements in Ilulissat fjord.

Existing radar-derived thickness data from MCoRDS were used to produce an updated MC result for the bed, ice thickness, and error (Figure 4.14). The MC result is gridded at 150-m spacing, with a spatial resolution of 150m. The MC map is better in terms of resolution and accuracy than *Bamber et al.* (2013)'s 1-km spacing map, or B2013, which uses kriging on land and the International Bathymetric Chart of the Arctic Ocean (IBCAO) v3 in the fjord (*Jakobsson et al.*, 2012). We also compare the GBMF result with the bed map of *Joughin et al.* (2014), generated by CReSIS in 2009 and which we refer to as C2009.

We map the grounding line of JI using ERS-1/2 interferometric SAR data from year 1996, ERS-1 orbits 22386 and 22887 and ERS-2 orbits 2713 and 3214, frames 1890, following (*Rignot et al.*, 2011b). While interferometric fringes are not visible across the entire grounding line, especially the northern tributary, the results capture the 1996 position over the deepest part of the glacier and on its near-stagnant ice shelf (Figure 4.16). We complement this information with the mapping of ice rumples by *Csatho et al.* (2008) to get a near-continuous mapping (Figure 4.15).

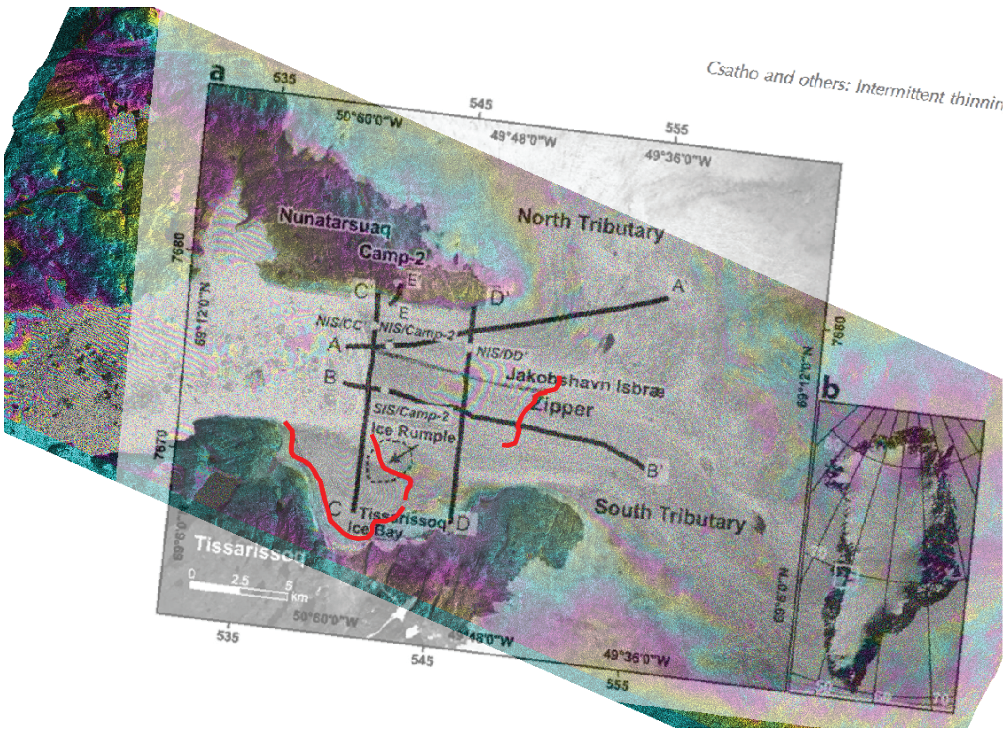

Figure 4.15: Differential SAR interferograms (DSIs) of Jakobshavn Isbræ, West Greenland, obtained from Earth Remote Sensing satellite 1 and 2 (ERS-1/2) data collected in winter 1996 overlaid on the figure 1 from *Csatho et al.* (2008). Grounding line position in 1996 is red.

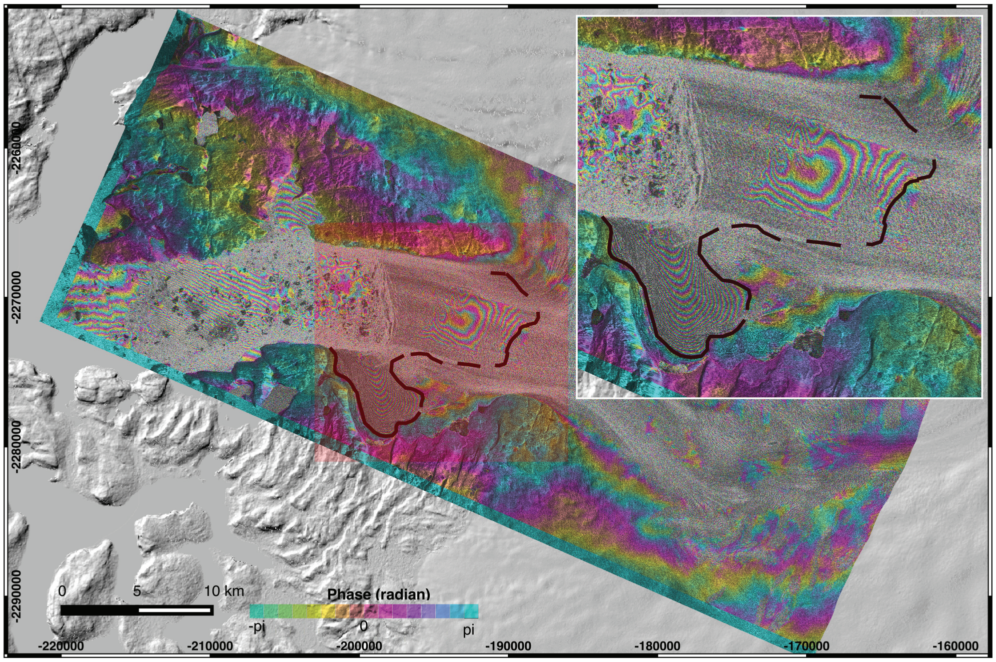

Figure 4.16: Differential SAR interferograms (DSIs) of Jakobshavn Isbræ, West Greenland, obtained from Earth Remote Sensing satellite 1 and 2 (ERS-1/2) data collected in winter 1996 overlaid on the GIMP shaded relief map of Greenland (*Howat et al.*, 2014). Grounding line position in 1996 is brown. Each fringe color coded from blue to yellow, purple, and blue again is a 360 cycle in interferometric phase. Note, some portion of the grounding line mapping is based on the mapping of ice rumples by (*Csatho et al.*, 2008).

Following the ice shelf collapse in 2002-2003, *Rosenau et al.* (2013) showed that the glacier developed a floating section only about 100 m long along the ice front, i.e. the grounding line has remained within 100 m of the calving front after 2003. Combining the 1996 interferometric data with ice-front positions recorded from Landsat data in late summer conditions (late August to early September) we obtain a 20-year proxy record for the grounding line retreat of JI (Figure 4.17, 4.18).

4.2.3 Results

Our model does not use a layer of sediment. We do a simple Bouguer slab calculation, which we add a 100-m sediment layer with density 2.2 g/cm^3 into the model. The result shows that bed elevation overestimate by 30 m. To explain the gravity anomaly measured by OIB over the JI trough, one would need a 1,500-m thick layer of sediments to match existing ice thickness measurements. We conclude that the OIB data cannot be used to detect the depth of the JI trough. The only gravity data that are sensitive enough to detect the deepest bed are from the GBMF survey.

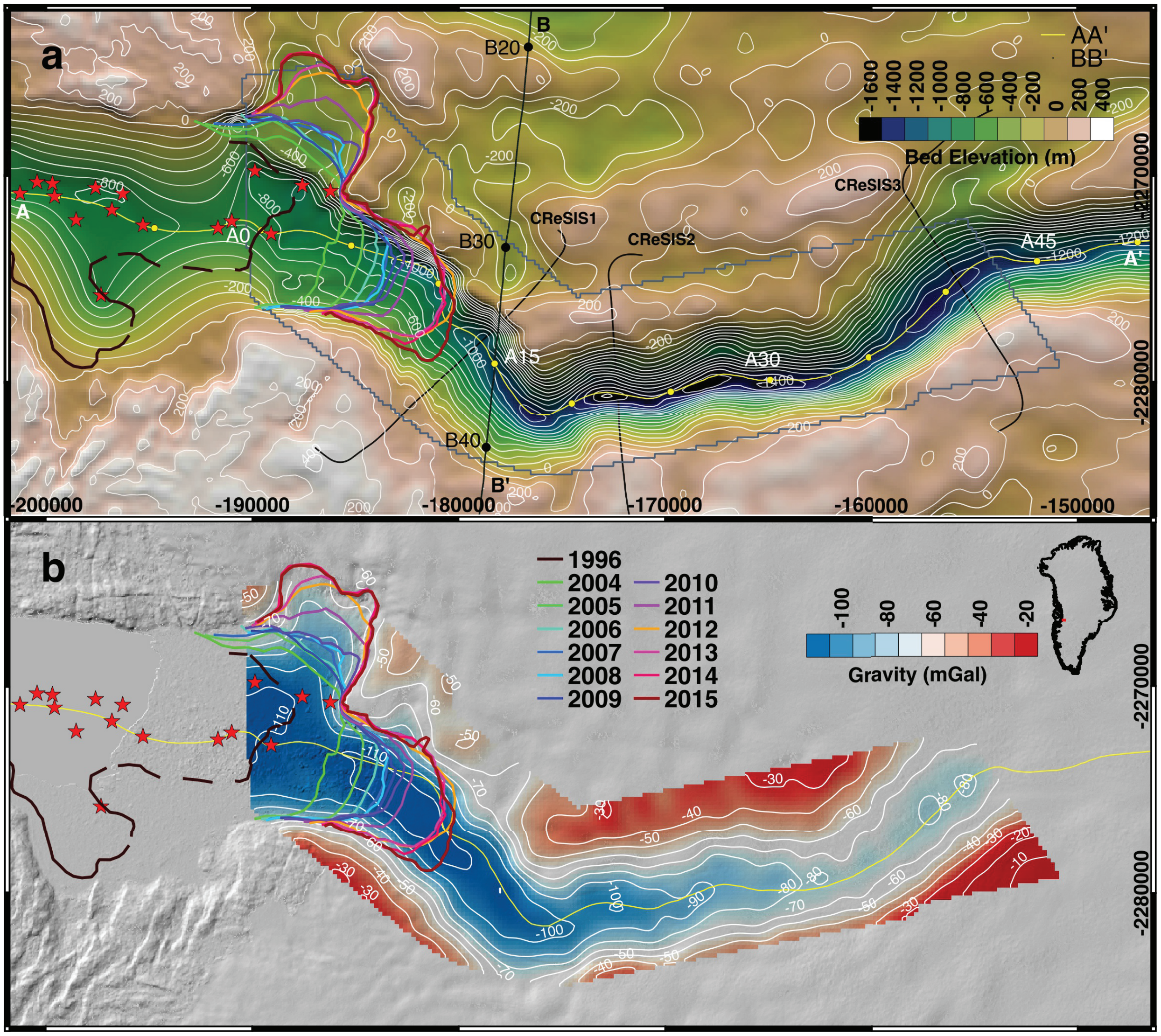

Figure 4.17: (a) Bed elevation above mean sea level of Jakobshavn Isbræ (JI), West Greenland and fjord bathymetry reconstructed from a 3D inversion of the GBMF gravity data, color coded from white to brown (400 m to 0 m above sea level) to green, blue and dark blue (200 to 1,600 m below sea level) with 100-m contours in white. Profile AA′ with yellow dots every 5 km is shown in Figure 4.18, profile BB′ in Figure 2.4, 2.5, profiles CReSIS1-3 in Figure 4.19. The limit of the survey domain is a thin, dark blue outline. Grounding line positions are color coded from brown (1996 from ERS-1/2) to green, blue, and red (2004 to 2015 from Landsat). Discrete depth soundings in the fjord are red stars. Background is a shaded relief digital elevation model of Greenland (*Howat et al.*, 2014). Projection is polar stereographic north at 150 m spacing. (b) Airborne, high-resolution, free-air gravity anomalies from the year 2012 GBMF survey with a color scale in mGal (1 mGal=10^{-5} m^2/s) and 10-mGal contours in white. Survey lines are thin black lines. Inset on top right shows glacier location in Greenland.

The observed gravity anomalies vary from -20 mGal to -120 mGal, with peak values along the trough and near the grounding zone (Figure 4.17b). Bed elevation is well correlated with the gravity anomaly (Figure 4.17a), except in the last 15 km where the bed map is asymmetric: the bed is steeper and deeper on the north side, and smoother and shallower on the south side. The northern branch of the glacier terminates abruptly in the ocean. The asymmetry is present in seismic profile S8 of *Clarke and Echelmeyer* (1996) approximately located at km 16. Upstream of km 20, the bed is symmetric, with a bed depth of 1,600 m at km 22 from the 1996 grounding line (Figure 4.18). Bumps and hollows in inferred bed elevation greater than 60 m are above the noise level.

Rosenau et al. (2013) reported a 3.5$\pm$0.2 km grounding line retreat for 2004-2010, or 0.6 km/yr, similar to the value from *Joughin et al.* (2012) for 2006-2009. Here, we estimate 0.62 km/yr for the entire period 1996 to 2016, with a total grounding line retreat of 12.5 km at the glacier center. During that time period, the ice shelf front retreated by 18 km.

The inversion yields a smooth transition in bed topography between the GBMF data and the MC result but at a lower spatial resolution (Figure 4.18). Following the line of deepest bed, we find that the bed depth drops from 700 m at the center of the grounding line in 1996 to 1,100 m bsl at the 2015 grounding line. Farther upstream, the bed depth drops to 1,600 m at km 22, then slowly rises to 1,200 m over the next 40 km. From km 0 to 27, the bed is essentially retrograde, consistent with earlier studies but several 100 m deeper (*Joughin et al.*, 2012; *Gogineni et al.*, 2014). The grounding line retreated rapidly from 2011 to 2012, before retreating more slowly as the glacier encountered a shallower bed.

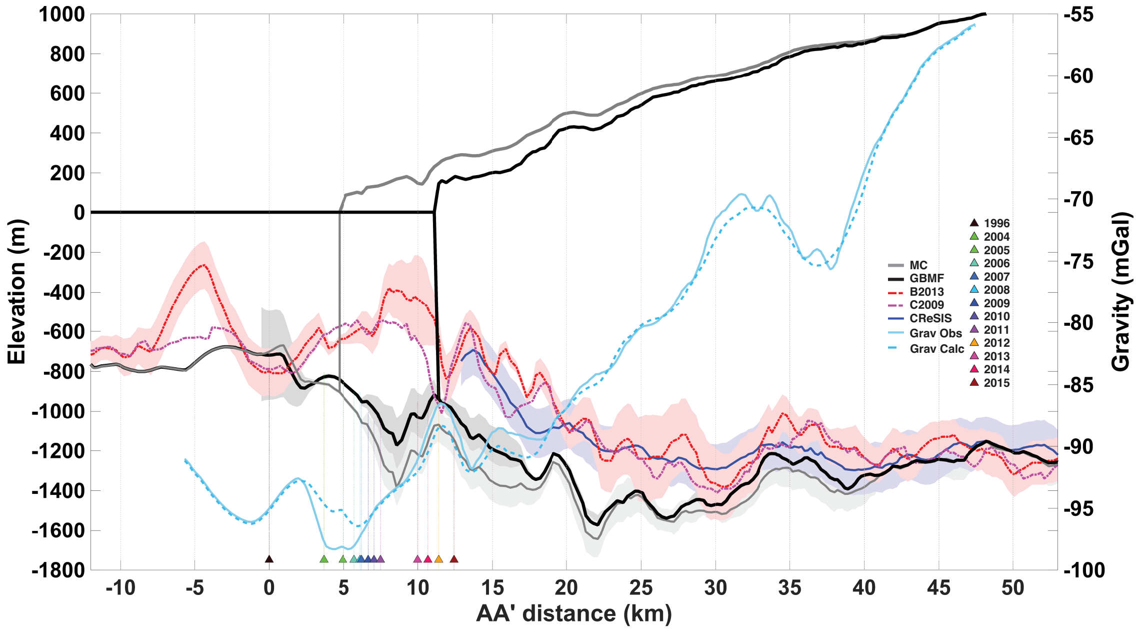

Figure 4.18: Profile AA′ along the deepest bed of Jakobshavn Isbræ, West Greenland showing the surface and bed elevations from the MC reconstruction (gray), the GBMF data in this study (black), *Bamber et al.* (2013) (dotted red), *Joughin et al.* (2014) (dotted purple) and CReSIS (dark blue) with corresponding error bars in shaded color ($\pm 1\sigma$). The surface elevation is from year 2007-2008 (MC, B2013, C2009) and 2012 (GBMF). Red stars denote bathymetry data in the fjord. Colored triangles denote the positions of the glacier grounding lines at different epochs with the same color table as in Figure 4.17. Origin of distance is the 1996 grounding line position. Superimposed on that plot with a secondary vertical axis on the left hand side is a comparison of the observed gravity anomaly (continuous blue) versus the calculated (dotted blue) gravity anomaly in mGal along profile AA′.

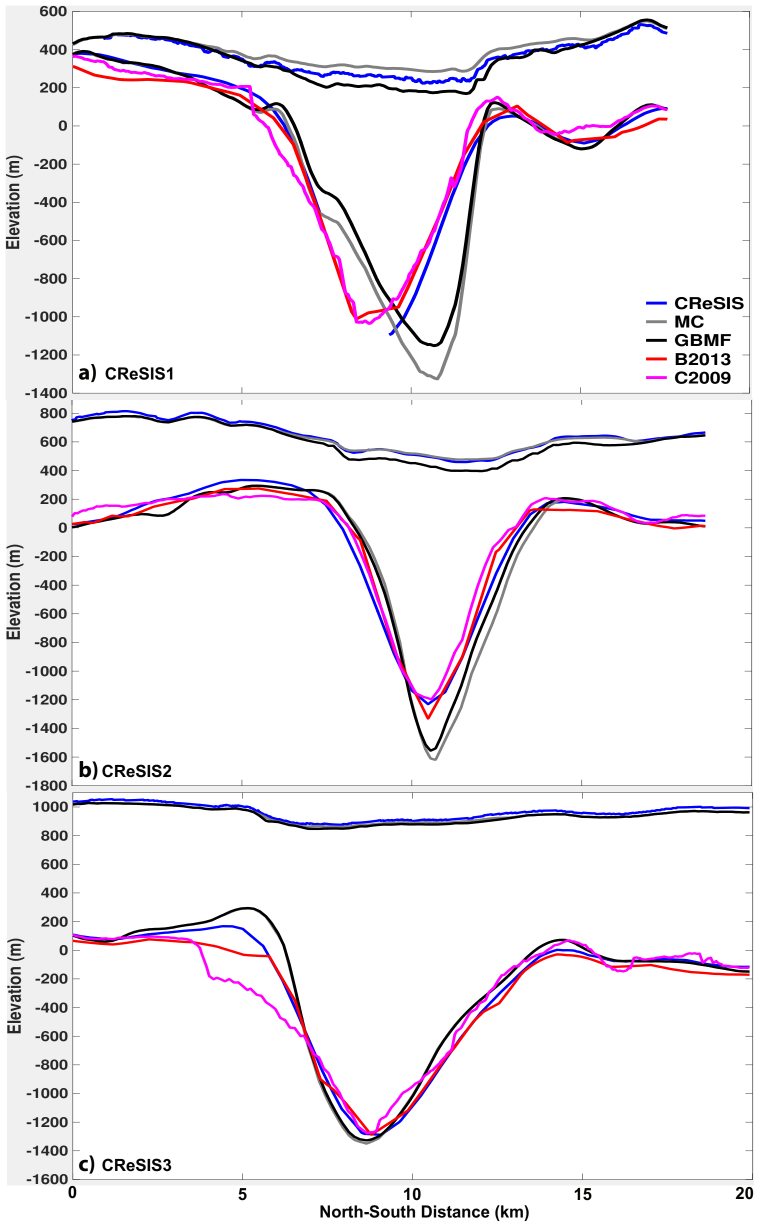

Figure 4.19: Comparison of the bed elevation Jakobshavn Isbræ, West Greenland from the MC reconstruction (gray), the GBMF gravity survey (black), *Bamber et al.* (2013) (red) and *Joughin et al.* (2014) (purple) along profiles (a) CReSIS1, (b) CReSIS2 and (c) CReSIS3 in Figure 4.17, at respectively low, medium and high elevation along the trough, along with surface elevation from CReSIS (blue) in 2009, GBMF in 2012 (black) and MC/B2013/C2009 in 2007-2008 (gray). Direction is north to south from left to right.

A comparison of GBMF with MC shows that GBMF is about 100 m deeper in the lower reaches (Figure 4.19a, 4.18 km 5 to 20), i.e. 5%, but within error bars. Farther upstream, the two solutions are in good agreement (Figure 4.19b,c). Comparing the errors from GBMF and MC (Figure 4.14), the MC result has an uncertainty of 100 m over most of the trough, whereas GBMF has an error varying from 30 m to 140 m. Farther upstream, the errors in MC and GBMF are more similar.

B2013 has a sill depth of 200 m (km 5) in the fjord that is an artifact and a bump at 400 m depth (km 8 to 11) that is also an artifact. The B2013 bed depth is 600 m too shallow compared to GBMF, or 60% at km 10. The difference remains above noise level until km 30. The two solutions do not converge until km 45. The bumps along AA′ from km 5 to 30 are not confirmed by the GBMF or MC. We attribute these artifacts to kriging of sparse radar data, a more detailed discussion of these could be found in the supporting information (Figure 4.20, 4.21) (*Bamber et al.*, 2013; *Joughin et al.*, 2014).

Comparing the GBMF results with MCoRDS, we find a reasonable agreement above km 33 (Figure 4.19c), but errors as large as 500 m at km 14 (Figure 4.20, 4.21). We attribute this discrepancy to the difficulty of identifying bed echoes near the ocean margin (*Gogineni et al.*, 2014). We also compare the results with C2009 along the profile from *Joughin et al.* (2014) (Figure 4.22) and along the line of deepest bed (Figure 4.18). We find significant differences of 200-300 m and a poor correlation in bed variability below km 30.

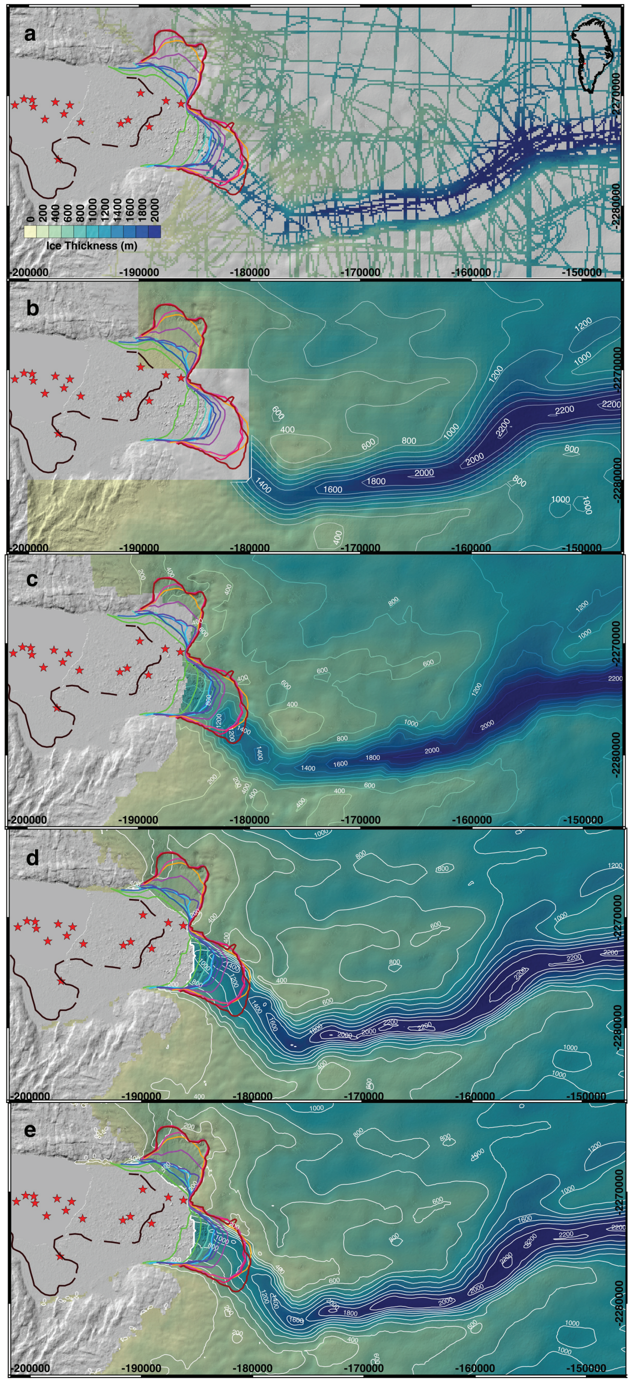

Figure 4.20: Ice thickness of Jakobshavn Isbræ, West Greenland (in meters of solid ice) from (a) CReSIS radar-derived thickness profiles color coded from yellow (no ice) to green and blue (up to 2,000 m of ice), (b) a 500 m thickness grid by CReSIS from 2006 to 2014 composite, (c) *Bamber et al.* (2013), (d) MC and (e) ice thickness derived from GBMF gravity data. Contour level is every 200 m of solid ice. Grounding line positions are color coded from brown (1996 from ERS-1/2) to green, blue, and red (2004 to 2015 from Landsat image). Red stars show the location of bathymetry measurements in Ilulissat fjord.

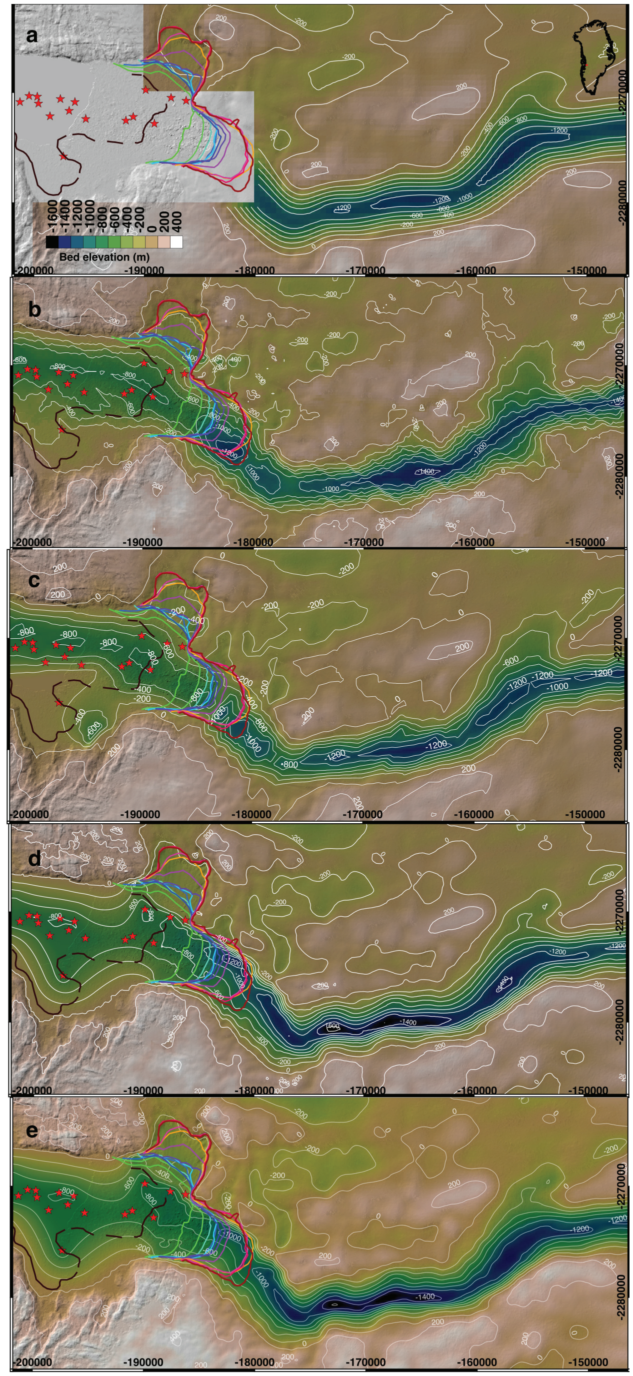

Figure 4.21: Bed elevation (in meters above sea level) of Jakobshavn Isbræ, West Greenland (a) a 500 m grid by CReSIS from 2006 to 2014 composite, (b) *Joughin et al.* (2014), (c) *Bamber et al.* (2013), (d) MC and (e) bed elevation inferred from the GBMF airborne gravity data. Contour level is every 200 m. Grounding line positions are color coded from black (1996) to brown (2015).

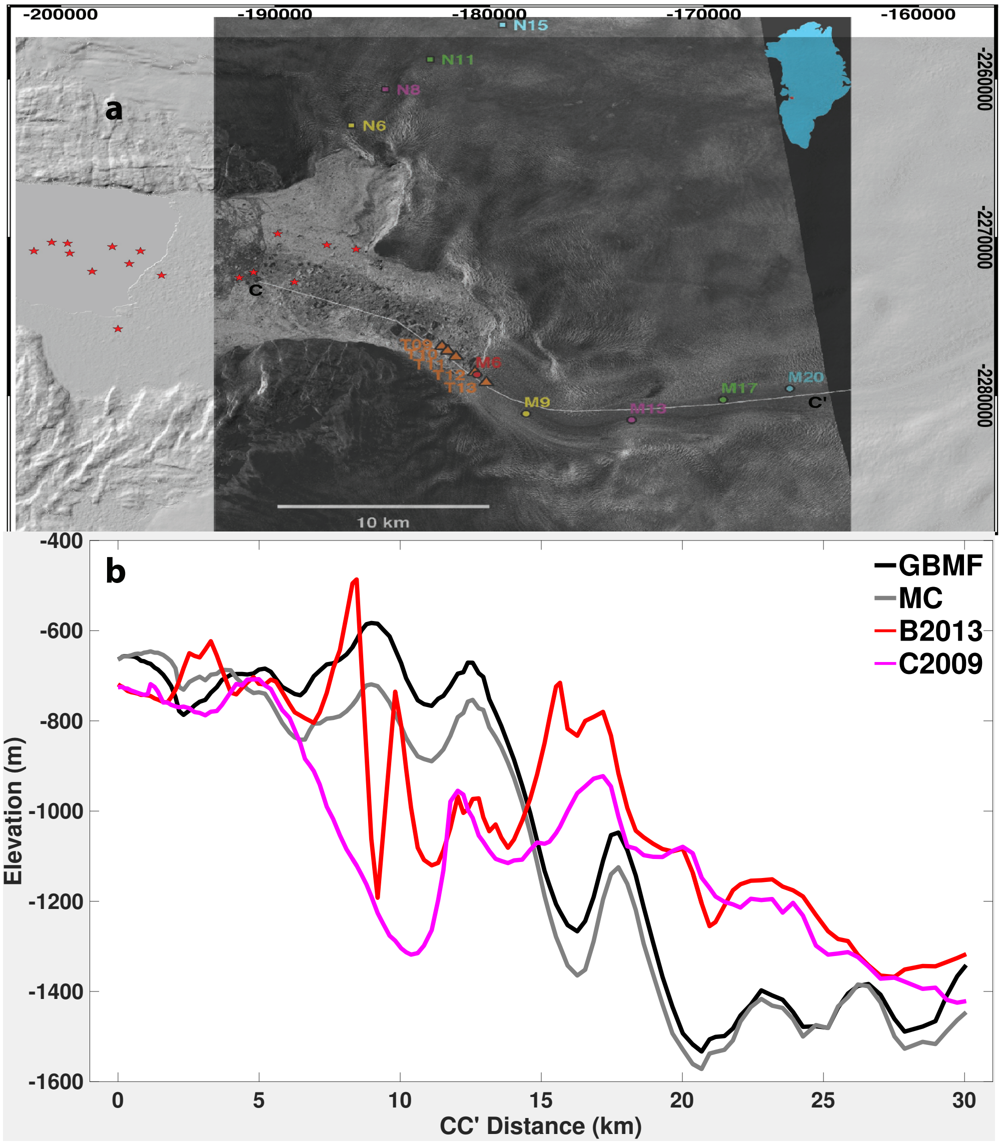

Figure 4.22: (a) Figure from *Joughin et al.* (2014) over Jakobshavn Isbræ, West Greenland, the white profile named CC′ overlaid on a shaded relief digital elevation model of Greenland (*Howat et al.*, 2014) and (b) bed elevation comparison along profile CC′ with GBMF,MC,B2013 and C2009. Red stars show the location of bathymetry measurements in Ilulissat fjord.

4.2.4 Discussion

Our inversion does not include a sediment layer. Inversions for basal shear stress (*Joughin et al.*, 2014; *Sergienko et al.*, 2014; *Shapero et al.*, 2016) suggest the presence of a weak bed, possibly a few meters to 100 m thick. In our inversion, introducing a layer of 100-m thick sediments would change the bed elevation by only 30 m. This magnitude uncertainty is less than the uncertainty of our gravity inversion. The GBMF result also agrees with MC in the upper part of the survey domain where quality thickness data exist, which suggests that the presence of sediments is not necessary to explain the gravity data.

Our study demonstrates the practical use of high-resolution airborne gravity to fill critical gaps in bed elevation in Greenland, especially in deep fjords that cannot be surveyed with deep radar sounders. If available, radar echo sounding would be preferable since these data are more precise (10-30 m versus 60 m) and higher resolution (10 m versus 750 m). Where reliable thickness data exist, the MC solution provides a high-resolution solution with low errors. Closer to the ocean margin where radar echoes are challenging to interpret, the gravity data offer a seamless mapping. To obtain a spatial resolution comparable to MC, the helicopter would need to fly at least twice slower, with a line spacing about twice denser, which would quadruple the cost of the survey.

Our results have implications for interpreting the retreat of JI since 1996. First, they suggest that the grounding line may have been anchored on a 700-m sill in the 1990s, before retreating into a fjord about 400 m deeper. Following the rapid retreat until 2012, the glacier has reached a higher bed which slowed down the retreat temporarily, as projected by *Joughin et al.* (2012) despite uncertainties in prior bed mappings. Second, during the retreat, as noted by *Joughin et al.* (2012), the glacier calving front has remained within 20 m of hydrostatic equilibrium. Ice front thickness will therefore increase from a current 1,100 m at km 12.5 (bed at 1,000 m depth) to 1,700 m when the glacier grounding line will reach at km 22 (bed about 1,500 m depth) or 50%, which will increase the ice discharge accordingly. Third, the results confirm that there is not major bed obstacle that could slow down the retreat at least until km 30. Fourth, the grounding line is currently 400 m deeper than estimated previously, hence thermal forcing from the ocean is 0.4°C greater from the pressure dependence of the freezing point of seawater alone.

At a fixed position along the glacier main trunk, the annual average ice velocity has been increasing steadily over time (*Joughin et al.*, 2014, e.g.). At the center of the calving front, however, we find that the mean annual speed averaged 12.6±0.9 km/yr from 2002 to 2015, listed in Table 4.1, i.e. the annual calving speed, which is the sum of the ice front speed and the retreat rate, has been about 13.2±0.9 km/yr, with little to no long term trend, hence equivalent to a maximum rate of calving.

Table 4.1: Ice speed at the center of the calving front from 2002 to 2015

Year	2002	2003	2004	2005	2006	2007	2008	2009	2010	2011	2012	2013	2014	2015
Ice speed (km/yr)	14.0	12.4	14.0	12.1	12.0	12.8	12.0	12.0	11.4	13.2	12.8	13.5	11.4	13.35

The new bed elevation confirms earlier studies (*Thomas*, 2004; *Joughin et al.*, 2012, e.g.) that JI is undergoing a marine ice sheet instability since it is retreating along mostly a retrograde bed. The retreat was likely triggered by an increase in ice shelf melt rate due to the intrusion of warmer AW in the fjord (*Holland et al.*, 2008). The current retreat rate of 0.6 km/yr is half as large as that observed in West Antarctica for Pine Island and Thwaites glaciers(1 km/yr) and one third as large as that experienced by Smith Glacier (2 km/yr) (*Rignot et al.*, 2014). These values place upper bounds on the current rate of retreat of large glaciers undergoing a marine instability. JI is probably retreating slower because it is confined in a deep trough with narrow sides that provide strong lateral resistance to flow.

4.3 3D modeling of two glaciers in Torssukatak Fjord, West Greenland

4.3.1 Introduction

Marine-terminating glaciers exert a significant control on the evolution of the Greenland Ice Sheet(GrIS) mass balance (*van den Broeke et al.*, 2009) and control 90% of the ice discharge into the ocean (*Rignot et al.*, 2010). Warm air temperatures thin the glaciers from the top. Warm oceans erode the submerged grounded ice, causing the grounding line to retreat. However, the glaciers bed topography is poorly known. As a result, it is difficult to project their evolution as they retreat inland, and to understand and quantify the role of ocean warming - a major source of climate forcing in Greenland- in the fjords. A recent study has shown that terminal glacier valleys were poorly characterized by earlier mappings and are far deeper and extend farther inland below sea level than previously thought (*Morlighem et al.*, 2014). The deep valleys were generated by the long-term erosion of glacial channels during ice ages. Near the grounding line of these glaciers, however, the uncertainty of the reconstruction is large, for several reasons. First, this location is the furthest away from quality radar sounding profiles that constrain the inversion; second, this area experience high rates of thinning and summer melt that are both not well known at that level of spatial details; the rate of thinning is traditionally not well sampled in narrow, steep terminal valleys; and the rate of melt is constrained by the spatial resolution of reconstructions of surface mass balance, typically about 11 km using the Regional Atmospheric Climate Model (RACMO). It is however important to constrain the reconstruction of ice thickness at the ice front because its position with respect to the bed topography is important for determining the glacier stability and sensibility to climate forcing both from the atmosphere and the ocean. Similarly, the sea floor bathymetry is not well known in Greenland's fjords (*Jakobsson et al.*, 2012), especially near glacier fronts which are typically chocked with iceberg debris and regularly scoured by calving events.

Sermeq Avangnardleq (AVA) (70° 3′ N, 50° 19′ W) and Sermeq Kujatdleq (KUJ) (69° 59′ N, 50° 10′ W) are two ocean-terminating outlet glaciers in central West Greenland, flowing into the ice-choked Torssukatak fjord (TOR). The fjord extends 50 km westwards, and merges into Vaigat Fjord, a large fjord to the north of Disko Island. For the fastest-flowing glacier of GrIS, Jakobshavn Isbræ (JI), its front receded 26 km during the period 1851-1953. Since 1953, the position of its terminus has been stable. AVA and KUJ generally receded only a little during the same period (*Atlas et al.*, 1913). Since 1985, based on the high resolution digital elevation models (DEMs), AVA has gained mass and its terminus has remained stable, however, for KUJ catchment, there is a thinning extending 15 km up-glacier from its terminus (*Felikson et al.*, 2017).

4.3.2 Data and Methods

Gravity data has already been discussed in Chapter 2. The MultiBeam Echo Sounding data (MBES) collected in the Vaigat Fjord, which includes Ata Sund and TOR, hosts four major outlet glaciers, AVA, KUJ, Kangilerngata Sermia and Eqip Sermia since 2007 with a Kongsberg-Simrad EM120 system (*Weinrebe et al.*, 2009). In August 2012, 2013, 2014 and 2015, our group employed a Reson 8160 MBES system started in Ilulissat and proceeded through Ata Sund, TOR, Vaigat Fjord, and Uummannaq Fjord, extending to the glaciers' termini (*Rignot et al.*, 2016). Until the summer of 2016, during the Ocean Melting Greenland (OMG) mission, we mapped the fjord bathymetry near the ice fronts for the first time. Bathmetry was on a 25 m grid with a nominal precision of 1-2 m (Figure 4.27). We manually traced the glaciers front positions from aerial photography since 1964 (*Carbonnell and Bauer*, 1968), with a 10-year interval between 1964 and 1985, several years between 1985 to 1999, and yearly intervals thereafter from Landsat multispectral scanner images in 1975 until Landsat

8 (Figure 4.23).

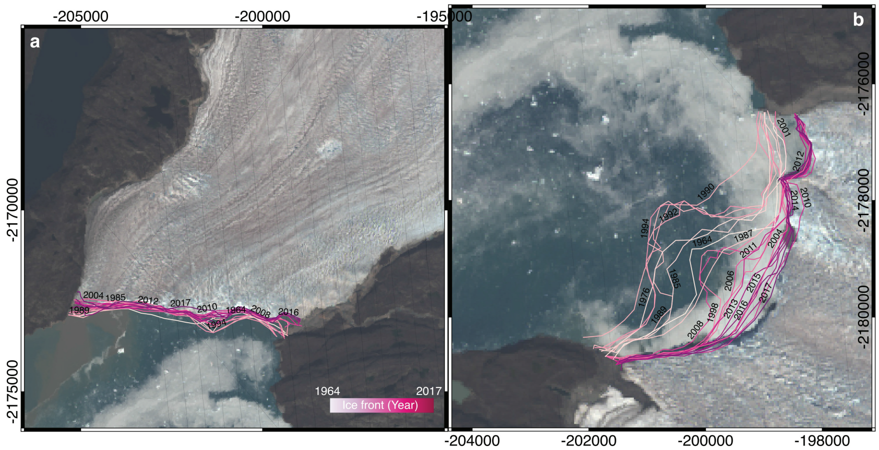

Figure 4.23: Ice front positions of (a) Sermeq Avangnardleq (AVA), and (b) Sermeq Kujatdleq (KUJ), central West Greenland. Color coded from yellow (1964) to dark green (2017), overlaid on a Landsat-8 image.

We performed a three-dimensional model of AVA and KUJ using Geosoft GM-SYS 3D software which implements *Parker* (1973)'s method. The model included three horizontal layers: 1) a solid ice layer with a density of 0.917 g/cm^3; 2) a sea water layer with a density of 1.028 g/cm^3; and 3) a rock/sediment substrate layer with a uniform density of 2.60 g/cm^3 for AVA; 2.59 g/cm^3 for KUJ. For these two glaciers, because the smaller domains than JI, we only allow a 500 m wide transition at the ocean boundary and inland at the boundary with the MC solution for inversion. We calculate the DC-shift of the gravity data on the points where the MC data overlapped with gravity measurements of lower errors. In order to provide a constant data set, we gridded our final bed elevation ot the spacing of the MBES, which is 25 m (Figure 4.27 b). Density selection is decided by the rate of convergence of the solution in terms of the bed elevation changes between modeled and initial bed for densities varying from 2.5 to 3.0 g/cm^3 with steps of 0.03 g/cm^3. We find a minimum at a density of 2.60 g/cm^3 for AVA and 2.69 g/cm^3 for KUJ (Figure 4.24), which are also correspond with the tonalite, granite and sandstone in this area based on the geological information from the Geological Survey of Denmark and Greenland (*Pedersen et al.*, 2013).

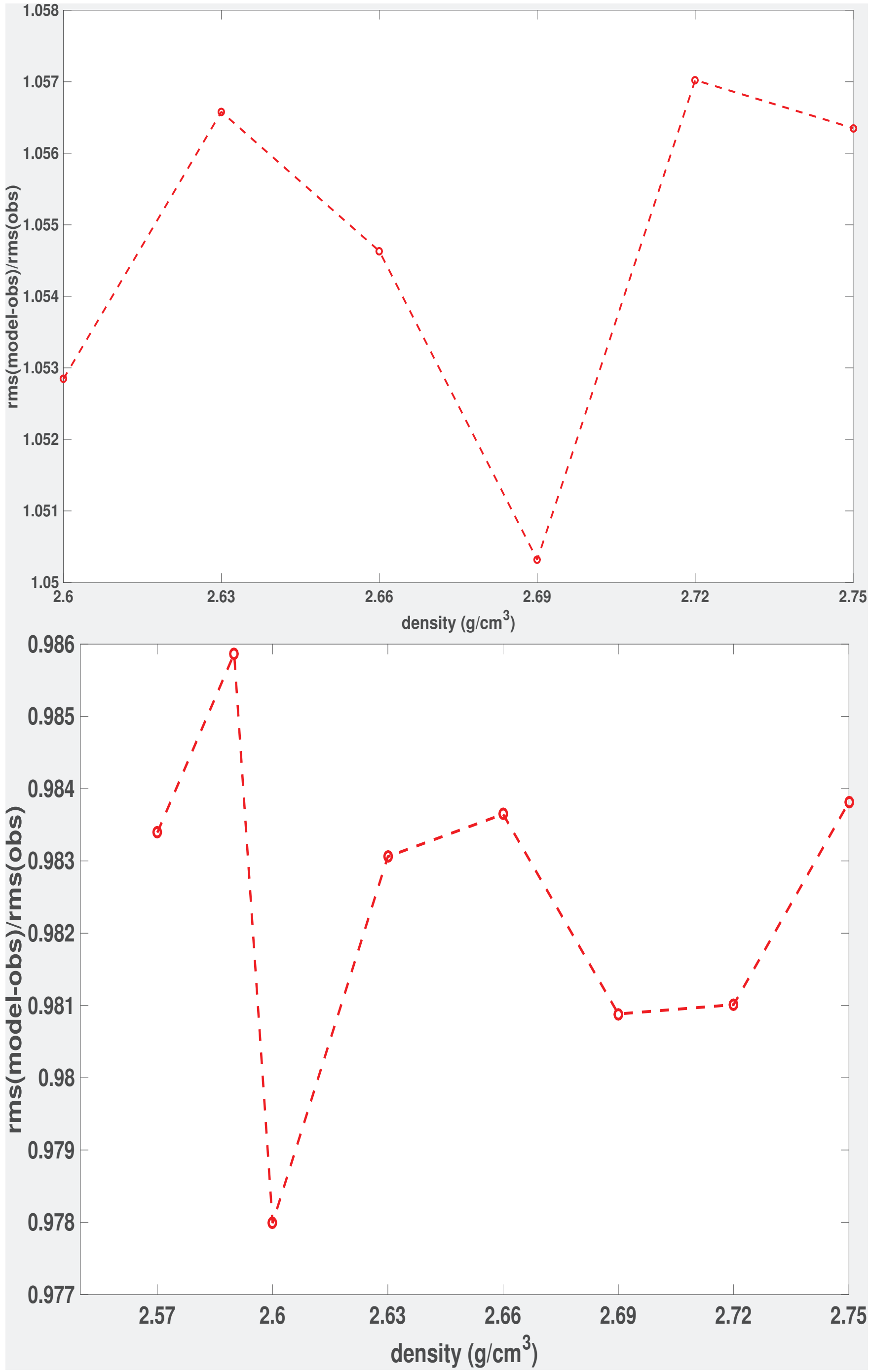

Figure 4.24: Optimization of the bedrock density beneath Sermeq Avangnardleq (AVA) and Sermeq Kujatdleq (KUJ), central West Greenland, obtained by comparing the r.m.s. of the modeled gravity solution versus the observed gravity divided by the r.m.s of the observed gravity for density values varying from 2.5 to 3.0 g/cm^3. The results reveal the existence of a minimum at a density of 2.60 g/cm^3 for AVA and 2.69 g/cm^3 for KUJ. The density value we used also corresponds to tonalite, granite and sandstone, present in this area according to the geologic maps of the Geological Survey of Denmark and Greenland (GEUS).

Data from the upper reaches of the model domain were used *Morlighem et al.* (2014) to produce an updated MC solution for the bed and ice thickness. The MC solution is a high resolution (150 m) map obtained by combined the radar-derived ice thickness data with ice flow vectors from satellite radar interferometry, reconstructed surface mass balance data, and ice thickening rates from OIB laser altimetry data. The MC map is significantly better in terms of resolution and accuracy than *Bamber et al.* (2013)'s 1-km spacing map (B2013) which combined thickness data from MCoRDS using kriging with the International Bathymetric Chart of the Arctic Ocean (IBCAO) v3 in the fjord (*Jakobsson et al.*, 2012) (Figure 4.26). Data quality for MC is expected to decrease closer to the ice front as errors accumulate downstream from errors in ice flow direction, surface mass balance, and ice thinning rates.

We use the similar method we did for JI using the gravity misfit, i.e. modeled gravity minus observed gravity, to quantify the uncertainty of the Inversion (Figure 4.25).

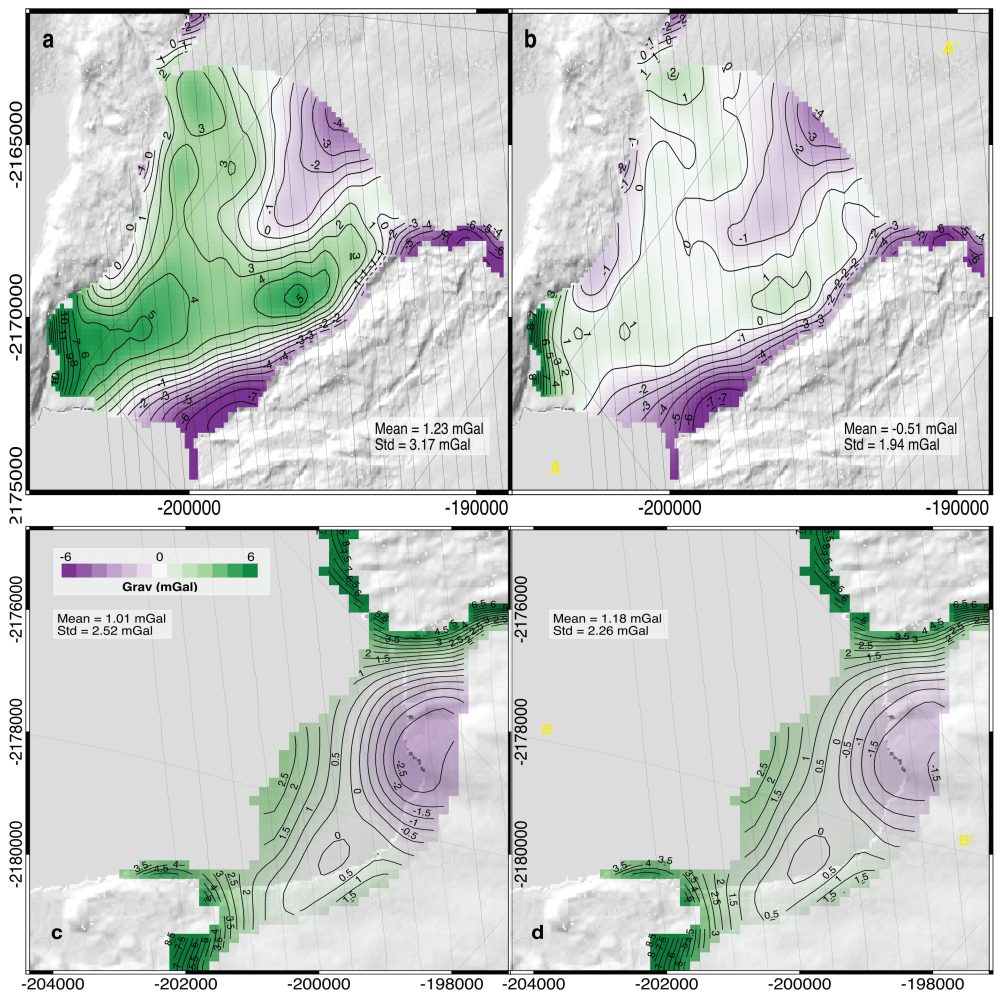

Figure 4.25: Bed elevation of Sermeq Avangnardleq (AVA) and Sermeq Kujatdleq (KUJ), central West Greenland. (a) *Bamber et al.* (2013) (b) bed elevation, fjord bathymetry from a 3D inversion of the GBMF gravity data in black boxes and MC solution color coded from white to orange (500 m to 0 m above sea level) to green, blue and dark blue (100 to 700 m below sea level) with 100-m contours in white. Projection is EPSG 3413, WGS84/NSIDC sea ice polar stereographic north.

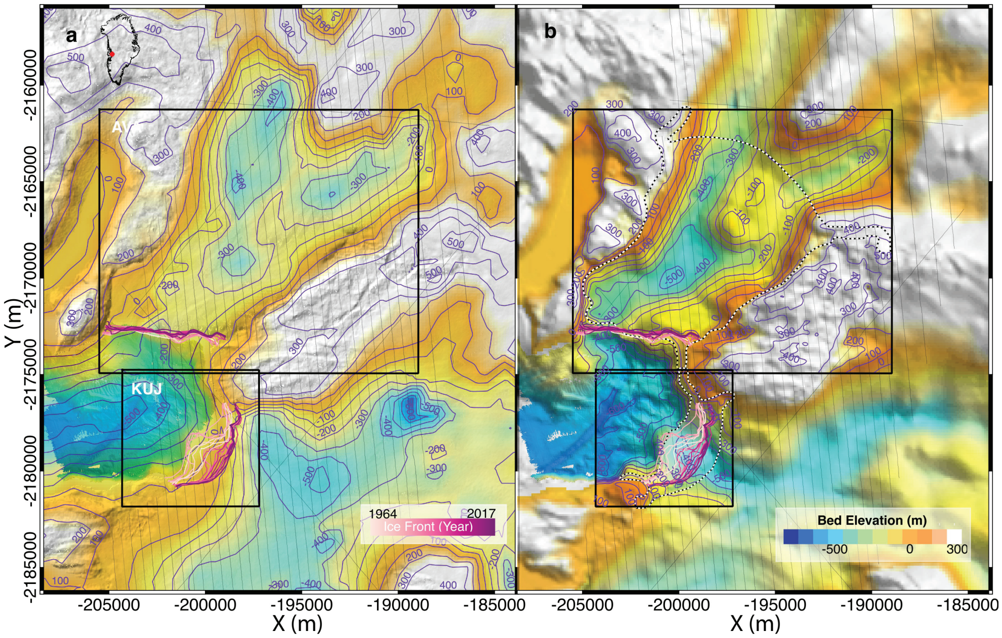

Figure 4.26: Bed elevation of Sermeq Avangnardleq (AVA) and Sermeq Kujatdleq (KUJ), central West Greenland. (a) *Bamber et al.* (2013) (b) bed elevation, fjord bathymetry from a 3D inversion of the GBMF gravity data in black boxes and MC solution color coded from white to orange (300 m to 0 m above sea level) to green, blue and dark blue (100 to 800 m below sea level) with 100-m contours in white. The limits of gravity inversions are thin white-black dash lines within each black box. Projection is EPSG 3413, WGS84/NSIDC sea ice polar stereographic north.

4.3.3 Results

The observed gravity anomalies within the survey domain vary from -95 mGal to 35 mGal, with peak values over ocean and near the grounding zones (Figure 4.27a). The bed elevation is well correlated with the gravity anomaly, as expected (Figure 4.27), i.e. largely negative gravity anomalies correspond to areas of thicken ice thickness and deeper bed elevation. For AVA, the inferred bed elevations vary from 552 m above sea level (asl) in the exposed two rocks areas to 565 m below sea level (bsl) in the two trough tributaries (Figure 4.28). For KUJ, the bed elevation range from 300 m asl to 650 bsl in the open ocean. Here we use the intersections between ice front position in 1964 and the two lines AA′ (2014041402) and BB′ (2013040601) (*Leuschen et al.*, 2010, updated 2017) recorded by the Multi-channel Coherent

Radar Depth Sounder (MCoRDS) radar, which is developed by the University of Kansas' Center of Remote Sensing of Ice Sheets (CReSIS), as absolute references for each glacier. Large (> 60 m) bumps and hollows in inferred bed elevation are above the noise level and reflect actual topographic features. We find no obvious correlation between the gravity misfit and bed elevation, which increases confidence in the results.

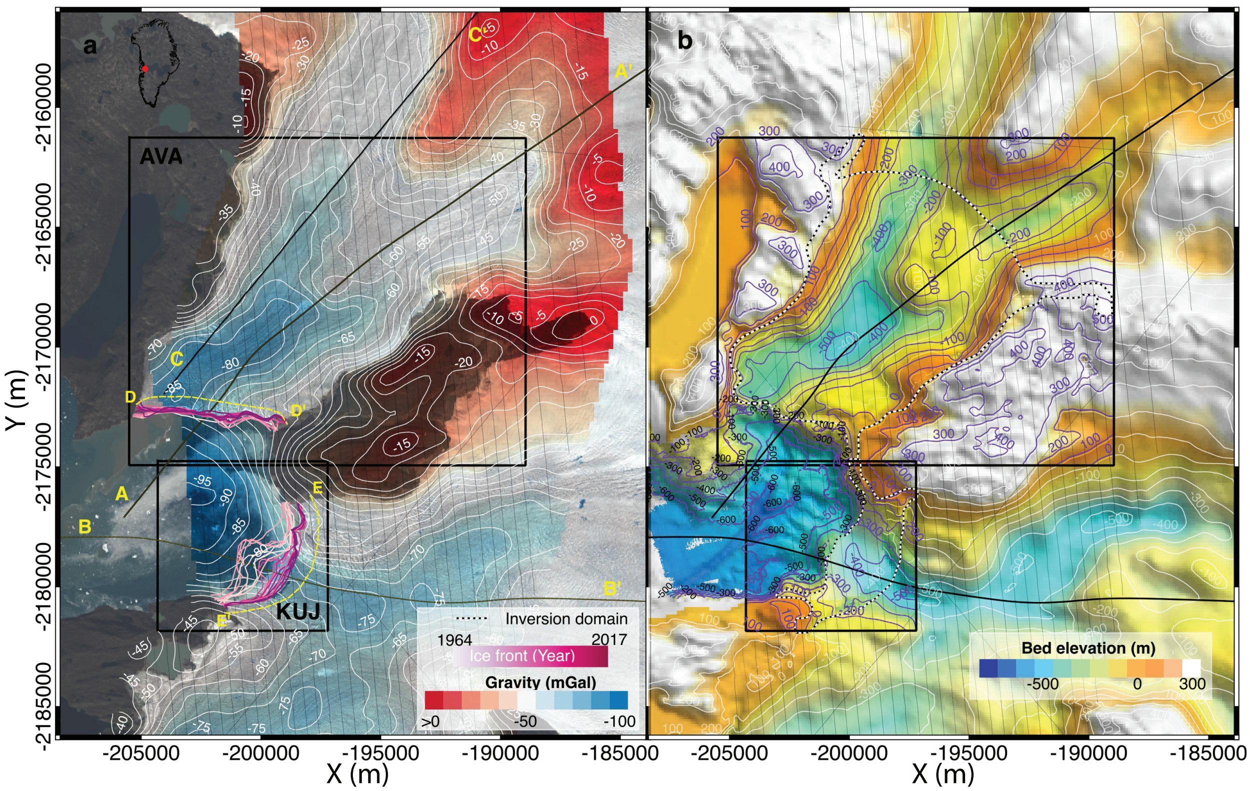

Figure 4.27: Bed elevation of Sermeq Avangnardleq (AVA) and Sermeq Kujatdleq (KUJ), central West Greenland. (a) Airborne, high-resolution, free-air gravity anomalies measured in 2012 for the GBMF survey with a color scale in mGal (1 mGal=10^{-5} m^2/s) and 10-mGal contours in white. Survey lines are thin black lines. Grounding line positions are color coded from snow (1964) to pink (2017 from Landsat). The limits of gravity inversions are thin white-black dash lines within each black box, overlaid on a Landsat-8 mosaic of Greenland. Inset on top left shows glacier location in Greenland. (b) bed elevation, fjord bathymetry from a 3D inversion of the GBMF gravity data in black boxes and MC solution color coded from white to orange (300 m to 0 m above sea level) to green, blue and dark blue (100 to 800 m below sea level) with 100-m contours in white. Profile AA′ and BB′ are shown in Figure 4.28 and Figure 4.29. Projection is EPSG 3413, WGS84/NSIDC sea ice polar stereographic north.

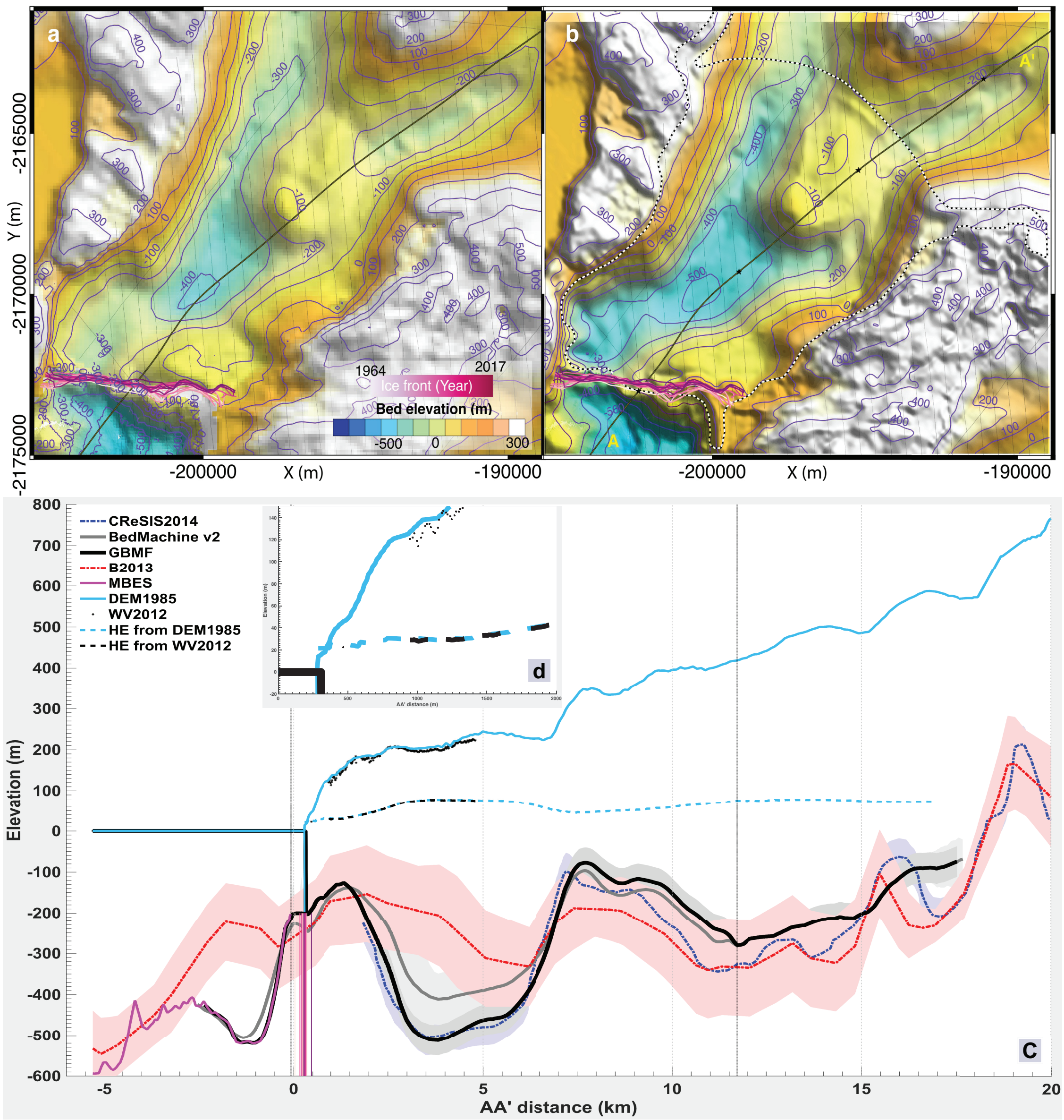

Figure 4.28: Bed elevation of Sermeq Avangnardleq (AVA), central West Greenland. (a) MC solution in land and multibeam echo sounding (MBES) in the ocean. (b) bed elevation form GBMF data gridded in 25 m. Color coded from white to orange (300 m to 0 m above sea level) to green, blue and dark blue (100 to 800 m below sea level) with 100-m contours in purple. Profile AA′ is the Multi-channel Coherent Radar Depth Sounder (MCoRDS) radar by CReSIS in 20140414. Black stars indicate 5 km intervals starting from the 1964's ice front. (c) Profile AA′ by CReSIS in 20140414 showing the glacier surface and bed elevation from different solutions. The solution from this study (GBMF gravity data) is black for bed (inversion) with error bars in dark gray, and hydrostatic equilibrium in dash line. The MC solution (*Morlighem et al.*, 2014) is light gray with error bars in lighter gray. The solution from MCoRDS is in blue. The solution from *Bamber et al.* (2013) is red for the bed with error bars in light red. The MBES measurement is magenta. The DEM 19850709 is deepskyblue solid line with HE dash line. (d) Zoom in map of the ice front area in (c) km 0 to km 2.

We obtain a smooth transition in bed topography between the GBMF data, the fjord bathymetry, and the MC solution. The entrance of TOR has a 300 m sill and the whole fjord is 700 - 800 m deep uniformly, however, shallows near the glaciers (*Rignot et al.*, 2016). During the mission of OMG in 2016, we mapped the fjord bathymetry close to ice front of AVA for the first time. Only left a small area not mapped because of the rarely ice free condition, which is only about 200 - 500 m to AVA's ice front (Figure 4.28 a). A 200 m sill is found at the mouth of AVA, for more than a century, the ice fronts of this glacier just hover on this sill with a movement within 150 m (Figure 4.28 b). For KUJ, there is a 3 km gap between MBES measurements and current ice front position (Figure 4.29 a), which is filled by gravity inversion (Figure 4.29 b).

A comparison of the GBMF results with MC, MCoRDS and B2013 of AVA was made based on the CReSIS line AA′ (Figure 4.28 b, 4.28 c). First, the bed elevation is deeper than the MC solution by 100 m between km 2 to 6. Further upstream, these two solutions are in better agreement (Figure 4.28 c). Errors in the MC product are highest at low elevation, which are originated from errors in radar-derived thickness, ice flow direction, and correction for glacier thinning, which accumulate in the ice flow direction. We let our inversion end around km 12 to match MC solution beyond the inversion domain for further correction of MC solution and future application. The differences with B2013 are larger. In the fjord, B2013 has a sill depth of 200 m (km -5) which is an artifact could be proved by our MBES data. On grounded ice, B2013 has a bump 200 m bsl (km 2 to 4) that is not confirmed by MCoRDS, MC or GBMF. Between km 7 to 10, the B2013 bed elevation is 100-m shallower than the other three datasets. Farther upstream, B2013 begins to follow MCoRDS until km 22 (the boundary of our figures' domain). Comparing the GBMF results with the MCoRDS, we find a perfect agreement from km 2 to 7. Although near grounding line the MCoRDS has difficulty to identify the bed echoes in the radar echogram, its did a good job more inland (*Gogineni et al.*, 2014). That's also the reason why we choose this line to do the comparison.

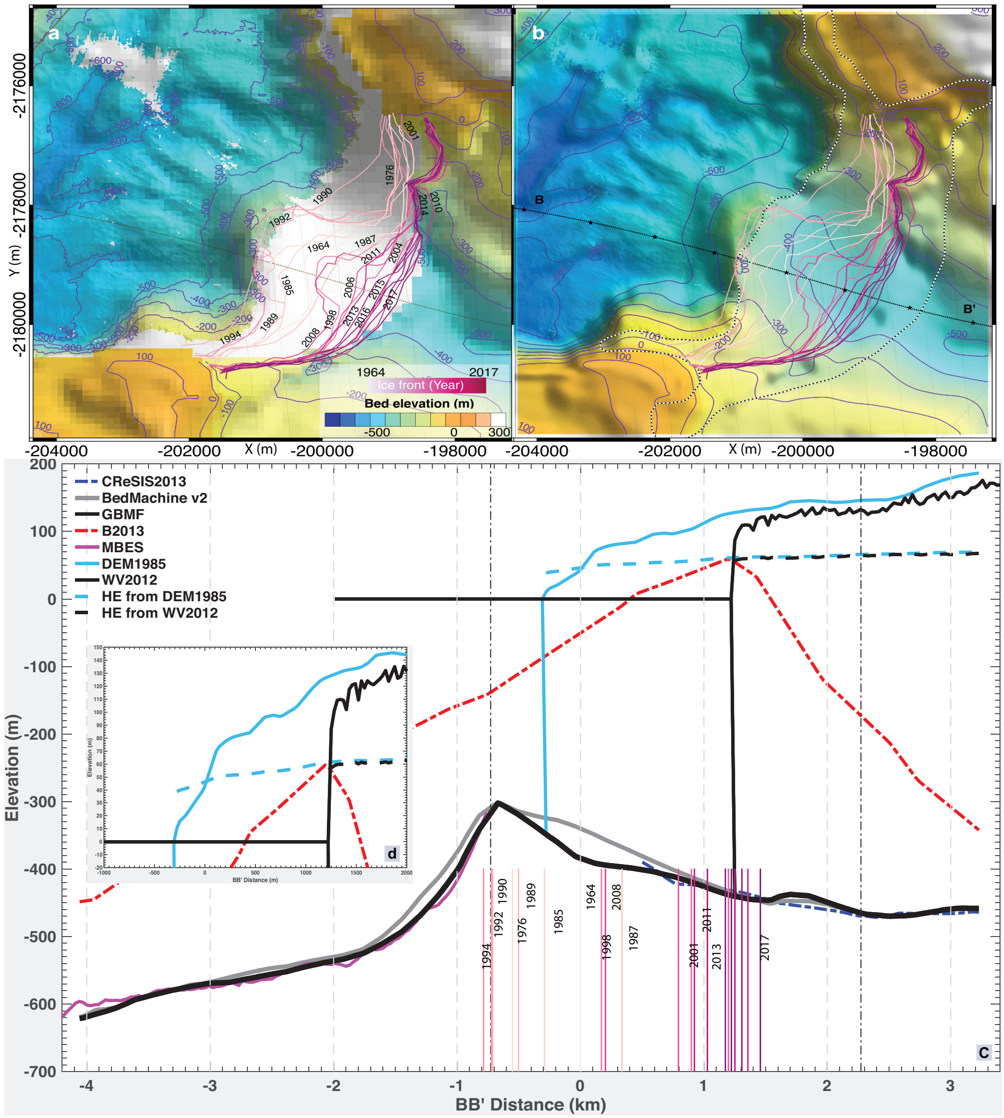

Figure 4.29: Bed elevation of Sermeq Kujatdleq (KUJ), central West Greenland. (a) MC solution in land and multibeam echo sounding (MBES) in the ocean. (b) bed elevation form GBMF data gridded in 25 m. Color coded from white to orange (300 m to 0 m above sea level) to green, blue and dark blue (100 to 800 m below sea level) with 100-m contours in purple. Profile BB′ is the Multi-channel Coherent Radar Depth Sounder (MCoRDS) radar by CReSIS in 20130406. Black stars indicate 1 km intervals starting from the 1964's ice front. (c) Profile BB′ by CReSIS in 20130406 showing the glacier surface and bed elevation from different solutions. The solution from this study (GBMF gravity data) is black for bed (inversion) and hydrostatic equilibrium in dash line. The MC solution (*Morlighem et al.*, 2014) is light gray with error bars in lighter gray. The solution from MCoRDS is in blue. The solution from *Bamber et al.* (2013) is red for the bed with error bars in light red. The MBES measurement is magenta. The DEM 19850709 is deepskyblue solid line with HE dash line. (d) Zoom in map of the ice front area in (c) km -1 to km 2.

Comparison of KUJ was also made on the CReSIS line BB′ (Figure 4.29 b, 4.29 c). A 300 m deep sill in front of the KUJ blocks the exit of icebergs, which made it impossible for standard vessels to penetrate the fjord to measure its depth. So the MBES measurements stopped at 3 km from the ice front during OMG 2016 mission, which is also the positions for ice fronts in year 1989, 1990 and 1994. First, within 1 km at km 0, GBMF bed elevation is 50 m deeper than MC. Then from km 0.5 to the end of inversion domain, GBMF and MC match with MCoRDS very well, except B2013's bed elevation (Figure 4.29 c); a more detailed discussion of these could be found in Figure 4.26 (*Bamber et al.*, 2013). A 450 m bump is in between km 1 to 2, where is the zone for the rest of the ice fronts until 2017.

4.3.4 Discussion

The results obtained in the TOR fjord for AVA and KUJ filling the gaps and providing a better fit with the MC reconstruction inland and the MBES offshore. This demonstrates the practicality of using high-resolution airborne gravity to invert bed elevation and ocean bathymetry, especially for deep fjords that are blocked by icebergs, brash ice and ice mélange. Radar echo sounding is more precise (10-30 m) than gravity (60 m), hence direct measurements with radar echo sounding still remain preferable where possible. Because there are no geologic constraints to determine the existence, thickness and density of potential sediments in these areas, we did not include a sediment layer in our model. GBMF solution is only affected by potential lateral and longitudinal variations in sediment thickness, not by its absolute value, so we conclude that our results are robust to the presence of sediments (*An et al.*, 2017).

In August 2008, water velocity, temperature and salinity were measured 4 km from the ice fronts in TOR fjord (*Rignot et al.*, 2010). Subglacial water discharge drives ocean convection, drawing deep, warm saline waters towards the near-vertical terminal ice face. The warm ocean waters melt ice along the calving face, and contribute to the overflow plume. In Tor, salinity and temperature increase with depth and small jets are found in the top 60 m to the north and middle of the fjord, all drawing water away from the glacier front.

Our results have implications for interpreting the stability of AVA since 1964. First, it suggests that the ice front of 1964 was anchored on a 250-m sill (km 0). The inversion reveals that from km 0 to 2, there is another much shallower sill at the mouth of AVA. The bed elevation rises for about 50 m as a prograde bed at this position. As a major bed obstacle downstream, this could prevent further glacier retreat. Hence, all the ice fronts from the rest of the record all hover within km 1 (Figure 4.28 c). Second, beyond km 2, the bed begins to drop to 500 m bsl, which is consistent with the observed pattern from MCoRDS. The deepest part of AVA is 565 m bsl in the middle of the glacier between km 3 and 4. Third, the GBMF bed is smoother and more uniform than that derived from the kriging of sparse data.

KUJ is also stable compared to the other glaciers in this area. First, there is a 300-m sill at the edge of our MBES measurements, where the 1989, 1990 and 1994's ice fronts sit on, although the ice front of 1964 is 1 km behind these three. Second, bed becomes 100 m deeper at km 0 and then with shallow slope but flatter than before. That makes the rest of ice fronts wander around between km 0 to 2. Entirely, the KUJ has a gently retrograde bed further inland. Similar for both AVA and KUJ, because of the smaller depth of these two glaciers, it prevents thermal forcing from sea water to melt and undercut the glacier front.

Submarine melting is a major ablation process across the tidewater glacier fronts, because of a two-order of magnitude larger than surface melt rates in the lower 5 km of Eqip Sermia, Kangilerngata Sermia and TOR in July to August 2008 calculated by *Rignot et al.* (2010). The warm, subsurface waters off the coast of west Greenland are fed from the east by the subpolar gyre of the North Atlantic via the Irminger current (*Myers et al.*, 2007). The subpolar gyre is influenced by the North Atlantic Oscillation (NAO) and it had a big change during the winter of 1995 - 1996 which allowed warm subpolar waters to spread westward, beneath colder surface polar waters (*Holland et al.*, 2008). It explains why JI had a rapid thinning since 1997 from prior years of slow thickening (*Thomas et al.*, 1995). Because of the nearby location, and with such a large-scale change in the subpolar gyre, the retreat of KUJ's ice front in 1998 could be also explained.

4.4 Conclusion

We employ high-resolution airborne gravity acquired at a low aircraft speed, with low ground clearance, to resolve the bed topography - and ice thickness - of Store glacier, Jakobshavn Isbræ, and two glaciers, which are Sermeq Avangnardleq and Sermeq Kujatdleq in Torssukatak Fjord of west Greenland in three dimensions using observational constraints off shore (bathymetry) and on shore (MC solution). The results provide a more definite view of the bed topography of these major glacier system than available previously, however, at a spatial resolution of 750 m along the trough and with an average precision of about 60 m. For Jakobshavn Isbræ, the results reveal an asymmetric bed in the lower reaches of the glacier, with a deeper bed along the northern flank of the trough, and a bed 300-400 m deeper on average than estimated previously, yet consistent with the presence of a retrograde bed favorable to fast retreat. The bed configuration upstream of the current grounding line suggests that the glacier will continue retreating for many decades to come. A more detailed analysis of the glacier ice flow evolution requires a numerical model. Earlier results probably portrayed scenarios for the future evolution of glaciers that were too conservative because they relied on a bed too shallow by a factor of two, hence a driving stress that was too small by a factor of two. The seamless topography obtained across the grounding line reveal the presence of a 300-m sill for AVA, which explains why this glacier has been stable for a century, despite changes in surface melt and ocean-induced melt and the presence of a deep fjord (800 m) in front of the glacier. For KUJ, we also reveal the presence of a wide sill (450 m depth) near the current ice front, witch explains its stability and the stranding of iceberg debris in front of the glacier. The GBMF bed data provide the first reliable description of the bed topography and ice thickness for these glaciers.

Chapter 5

Conclusions

5.1 Summary of Results

Mass loss in Greenland is primarily due to rapid changing of tidewater glaciers. To understand the drastic evolution of these glaciers, it is essential to know the glacier thickness, bed elevation below sea level, and fjord bathmetry in front of these glaciers. The use of gravity inversion to fill gaps in bed maps of outlet glaciers is a new area of study in cryosphere science because of previous limitations in the availability of gravity measurements. There are several studies that have employed gravity data on glaciers before this dissertation. These previous studies were based on the measurements from NASA's Operation IceBridge covered both Greenland and Antarctica. One study identified the first bathymetry model of the underlying continental shelf Larsen C (*Cochran and Bell*, 2012). Another study identified an offshore ridge underneath Thwaites Glacier (*Tinto and Bell*, 2011), and also a study investigated subglacial bathymetry and sediment layer distribution beneath the Pine Island Glacier ice shelf (*Muto et al.*, 2013).

This dissertation mainly focused on 3D gravity inversions of major glaciers in Greenland.

High-resolution gravity data is combined with novel measurements of fjord bathymetry and bed topography reconstructed by the mass conservation (MC) approach (*Morlighem et al.*, 2014). The major findings of this dissertation are as follows:

1) The new bed elevation confirms earlier studies (*Thomas*, 2004; *Joughin et al.*, 2012, e.g.) that Jakobshavn Isbræ (JI) is undergoing a marine ice sheet instability, since it is retreating along a retrograde bed. This is the first solution of bed topography of JI from high-resolution gravity data (750-m spatial resolution and 0.5-mGal precision) combined with geological constraints, like bathymetry measurement points from eXpendable Current profiler (XCP) and Conductivity Temperature Depth (XCTD) probes dropped from helicopters (*An et al.*, 2017). Based on the refined bed topography, we project that JI will keep retreating into deeper grounds for decades to come. The current retreat rate is 0.6 km/yr; the rate of retreat will be slower in the future due to the existence of a deep trough with narrow sides that provides strong lateral resistance to flow. We use the gravity misfit, which ranges from -3 to +3 mGal, to quantify the uncertainty of the inversion of our bed mapping, which is about 60 m.

2) High-resolution gravity data in the 3D inversion helps fill gaps in major outlet glacier bed mapping where traditional deep radar sounding methods fail. Gravity data acts as a bridge between multibeam echo sounding (MBES) measurements in the fjord and MC reconstruction bed elevation inland areas.

3) With the simulation of the impact of a change in aircraft speed and ground clearance on the spatial resolution, noise level, and magnitude of the gravity anomalies recorded over the JI trough, A guideline is provided for future gravity surveys on investigating glaciers bed topography (Figure 2.4). Changing the ground clearance has a stronger impact on data quality than changing the speed. I conclude that while there is flexibility in aircraft speed below 70 m/s, it is critical to maintain a ground clearance < 200 m to detect the gravity anomaly over the JI trough within less than 5 mGal.

4) On land, the soundings of bed topography from the Multichannel Coherent Radar Depth Sounder (MCoRDS) are more precise (10-30 m versus 60 m) and exhibit higher resolution (10 m versus 750 m) than gravity inversion. The MC solution provides a high-resolution bed topography with low errors of reliable ice thickness data. However, for deep fjords like JI, the radar sounder signal is difficult to obtain due to thickness of ice by (>2 km), the presence of highly absorptive and temperate ice near the bottom, combined with high surface clutter caused by a broken up ice surface (*Leuschen et al.*, 2010, updated 2017). Radar echoes are challenging to interpret closer to the ocean margin. Hence, gravity data offers a seamless mapping both on land and in the ocean.

5) Similar to MBES data, the measured bathymetry data could have a nominal vertical precision of 1-2 m (*Rignot et al.*, 2016). However, standard vessels cannot penetrate the fjord to measure its depth due to the permanent presence of icebergs, brash ice, and ice mélange caused by deep sills at the mouth of the fjords which block the exit of icebergs. Hence, gravity inversion acts as a supplement for the fjords where surveys cannot be conducted due to current technical and environmental state. In the warmer climate, there would be increase in both oceanic and atmospheric temperature. Gravity inversion could provide guidelines for future ocean measurement campaigns. With the melting of glaciers, MBES can be applied for more ocean areas of bathymetry measurements.

6) The five-year mission, Oceans Melting Greenland (OMG) by NASA, started in 2015 was inspired by the early success of MBES mapping and gravity inversion and the goal of this mission focused on improving estimates of sea level rise from Greenland. This mission consists a ship collecting measurements of the depth and shape of the sea floor, as well as an aircraft measuring free-air gravity anomalies with the AIRGrav instrument in same sectors; collected data will be further employed in gravity inversion.

7) Density of rock is one of the important parameters in gravity modeling. To define an optimal average density for the glacier bed, we developed a method to calculate the rate of

convergence of the solution in terms of the misfit between modeled and initial gravity fields for densities varying in a range based on the local geological information by the Geological Survey of Denmark and Greenland (GEUS) (*Pedersen et al.*, 2013).

The GBMF data provides incomparable descriptions of bed topography of these glaciers when compared with other solutions, such as bed elevation by *Bamber et al.* (2013), in reasonable agreement with the MC reconstruction. This study provides simple guidelines to study in fjords often chocked up with iceberg debris, e.g., Helheim or Kangerdlugssuaq glaciers, or other glaciers in Southeast Greenland, including glaciers with poor radio echo sounding data near the calving fronts.

5.2 Implications for Future Research

This study provides some examples in gravity inversion on glacier bed topography and fjord bathymetry combined with other data to constrain the inversion processes. The inversion results give us a complete view of the glacier's revolution in the past and future development. At the same time, the results could be used in ice-ocean interaction models to predict the ocean effects on glacier melting in the ongoing warm climate. To further develop the gravity inversion models, we need more measurements from ocean, higher resolution and wider coverage in gravity datasets. Specifically, the following aspects need further study in the future:

1) Ongoing work of Helheim Glacier (HEL), (66.5° N, 38° W) is the fastest outlet glacier in the Southeast Greenland. To have a better understanding of this glacier's evolution and to overcome the difficulties in bathymetry measurements, because it plays an important role in the loss of ice from Greenland, we surveyed it with airborne gravimeter in Summer 2012. Based on the preliminary results on HEL, the geology is quite different in north and south

branches. Hence, further step for modeling will divide the HEL into two parts, and do the gravity inversion separately.

2) More constraints are needed in the gravity inversion models. The constraints could from ocean bathymetry measurements (MBES), more precise ice thickness measurements on land or seismic measurements overlapped with gravity data, e.g., I used for JI (*Clarke and Echelmeyer*, 1996). For example, Helheim Glacier in East Greenland, discharges into deep Sermilik Fjord, which is mostly covered by sea ice from January to June and a large ice mélange extends year-around (*Andresen et al.*, 2012). Moreover, all the gravity data used in this study has high-resolution and acquired by helicopter, which is relatively more expensive than other datasets. Therefore, guidelines on gravity survey are provided. More high-resolution gravity data will be acquired in the future.

3) More precise rock information beneath the glaciers are needed. In my gravity inversions, a homogeneous rock density is applied for the glacier bed. However, based on several other constraints, different rock types could be identified and then rock density distribution could be applied to gravity inversion model as well (*Greenbaum et al.*, 2015). A simple Bouguer slab calculation shows that each 100 m of sediment with density 2.2 g/cm^3 leads to a bed elevation overestimate by 30 m. This magnitude uncertainty is less than the uncertainty of our gravity inversion. Hence, we decide to not include sediment layer in our gravity model to avoid more unexpected uncertainties. However, with available sediment measurements or prediction from models, a sediment layer in the gravity model could be added to make the model more precise (*Gourlet et al.*, 2016; *Muto et al.*, 2016; *Koppes et al.*, 2015; *Andresen et al.*, 2012).

4) Based on my study, gravity models have already done a good job to help us obtain a seamless and smooth bed topography for glaciers. However, because of the ambiguity of inherent characteristics in gravity interpretations, magnetic data could be introduced as a supplement to identify the geologic boundary (*Tinto et al.*, 2015; *Greenbaum et al.*, 2015;

Bondzio et al., 2016).

5) This approach can be applied to other study areas where gravity surveys are available. However, there is a large variety of different glacier types. There are differences between large glaciers and small glaciers, Greenland glaciers and Antarctica glaciers, tidewater glaciers and glaciers with floating ice tongues. Also, different areas have different geological features, therefore models would need to be specific to each glacier.

In this dissertation, we employ high-resolution gravity data combined with the MC solution on land and MBES data in the fjord to resolve bed topography for several glaciers in Greenland. Similar methodology could be applied to other glaciers around the world. Furthermore, the gravity method can also used in industry to identify resources or minerals.

Bibliography

An, L., E. Rignot, S. Elieff, M. Morlighem, R. Millan, J. Mouginot, D. M. Holland, D. Holland, and J. Paden (2017), Bed elevation of Jakobshavn Isbrae, West Greenland, from high-resolution airborne gravity and other data, *Geophys. Res. Lett.*, *44*, 1–9, doi: 10.1002/2017GL073245.

Andresen, C. S., F. Straneo, M. H. Ribergaard, A. A. Bjørk, T. J. Andersen, A. Kuijpers, N. Nørgaard-Pedersen, K. H. Kjær, F. Schjøth, K. Weckström, and A. P. Ahlstrøm (2012), Rapid response of Helheim Glacier in Greenland to climate variability over the past century, *Nat. Geosci.*, *5*(1), 37–41, doi:10.1038/ngeo1349.

Argyle, M., S. Ferguson, L. Sander, and S. Sander (2000), AIRGrav results: a comparison of airborne gravity data with GSC test site data, *Lead. Edge*, *19*(10), 1134–1138, doi: 10.1190/1.1816088.

Atlas, S. I., U. States, G. Survey, and P. Paper (1913), the United States Geological Survey., *Science*, *37*(945), 205–9, doi:10.1126/science.37.945.205.

Bamber, J. L., J. A. Griggs, R. T. W. L. Hurkmans, J. A. Dowdeswell, S. P. Gogineni, I. Howat, J. Mouginot, J. Paden, S. Palmer, E. Rignot, and D. Steinhage (2013), A new bed elevation dataset for Greenland, *Cryosphere*, *7*(2), 499–510, doi:10.5194/tc-7-499-2013.

Bondzio, J. H., H. Seroussi, M. Morlighem, T. Kleiner, M. Rückamp, A. Humbert, and E. Y. Larour (2016), Modelling calving front dynamics using a level-set method: Application to Jakobshavn Isbræ, West Greenland, *Cryosphere*, *10*(2), 497–510, doi: 10.5194/tc-10-497-2016.

Braithwaite, R. J. (1995), Positive degree-day factors for ablation on the Greenland Ice-sheet studied by energy balance modeling, *J. Glaciol.*, *41*(137), 153–160, doi:10.3198/1995JoG41-137-153-160.

Carbonnell, M., and A. Bauer (1968), Exploration des couvertures photographiques aeriennes repetees du front des glaciers velant dans Disko Bugt et Umanak Fjord, *Medd. Groenl.*, *173*(5).

Clarke, T. S., and K. Echelmeyer (1996), Seismic-reflection evidence for a deep subglacial trough beneath Jakobshavns Isbræ, West Greenland, *J. Glaciol.*, *42*(141), 219–232.

Cochran, J. R., and R. E. Bell (2012), Inversion of IceBridge gravity data for continental shelf bathymetry beneath the Larsen Ice Shelf, Antarctica, *J. Glaciol.*, *58*(209), 540–552, doi:10.3189/2012JoG11J033.

Cochran, J. R., S. Elieff, J. Tinto, and K. Charles (2011), IceBridge Gravity Instrument Performance and Data Assessment.

Csatho, B., T. Schenk, C. J. Van Der Veen, and W. B. Krabill (2008), Intermittent thinning of Jakobshavn Isbrae, West Greenland, since the Little Ice Age, *J. Glaciol.*, *54*(184), 131–144, doi:10.3189/002214308784409035.

Echelmeyer, K., T. S. Clarke, and W. D. Harrison (1991), Surficial glaciology of Jakobshavn Isbrae, West Greenland: Part I. Surface Morphology, *J. Glaciol.*, *37*(127), 368–382.

Edwards, M. H., and B. J. Coakley (2003), CHEMIE der ERDE GEOCHEMISTRY INVITED REVIEW SCICEX Investigations of the Arctic Ocean System, *Earth Sci.*, *63*, 281–328.

Ettema, J., M. R. Van Den Broeke, E. Van Meijgaard, W. J. Van De Berg, J. L. Bamber, J. E. Box, and R. C. Bales (2009), Higher surface mass balance of the Greenland ice sheet revealed by high-resolution climate modeling, *Geophys. Res. Lett.*, *36*(12), 4–8, doi:10.1029/2009GL038110.

Felikson, D., T. C. Bartholomaus, G. A. Catania, N. J. Korsgaard, K. H. Kjær, M. Morlighem, B. Noël, M. van den Broeke, L. A. Stearns, E. L. Shroyer, D. A. Sutherland, and J. D. Nash (2017), Inland thinning on the Greenland ice sheet controlled by outlet glacier geometry, *Nat. Geosci.*, doi:10.1038/ngeo2934.

Fenty, I., J. Willis, A. Khazendar, S. Dinardo, R. Forsberg, I. Fukumori, D. Holland, M. Jakobsson, D. Moller, J. Morison, A. Münchow, E. Rignot, M. Schodlok, A. Thompson, K. Tinto, M. Rutherford, and N. Trenholm (2016), Oceans Melting Greenland: Early Results from NASA's Ocean-Ice Mission in Greenland, *Oceanography*, *29*(4), 72–83, doi:10.5670/oceanog.2016.100.

Filina, I. Y., D. D. Blankenship, M. Thoma, V. V. Lukin, V. N. Masolov, and M. K. Sen (2008), New 3D bathymetry and sediment distribution in Lake Vostok: Implication for pre-glacial origin and numerical modeling of the internal processes within the lake, *Earth Planet. Sci. Lett.*, *276*(1-2), 106–114, doi:10.1016/j.epsl.2008.09.012.

Gogineni, S., J. B. Yan, J. Paden, C. Leuschen, J. Li, F. Rodriguez-Morales, D. Braaten, K. Purdon, Z. Wang, W. Liu, and J. Gauch (2014), Bed topography of Jakobshavn Isbræ, Greenland, and Byrd Glacier, Antarctica, *J. Glaciol.*, *60*(223), 813–833, doi:10.3189/2014JoG14J129.

Gómez-Ortiz, D., and B. N. P. Agarwal (2005), 3DINVER.M: A MATLAB program to invert the gravity anomaly over a 3D horizontal density interface by Parker-Oldenburg's algorithm, *Comput. Geosci.*, *31*(4), 513–520, doi:10.1016/j.cageo.2004.11.004.

Gourlet, P., E. Rignot, A. Rivera, and G. Casassa (2016), Ice thickness of the northern half of the Patagonia Icefields of South America from high-resolution airborne gravity surveys, *Geophys. Res. Lett.*, doi:10.1002/2015GL066728.

Greenbaum, J. S., D. D. Blankenship, D. a. Young, T. G. Richter, J. L. Roberts, a. R. a. Aitken, B. Legresy, D. M. Schroeder, R. C. Warner, T. D. van Ommen, and M. J. Siegert (2015), Ocean access to a cavity beneath Totten Glacier in East Antarctica, *Nat. Geosci.*, *8*(March), 1–5, doi:10.1038/NGEO2388.

Hall, D. K., J. C. Comiso, N. E. Digirolamo, C. A. Shuman, J. E. Box, and L. S. Koenig (2013), Variability in the surface temperature and melt extent of the Greenland ice sheet from MODIS, *Geophys. Res. Lett.*, *40*(10), 2114–2120, doi:10.1002/grl.50240.

Hall, J. K., and Y. Kristoffersen (2009), The R/H SabvabaaA research hovercraft for marine geophysical work in the most inaccessible area of the Arctic Ocean, *Lead. Edge*, *28*(8), 932–935, doi:10.1190/1.3192839.

Harvey, P. K. (2005), *Petrophysical Properties of Crystalline Rocks*, 288 pp., Geological Society of London.

Hinze, J. W., R. R. B. von Frese, and A. H. Saad (2013), *Gravity and Magnetic Exploration: Principles, Practices, and Applications*, Cambridge University Press.

Holland, D. M., R. H. Thomas, B. de Young, M. H. Ribergaard, and B. Lyberth (2008), Acceleration of Jakobshavn Isbræ triggered by warm subsurface ocean waters, *Nat. Geosci.*, *1*(10), 659–664, doi:10.1038/ngeo316.

Howat, I. M., J. E. Box, Y. Ahn, A. Herrington, and E. M. McFadden (2010), Seasonal variability in the dynamics of marine-terminating outlet glaciers in Greenland, *J. Glaciol.*, *56*(198), 601–613, doi:10.3189/002214310793146232.

Howat, I. M., Y. Ahn, I. Joughin, M. R. Van Den Broeke, J. T. M. Lenaerts, and B. Smith (2011), Mass balance of Greenland's three largest outlet glaciers, 2000-2010, *Geophys. Res. Lett.*, *38*(12), 1–5, doi:10.1029/2011GL047565.

Howat, I. M., A. Negrete, and B. E. Smith (2014), The Greenland Ice Mapping Project (GIMP) land classification and surface elevation data sets, *Cryosph.*, *8*(4), 1509–1518, doi:10.5194/tc-8-1509-2014.

IBCAO (2011), The IBCAO Compilation Team Introduces the Upcoming Version 3.0, *AGU Fall Meeting Posters*.

Inc., G. (2017), Geosoft oasis montaj, `http://www.geosoft.com/products/oasis-montaj`.

Institution, W. H. O. (2006), Polardiscovery, `http://polardiscovery.whoi.edu/index.html`.

Jakobsson, M., R. Macnab, L. Mayer, R. Anderson, M. Edwards, J. Hatzky, H. W. Schenke, and P. Johnson (2008), An improved bathymetric portrayal of the Arctic Ocean: Implications for ocean modeling and geological, geophysical and oceanographic analyses, *Geophys. Res. Lett.*, *35*(7), n/a–n/a, doi:10.1029/2008GL033520.

Jakobsson, M., L. Mayer, B. Coakley, J. A. Dowdeswell, S. Forbes, B. Fridman, H. Hodnesdal, R. Noormets, R. Pedersen, M. Rebesco, H. W. Schenke, Y. Zarayskaya, D. Accettella, A. Armstrong, R. M. Anderson, P. Bienhoff, A. Camerlenghi, I. Church, M. Edwards, J. V. Gardner, J. K. Hall, B. Hell, O. Hestvik, Y. Kristoffersen, C. Marcussen, R. Mohammad, D. Mosher, S. V. Nghiem, M. T. Pedrosa, P. G. Travaglini, and P. Weatherall (2012), The International Bathymetric Chart of the Arctic Ocean (IBCAO) Version 3.0, *Geophys. Res. Lett.*, *39*(12), 1–6, doi:10.1029/2012GL052219.

Johnson, H. L., A. Münchow, K. K. Falkner, and H. Melling (2011), Ocean circulation and properties in Petermann Fjord, Greenland, *J. Geophys. Res. Ocean.*, *116*(1), 1–18, doi:10.1029/2010JC006519.

Joughin, I., W. Abdalati, and M. Fahnestock (2004), Large fluctuations in speed on Greenland's Jakobshavn Isbræ glacier, *Nature*, *432*(7017), 608–610, doi:10.1038/nature03130.

Joughin, I., I. M. Howat, M. Fahnestock, B. Smith, W. Krabill, R. B. Alley, H. Stern, and M. Truffer (2008), Continued evolution of Jakobshavn Isbrae following its rapid speedup, *J. Geophys. Res. Earth Surf.*, *113*(4), 1–14, doi:10.1029/2008JF001023.

Joughin, I., B. E. Smith, I. M. Howat, D. Floricioiu, R. B. Alley, M. Truffer, and M. Fahnestock (2012), Seasonal to decadal scale variations in the surface velocity of Jakobshavn Isbrae, Greenland: Observation and model-based analysis, *J. Geophys. Res. Earth Surf.*, *117*(2), 1–20, doi:10.1029/2011JF002110.

Joughin, I., B. E. Smith, D. E. Shean, and D. Floricioiu (2014), Brief communication: Further summer speedup of jakobshavn isbræ, *Cryosphere*, *8*(1), 209–214, doi:10.5194/tc-8-209-2014.

Khan, S. A., J. Wahr, M. Bevis, I. Velicogna, and E. Kendrick (2010), Spread of ice mass loss into northwest Greenland observed by GRACE and GPS, *Geophys. Res. Lett.*, *37*(6), 1–5, doi:10.1029/2010GL042460.

Koppes, M., B. Hallet, E. Rignot, J. Mouginot, J. S. Wellner, and K. Boldt (2015), Observed latitudinal variations in erosion as a function of glacier dynamics, *Nature*, *526*(7571), 100–103, doi:10.1038/nature15385.

Leuschen, C., P. Gogineni, F. Rodriguez-Morales, J. Paden, and C. Allen. (2010, updated 2017), IceBridge MCoRDS L2 Ice Thickness, Version 1, *NASA National Snow and Ice Data Center*, doi:http://dx.doi.org/10.5067/GDQ0CUCVTE2Q.

Lowrie, W. (1997), *Fundamentals of Geophysics*, 89,10 pp., Cambridge University Press, Cambridge.

Luckman, A., and T. Murray (2005), Seasonal variation in velocity before retreat of Jakobshavn Isbræ, Greenland, *Geophys. Res. Lett.*, *32*(8), 1–4, doi:10.1029/2005GL022519.

MacAyeal, D. R., J. Freed-Brown, W. W. Zhang, and J. M. Amundson (2012), The influence of ice melange on fjord seiches, *Ann. Glaciol.*, *53*(60), 45–49, doi:10.3189/2012/AoG60A027.

Millan, R., E. Rignot, V. Bernier, M. Morlighem, and P. Dutrieux (2017), Bathymetry of the Amundsen Sea Embayment sector of West Antarctica from Operation IceBridge gravity and other data, *Geophys. Res. Lett.*, *44*(3), 1360–1368, doi:10.1002/2016GL072071.

Morlighem, M., E. Rignot, J. Mouginot, X. Wu, H. Seroussi, E. Larour, and J. Paden (2013), High-resolution bed topography mapping of Russell Glacier, Greenland, inferred from Operation IceBridge data, *J. Glaciol.*, *59*(218), 1015–1023, doi:10.3189/2013JoG12J235.

Morlighem, M., E. Rignot, J. Mouginot, H. Seroussi, and E. Larour (2014), Deeply incised submarine glacial valleys beneath the Greenland ice sheet, *Nat. Geosci.*, *7*(6), 18–22, doi:10.1038/ngeo2167.

Morlighem, M., E. Rignot, and J. Willis (2016), Improving Bed Topography Mapping of Greenland Glaciers Using NASA's Oceans Melting Greenland (OMG) Data, *Oceanography*, *29*(4), 62–71, doi:10.5670/oceanog.2016.99.

Motyka, R. J., M. Truffer, M. Fahnestock, J. Mortensen, S. Rysgaard, and I. Howat (2011), Submarine melting of the 1985 Jakobshavn Isbræ floating tongue and the triggering of the current retreat, *J. Geophys. Res. Earth Surf.*, *116*(1), 1–17, doi:10.1029/2009JF001632.

Mouginot, J., E. Rignot, B. Scheuchl, I. Fenty, A. Khazendar, M. Morlighem, A. Buzzi, and J. Paden (2015), Fast retreat of Zachariæ Isstrøm, northeast Greenland, *Science (80-.).*, *350*(November), 1357–1361, doi:10.1126/science.aac7111.

Murray, T., K. Scharrer, T. D. James, S. R. Dye, E. Hanna, A. D. Booth, N. Selmes, A. Luckman, A. L. C. Hughes, S. Cook, and P. Huybrechts (2010), Ocean regulation hypothesis for glacier dynamics in southeast Greenland and implications for ice sheet mass changes, *J. Geophys. Res. Earth Surf.*, *115*(3), 1–15, doi:10.1029/2009JF001522.

Muto, A., S. Anandakrishnan, and R. B. Alley (2013), Subglacial bathymetry and sediment layer distribution beneath the Pine Island Glacier ice shelf, West Antarctica, modeled using aerogravity and autonomous underwater vehicle data, *Ann. Glaciol.*, *54*(64), 27–32, doi:10.3189/2013AoG64A110.

Muto, A., L. E. Peters, K. Gohl, I. Sasgen, R. B. Alley, S. Anandakrishnan, and K. L. Riverman (2016), Subglacial bathymetry and sediment distribution beneath Pine Island Glacier ice shelf modeled using aerogravity and in situ geophysical data: New results, *Earth Planet. Sci. Lett.*, *433*, 63–75, doi:10.1016/j.epsl.2015.10.037.

Myers, P. G., N. Kulan, and M. H. Ribergaard (2007), Irminger water variability in the West Greenland Current, *Geophys. Res. Lett.*, *34*(17), 2–7, doi:10.1029/2007GL030419.

Oldenburg, W. D. (1974), The inversion and interpretation of gravity anomalies, *Geophysics*, *39*(4), 526–536.

Parker, R. (1973), The rapid calcuation of potential anomalies, *Geophys. J.*, *31*(4), 447–455.

Pedersen, M., W. L. Weng, N. Keulen, and T. F. Kokfelt (2013), A new seamless digital 1:500 000 scale geological map of Greenland, *Geol. Surv. Denmark Greenl. Bull.*, pp. 65–68.

Plouff, D. (1976), Gravity and Magnetic Fields of Polygonal Prisms and Application to Magnetic Terrain Corrections, *Geophysics*, *41*(4), 727–741, doi:10.1190/1.1440645.

Plummer, J., S. Gogineni, C. van der Veen, C. Leuschen, and J. Li (2008), Ice thickness and bed map for Jakobshavn Isbræ, *CReSIS Tech. Rep., Univ. of Kansas, Lawrence, Kans.*

Post, A., S. O'Neel, R. J. Motyka, and G. Streveler (2011), A complex relationship between calving glaciers and climate, *Eos (Washington. DC).*, *92*(37), 305–307, doi:10.1029/2011EO370001.

Pritchard, H. D., R. J. Arthern, D. G. Vaughan, and L. A. Edwards (2009), Extensive dynamic thinning on the margins of the Greenland and Antarctic ice sheets: Supplemental, *Nature*, *461*(7266), 971–975, doi:10.1038/nature08471.

Ribergaard, M. H. (2013), Introduction to the west Greenland oceanography.

Rignot, E., and P. Kanagaratnam (2006), Changes in the Velocity Structure of the Greenland Ice Sheet, *ScienceScience*, pp. 986–990, doi:10.1126/science.1121381.

Rignot, E., and J. Mouginot (2012), Ice flow in Greenland for the International Polar Year 2008-2009, *Geophys. Res. Lett.*, *39*(11), 1–7, doi:10.1029/2012GL051634.

Rignot, E., and K. Steffen (2008), Channelized bottom melting and stability of floating ice shelves, *Geophys. Res. Lett.*, *35*(2), 2–6, doi:10.1029/2007GL031765.

Rignot, E., and R. R. H. Thomas (2002), Mass Balance of Polar Ice Sheets, *Science (80-.).*, *297*(5586), 1502–1506, doi:10.1126/science.1073888.

Rignot, E., A. Rivera, and G. Casassa (2003), Contribution of the Patagonia Icefields of South America to sea level rise., *Science*, *302*(5644), 434–7, doi:10.1126/science.1087393.

Rignot, E., J. E. Box, E. Burgess, and E. Hanna (2008), Mass balance of the Greenland ice sheet from 1958 to 2007, *Geophys. Res. Lett.*, *35*(20), 1–5, doi:10.1029/2008GL035417.

Rignot, E., M. Koppes, and I. Velicogna (2010), Rapid submarine melting of the calving faces of West Greenland glaciers, *Nat. Geosci.*, *3*(3), 187–191, doi:10.1038/ngeo765.

Rignot, E., I. Velicogna, M. R. Van Den Broeke, A. Monaghan, and J. Lenaerts (2011a), Acceleration of the contribution of the Greenland and Antarctic ice sheets to sea level rise, *Geophys. Res. Lett.*, *38*(5), 1–5, doi:10.1029/2011GL046583.

Rignot, E., J. Mouginot, and B. Scheuchl (2011b), Antarctic grounding line mapping from differential satellite radar interferometry, *Geophys. Res. Lett.*, *38*(10), 1–6, doi:10.1029/2011GL047109.

Rignot, E., I. Fenty, D. Menemenlis, and Y. Xu (2012), Spreading of warm ocean waters around Greenland as a possible cause for glacier acceleration, *Ann. Glaciol.*, *53*(60), 257–266, doi:10.3189/2012AoG60A136.

Rignot, E., J. Mouginot, M. Morlighem, H. Seroussi, and B. Scheuchl (2014), Widespread, rapid grounding line retreat of Pine Island, Thwaites, Smith, and Kohler glaciers, West Antarctica, from 1992 to 2011, *Geophys. Res. Lett.*, *41*(10), 3502–3509, doi:10.1002/2014GL060140.

Rignot, E., I. Fenty, Y. Xu, C. Cai, and C. Kemp (2015), Undercutting of marine-terminating glaciers in West Greenland, *Geophys. Res. Lett.*, *42*(14), 5909–5917, doi:10.1002/2015GL064236.

Rignot, E., I. Fenty, Y. Xu, C. Cai, I. Velicogna, C. Cofaigh, J. A. Dowdeswell, W. Weinrebe, G. Catania, and D. Duncan (2016), Bathymetry data reveal glaciers vulnerable to ice-ocean interaction in Uummannaq and Vaigat glacial fjords, west Greenland, *Geophys. Res. Lett.*, *43*(6), 2667–2674, doi:10.1002/2016GL067832.

Rosenau, R., E. Schwalbe, H. G. Maas, M. Baessler, and R. Dietrich (2013), Grounding line migration and high-resolution calving dynamics of Jakobshavn Isbræ, West Greenland, *J. Geophys. Res. Earth Surf.*, *118*(2), 382–395, doi:10.1029/2012JF002515.

Roy, L., M. K. Sen, D. D. Blankenship, P. L. Stoffa, and T. G. Richter (2005), Inversion and uncertainty estimation of gravity data using simulated annealing : An application over Lake Vostok , East Antarctica, *Geophysics*, *70*(1), J1–J12, doi:10.1190/1.1852777.

Schoof, C. (2007), Ice sheet grounding line dynamics: Steady states, stability, and hysteresis, *J. Geophys. Res. Earth Surf.*, *112*(3), 1–19, doi:10.1029/2006JF000664.

Seber, D., E. Sandvol, C. Sandvol, C. Brindisi, and M. Barazangi (2001), Crustal model for the Middle East and North Africa region: Implications for the isostatic compensation mechanism, *Geophys. J. Int.*, *147*(3), 630–638, doi:10.1046/j.0956-540x.2001.01572.x.

Sergienko, O. V., T. T. Creyts, and R. C. A. Hindmarsh (2014), Similarity of organized patterns in driving and basal stresses of Antarctic and Greenland ice sheets beneath extensive areas of basal sliding, *Geophys. Res. Lett.*, *41*(11), 3925–3932, doi:10.1002/2014GL059976.

Shapero, D. R., I. R. Joughin, K. Poinar, M. Morlighem, and F. Gillet-Chaulet (2016), Basal resistance for three of the largest Greenland outlet glaciers, *J. Geophys. Res. F Earth Surf.*, *121*(1), 168–180, doi:10.1002/2015JF003643.

Smith, W., and D. Sandwell (2004), Conventional Bathymetry, Bathymetry from Space, and Geodetic Altimetry, *Oceanography*, *17*(1), 8–23, doi:10.5670/oceanog.2004.63.

Stearns, L. A., and G. S. Hamilton (2007), Rapid volume loss from two East Greenland outlet glaciers quantified using repeat stereo satellite imagery, *Geophys. Res. Lett.*, *34*(5), 1–5, doi:10.1029/2006GL028982.

Straneo, F., and P. Heimbach (2013), North Atlantic warming and the retreat of Greenland's outlet glaciers., *Nature*, *504*(7478), 36–43, doi:10.1038/nature12854.

Straneo, F., D. Sutherland, D. Holland, C. Gladish, G. Hamilton, H. Johnson, E. Rignot, Y. Xu, and M. Koppes (2012), Characteristics of ocean waters reaching greenland's glaciers, *Annals of Glaciology*, *53*(60), 202–210, doi:10.3189/2012AoG60A059.

Straneo, F., P. Heimbach, O. Sergienko, G. Hamilton, G. Catania, S. Griffies, R. Hallberg, A. Jenkins, I. Joughin, R. Motyka, W. T. Pfeffer, S. F. Price, E. Rignot, T. Scambos, M. Truffer, and A. Vieli (2013), Challenges to understanding the dynamic response of Greenland's marine terminating glaciers to oc eanic and atmospheric forcing, *Bull. Am. Meteorol. Soc.*, *94*(8), 1131–1144, doi:10.1175/BAMS-D-12-00100.1.

Studinger, M., R. E. Bell, and A. A. Tikku (2004), Estimating the depth and shape of subglacial Lake Vostok's water cavity from aerogravity data, *Geophys. Res. Lett.*, *31*(12), 2–5, doi:10.1029/2004GL019801.

Studinger, M., R. Bell, and N. Frearson (2008), Comparison of AIRGrav and GT-1A airborne gravimeters for research applications, *Geophysics*, *73*(6), I51–I61, doi:10.1190/1.2969664.

Talwani, M., J. L. Worzel, and M. Landisman (1959), Rapid gravity computations for two-dimensional bodies with application to the Mendocino submarine fracture zone, *J. Geophys. Res.*, *64*(1), 49, doi:10.1029/JZ064i001p00049.

Thomas, R. (2004), Force perturbation analysis of recent thinning and acceleration of Jakobshavn Isbrae, Greenland., *J. Glaciol.*, *50*(168), 57–66, doi:10.3189/172756504781830321.

Thomas, R., W. Krabill, E. Frederick, and K. Jezek (1995), Thickening of Jakobshavns Isbr*ae*, West Greenland, measured by airborne laser altimetry, *Ann. Glaciol.*, *21*, 259–262, doi:https://doi.org/10.1017/S0260305500015913.

Thomas, R., E. Frederick, W. Krabill, S. Manizade, and C. Martin (2009), Recent changes on greenland outlet glaciers, *J. Glaciol.*, *55*(189), 147–162, doi:10.3189/002214309788608958.

Thomas, R. H., B. M. Csathó, S. Gogineni, K. G. Jezek, and K. Kuivinen (1998), Thickening of the western part of the Greenland ice sheet, *J. Glaciol.*, *44*(148), 653–658.

Thomas, R. H., W. Abdalati, E. Frederick, W. B. Krabill, S. Manizade, and K. Steffen (2003), Investigation of surface melting and dynamic thinning on Jakobshavn Isbrae, Greenland, *J. Glaciol.*, *49*, 231–239, doi:10.3189/172756503781830764.

Tinto, K. J., and R. E. Bell (2011), Progressive unpinning of Thwaites Glacier from newly identified offshore ridge: Constraints from aerogravity, *Geophys. Res. Lett.*, *38*(20), 1–6, doi:10.1029/2011GL049026.

Tinto, K. J., R. E. Bell, J. R. Cochran, and A. Münchow (2015), Bathymetry in Petermann fjord from Operation IceBridge aerogravity, *Earth Planet. Sci. Lett.*, *422*, 58–66, doi:10.1016/j.epsl.2015.04.009.

van den Broeke, M., J. Bamber, J. Ettema, E. Rignot, E. Schrama, W. J. van de Berg, E. van Meijgaard, I. Velicogna, and B. Wouters (2009), Partitioning Recent Greenland Mass Loss, *Science (80-.).*, *326*(5955), 984–986, doi:10.1126/science.1178176.

Velicogna, I. (2009), Increasing rates of ice mass loss from the Greenland and Antarctic ice sheets revealed by GRACE, *Geophys. Res. Lett.*, *36*(19), 2–5, doi:10.1029/2009GL040222.

Velicogna, I., and J. Wahr (2013), Time-variable gravity observations of ice sheet mass balance: Precision and limitations of the GRACE satellite data, *Geophys. Res. Lett.*, *40*(12), 3055–3063, doi:10.1002/grl.50527.

Weidick, A., and O. Bennike (2007), *Quaternary glaciation history and glaciology of Jakobshavn Isbrae and the Disko Bugt region, West Greenland: A review.*, 14, 7–+ pp., Geological Survey of Denmark and Greenland (GEUS).

Weidick, A., N. Mikkelsen, C. Mayer, and S. Podlech (2004), Jakobshavn Isbrae, West Greenland: The 20022003 collapse and nomination for the UNESCO World Heritage List, *Geol. Surv. Denmark Greenl. Bull.*, *4*(August 2017), 85–88.

Weinrebe, W., A. Kuijpers, I. Klaucke, and M. Fink (2009), Multibeam Bathymetry Surveys in Fjords and Coastal Areas of West-Greenland, *AGU Fall Meeting Abstracts*.

Williams, C. N., S. L. Cornford, T. M. Jordan, J. A. Dowdeswell, M. J. Siegert, C. D. Clark, D. A. Swift, A. Sole, I. Fenty, and J. L. Bamber (2017), Generating synthetic fjord bathymetry for coastal Greenland, *Cryosphere*, *11*(1), 363–380, doi:10.5194/tc-11-363-2017.

Wu, X. (2014), IceBridge Radar L3 Tomographic Ice Thickness, *NASA National Snow and Ice Data Center*, doi:http://dx.doi.org/10.5067/92SUAOLU6AP1.

Xu, Y., E. Rignot, I. Fenty, D. Menemenlis, and M. M. Flexas (2013), Subaqueous melting of Store Glacier, west Greenland from three-dimensional, high-resolution numerical modeling and ocean observations, *Geophys. Res. Lett.*, *40*(17), 4648–4653, doi:10.1002/grl.50825.

Yin, J., J. T. Overpeck, S. M. Griffies, A. Hu, J. L. Russell, and R. J. Stouffer (2011), Different magnitudes of projected subsurface ocean warming around Greenland and Antarctica, *Nat. Geosci.*, *4*(8), 524–528, doi:10.1038/ngeo1189.